Search for the electric dipole moment of the muon at the Fermilab Muon g-2 experiment

LUCY BAILEY

University College London

Department of Physics and Astronomy

Submitted in partial fulfilment of the requirements for the degree of Doctor of Philosophy.

Declaration

I, Lucy Bailey, confirm that the work presented in this thesis is my own. Where information has been derived from other sources, I confirm that this has been indicated in the thesis.



Lucy Bailey London, United Kingdom March 2025

The author acknowledges that the Muon g-2 experiment at Fermilab was designed, commissioned, and run by a full collaboration of over to 200 people at any given time. Derivation of the sensitivity to an EDM in Section 2.2.4 is based on principles developed for Muon g-2 analysis and was developed by P. Debevec and J. Price.

Work to improve the tracking efficiency, as detailed in Section 2.3.3, was led by G. Hesketh, with tests, and implementation completed by the author. A mechanism for producing a false in-phase oscillation as mentioned in Section 3.1.6 was investigated by J. Price.

The cross-checks at different frequencies described in Section 3.3.3 were completed by M. Sakurai, who also determined the CBO frequency used in the EDM fits. D. Vasilkova was responsible for the MC production, characterisation of the tracker acceptance, and determining the associated uncertainties as described in Section 3.2.7. The final combination and limit setting was completed by G. Hesketh.

Acknowledgements

Naturally, the work in this thesis could have not been completed without the consistent support of mentors, colleagues, and friends. I would like to thank my supervisor, Gavin Hesketh, who continually advocated for me and my work, encouraged me to tackle challenges head on, and was a pleasure to work with - thank you.

I'd like to thank the whole Muon g-2 collaboration, who were always welcoming and whose knowledge of the experiment was invaluable. I also thank the review committee for volunteering their time to scrutinise the analysis of the muon electric dipole moment (EDM). Special thanks to James Mott for his comprehensive expertise and willingness to help. For excellent company while at Fermilab and their work on the radial field measurements, I especially thank Brendan Kiburg, Simon Corrodi and Fatima Rodriguez.

The EDM team is small but tireless and I thank all of them for their expertise and hard work. In particular, I thank Joe Price for his dedication to the analysis, fruitful conversations, and practical advice. I would also like to thank the PhDs that paved the way for the analysis: Dominika Vasilkova for their guidance, advice and, when needed, mutual despair; and Sam Grant, who was always prepared to give his time and attention to my questions.

I thank my colleagues, friends, and former housemates - Margot MacMahon and Marcin Jastrzebski - for the moral support, flat dinners, and laughs. I am incredibly grateful to Daniel MacLean for his patience, encouragement, and proof-reading services. Lastly, I thank my parents for their steadfast support and greatly appreciate their efforts to not only understand what I do, but also attempt to explain it to others.

Abstract

Due to the experimental setup at the Fermilab Muon g-2 experiment, a measurement of the electric dipole moment (EDM) is facilitated alongside the main measurement of the anomalous magnetic moment. The search for the muon EDM, which uses the straw tracking detector, is presented here. EDMs are vanishingly small in the Standard Model and the detection of any significant EDM would be new physics outright and provide a source of CP-violation.

Firstly, the Standard Model picture of magnetic moments and EDMs are explained to motivate the experiment and EDM measurement. Experimental methods, setup and recent improvements are then set out, followed by the EDM analysis of the Run-2/3 dataset. Sources of systematic uncertainty are described and characterised and several cross-checks are performed. The data is currently blinded but, given a final measurement of exactly zero muon EDM, $d_{\mu}=0$, the best-case limit would then be $|d_{\mu}|<0.33\times10^{-19}~e\cdot{\rm cm}$ at 95% confidence level.

Impact Statement

The Muon g-2 experiment will measure the anomalous magnetic moment of the muon to 140 ppb and provide one of the most stringent tests of the Standard Model. A measurement of the muon electric dipole moment (EDM) is also facilitated and will help to probe theories beyond the Standard Model (BSM).

Improvements to the tracking algorithms to maximise statistics are necessary for the EDM analysis to reach its sensitivity goals. In total the number of tracks available for analysis for the Run-2/3 dataset was increased by 2.7 times. Some of these updates are also used in tracking for the g-2 analysis to determine systematics and corrections in Run-4/5/6. Further, the measurement of the radial field is necessary to account for the EDM-like signal it produces. The correction to the measured EDM is needed for the Run-2/3 dataset but will also be required for analysis of the full dataset in the future.

Analysis of the Run-2/3 dataset presented here will be the best direct limit on the muon electric dipole moment when unblinded and improve on the previous limit by up to 5.5 times. Precision measurements provide tests of the SM and help to constrain BSM physics.

Contents

Ab	brev	viations	s	8
Lis	st of	Figure	es	9
Lis	st of	Tables	;	16
1	The	\mathbf{ory}		18
	1.1	The St	candard Model of particle physics	18
	1.2	Charge	e-parity violation in the Standard Model	19
	1.3	Muons		21
	1.4	Magne	tic dipole moments	21
	1.5	Electri	c dipole moments	23
	1.6	Summa	ary	26
2	Exp	erimer	ntal Methods	27
	2.1	Spin p	recession	28
	2.2	Measu	rement principles	29
		2.2.1	a_{μ} measurement principle	29
		2.2.2	EDM measurement principle	31
		2.2.3	EDM measurement in the lab frame	32
		2.2.4	Sensitivity to an EDM	33
	2.3	Experi	mental setup	36
		2.3.1	Beam dynamics effects	39
		2.3.2	Straw trackers	40
		2.3.3	Improving the tracking efficiency	42
		2.3.4	Quality cut adjustment	46
	2.4	Simula	tion	47
		2.4.1	EDM in simulation	47
		2.4.2	Tracker acceptance	48
		2.4.3	Updates to simulation	51
	2.5	Radial	magnetic field	52
		2.5.1	Tilt in the spin precession plane	52
		2.5.2	Direct measurement	53
		2.5.3	Measurement using the ESQs	54
		2.5.4	Extrapolating the radial field	55
		2.5.5	Run-6 measurement and extrapolation	55
3	Ana	lysis		59
	3.1	EDM a	analysis	59
		3.1.1	Data analysed	59
		3.1.2	Momentum binning	60

		3.1.3	Handling of data prior to fitting	60
		3.1.4	Fitting	63
		3.1.5	Blinding	76
		3.1.6	EDM fit results	77
	3.2	System	natic uncertainties	87
		3.2.1	Randomisation of VB oscillations	87
		3.2.2	Beam scraping correction	87
		3.2.3	g-2 phase	88
		3.2.4	g-2 momentum dependent phase	91
		3.2.5	g-2 amplitude	91
		3.2.6	CBO fit parameters	91
		3.2.7	$R_{\rm acc}(\lambda)$ uncertainties	91
		3.2.8	$R_{e^+}(\lambda)$ uncertainty	95
		3.2.9	Polarisation	95
		3.2.10	Muon momentum spread	96
		3.2.11	Radial field	96
		3.2.12	Systematic uncertainty summary	97
	3.3	Cross-	checks	101
		3.3.1	Analysis without momentum binning	101
		3.3.2	Fit start-time scans	104
		3.3.3	Check for oscillation at the CBO frequency	105
	3.4	Combi	ning results	106
	3.5	Limit	setting	111
	3.6	Estima	ate of best sensitivity	112
	3.7	Discus	sion	112
Aı	ppen	dices		120
\mathbf{A}	Exa	mple r	esults from beam scraping fit and correction	121
В	All	fit star	et-time scan plots	123
\mathbf{C}	Uno	ertaint	ties on the R-factors	142

Abbreviations

Notation	Description
BMT	Bargmann-Michel-Telegdi.
BNL	Brookhaven National Laboratory.
CL	Confidence level.
CBO	Coherent betatron oscillation.
CP	Charge conjugation and parity operation.
DCA	Distance of closest approach.
EDM	Electric dipole moment.
EM	Electromagnetic.
ESQ	Electrostatic quadrupole.
FFT	Fast Fourier transform.
FNAL	Fermilab National Accelerator Laboratory.
FOM	Figure of merit.
FR	Fast rotation.
HLbL	Hadronic Light-by-Light.
HVP	Hadronic vacuum polarisation.
MC	Monte Carlo.
MDM	Magnetic dipole moment.
MRF	Muon rest frame.
NDF	Number of degrees of freedom.
NMR	Nuclear magnetic resonance.
QED	Quantum electrodynamics.
QC	Quality cut.
QV	Quality vertex.
QCD	Quantum chromodynamics.
RMS	Root mean square.
VB	Vertical betatron.

List of Figures

1.1	and two neutrinos	21
1.2	Five Feynman diagrams showing: the Dirac equation interaction giving $g=2$; and loop diagrams from QED, Electroweak and Hadronic interactions that contribute to a_{μ}	22
1.3	Illustration of (a) a dipole under (b) parity (P) and (c) time-reversal (T) transformations showing that an EDM d violates both P and T symmetries	25
1.4	Summary of current best EDM limits for the electron, muon, neutron, and proton. SM predictions are included and a summary of various BSM theory predictions in yellow. The dashed lined represent expected limits from future experiments and the muon limit based on mass scaling using the electron EDM limit	25
2.1	Picture of the storage ring in the experiment hall at FNAL. The white covering is insulation to minimise temperature fluctuations in order to keep the magnetic field more stable.	27
2.2	Illustration of a muon in storage ring, undergoing circular motion with spin precessing in \hat{x} - \hat{z} plane. Courtesy of P. Debevec	30
2.3	Illustration of the spin precession plane for an antimuon when (a) there is no EDM and the spin precesses in the \hat{x} - \hat{z} plane, and (b) when there is a non-zero EDM and the precession plan is the tilted. Courtesy of P. Debevec	32
2.4	The number function $N(\lambda)$, EDM asymmetry function $A_{\pm}(\lambda)$ and statistical Figure-of-Merit $NA^{2}(\lambda)$ in the lab frame	35
2.5	Reduction in the average vertical angle in the lab frame at point of maximum tilt in the MRF $R_{e^+}(\lambda)$	35
2.6	A cross section of the storage ring dipole showing the storage region and the various tools for making minor adjustments to improve the magnetic field uniformity	37
2.7	A schematic drawing of the storage ring including the systems for muon injection and focussing, as well as the detectors	37

2.8	Fourier transform of the residuals from a fit following Equa-	
	tion 2.2.6 (red dashed line) and from the full fit (black	
	line). The peaks correspond to the missing betatron fre-	
	quencies and muon losses. Data are from the Run-3a data	
	set. Inset: corresponding asymmetry-weighted e^+ time	
	spectrum (black line) with the full fit function (red line)	
	overlaid. Caption adapted and figure taken from [33]	40
2.9	A top down view of a tracker station in the storage ring.	
	The decay positron travels inwards towards a calorimeter,	
	passing through the straw tracker modules	41
2.10	One tracker module containing 4 layers of 32 straws. A	4.4
0.11	tracker station is made up of 8 of these modules	41
2.11	A cross-section of a straw indicating the distance of closest	40
0.10	approach (DCA) of the positron.	42
2.12	Example of a 2D histogram of drift time and DCA for	
	layer 49 in run 15921. The colour axis shows the number of entries.	43
າ 19		40
2.13	Example of the Gaussian fit to the projection of DCA for a slice in drift time around 40 ns for layer 49 in run 15921.	
	The histogram statistics are shown above the fit results.	43
2 14	Example of the fifth order polynomial fit to the DCA cal-	10
2.11	ibration in for layer 49 in run 15921. The $\chi^2/\text{NDF} = 4.8$,	
	which is larger than the ideal 1 and is probably caused by	
	the difficulty in fitting drift times for positrons that pass	
	very near the edge of the straw or near the central wire	44
2.15	The hit width distributions for each station with $0 < t <$	
	300 µs from a subset of data in Run-3. The impact of	
	cross-talk can be seen in the peak at at low hit width,	
	with good hits peaking around 30 ns width	44
2.16	The scaling applied the the uncertainty on the DCA for	
	stations 12 and 18	45
2.17	A comparison of the quality vertex tracking efficiency in	
	station 12 with a hit width cut versus with both a hit	
	width cut and the fill-time dependent uncertainty on the	4 -
0.10	DCA. The results are alike in station 18	45
2.18	Comparison of momentum distributions in data for tracks	
	that hit no volumes and tracks hitting the four most commonly hit volumes	46
2 10	The distributions and residuals for true tracks and reco	40
2.19	tracks that hit the carbon fibre post and pass all other	
	QV cuts for (a) momentum and (b) vertical decay angle.	47
2.20	Azimuthal decay positions for reco track vertices in MC	Δ,
	showing an acceptance of $\sim 25^{\circ}$ in azimuth	48
2.21	Fitted EDM amplitude for each momentum bin for all	
	decays, reco track vertices and true track vertices. Due	
	to acceptance effects, the measured amplitude from track	
	vertices is reduced compared to the <i>all decays</i> amplitude.	49
2.22	Acceptance of vertical angles in momentum from MC with	
	injected EDM of $5.4 \times 10^{-18}~e \cdot \text{cm}$. The z axis is normalised	
	so that the peak is at 1.	49

2.23	The vertical angle θ_y and vertical decay position y in the momentum range 500 - 3000 MeV for the (a) all decays sample and (b) true track vertices, demonstrating the effects of tracker acceptance	49
2.24	The vertical beam distributions from MC track vertices using the default gas gun settings (red) and the flattened distribution used for the EDM analysis (blue)	51
2.25	The DCA to drift time relation for producing hits in MC showing the updated conversion using a fit to data for layer 47 (blue) compared to the previous linear relationship used for all layers (red)	52
2.26	Illustration of the tilt in the spin precession plane due to a radial magnetic field	53
2.27	The expected radial field from the SCC settings compared to the radial field as measured by the Hall probe. These are both relative to the nominal Run-5 SCC setting. A straight line fit is shown	54
2.28	The data used to fit the reference vertical position around the time of the ESQ-based radial field measurement in Run-6. The hashed box indicates when the radial field measurement was made	56
2.29	The results from the linear fit to the vertical position and applied field for four ESQ voltages	57
2.30	The linear fit to the gradients from Figure 2.29 against the inverse of the ESQ voltages	57
2.31	The extrapolated average radial field in Run-6 using the Run-6 ESQ-based radial field measurement, showing the statistical and systematic uncertainties determined for each dataset	57
3.1	Run-2/3 combined positron momentum distribution for analysis vertices with the 8 momentum bins used in the EDM analysis shown by red dashed lines	60
3.2	FFT of the EDM fit residuals from 3N, stations combined, $750 MeV with (a) before VB randomisation and (b) after VB randomisation is applied$	61
3.3	Fits to the drift in vertical angle due to beam scraping for dataset 3N and shown for each momentum bin and both	
3.4	The result of applying the beam scraping correction to dataset 3N for both stations and all momentum bins	62 62
3.5	The phase from EDM fits to MC decays, where the phase, ϕ_a , is allowed to float in the numerator of Equation 3.1.3.	64
3.6	Fit to the anomalous precession frequency for quality track vertices with $p > 1.7$ GeV for station 12	65
3.7	Fit to the anomalous precession frequency for quality track vertices with $p > 1.7$ GeV for station 18	65
3.8	Fit to the anomalous precession frequency in momentum bins for Run-2 station 12.	67

3.9	Fit to the anomalous precession frequency in momentum	
	bins for Run-2 station 18	68
3.10	Fit to the anomalous precession frequency in momentum	
	bins for Run-3a station 12	69
3.11	Fit to the anomalous precession frequency in momentum	
	bins for Run-3a station 18	70
3.12	Fit to the anomalous precession frequency in momentum	
	bins for Run-3b station 12	71
3.13	Fit to the anomalous precession frequency in momentum	
	bins for Run-3b station 18	72
3.14	Summary of the amplitude from the anomalous precession	
	frequency fits in each momentum bin for all datasets and	
	both stations. The uncertainties on all point have been	
	multiplied by 10 to improve readability	73
3.15	Summary of the phase from the anomalous precession fre-	
	quency fits in each momentum bin for all datasets and	
	both stations. The uncertainties on all point have been	
	multiplied by 10 to improve readability	73
3.16	Summary of the CBO amplitude from the anomalous pre-	
	cession frequency fits in each momentum bin for all datasets	
	and both stations	74
3.17	Summary of the CBO phase from the anomalous preces-	
	sion frequency fits in each momentum bin for all datasets	
	and both stations	74
3.18	Summary of the reduced χ^2 from the anomalous precession	
	frequency fits in each momentum bin for all datasets and	
0.40	both stations.	75
3.19	The distribution of blinding multipliers from 100,000 unique	70
0.00	blinding strings. Adapted from [63]	76
3.20	Fit to the average vertical angle in momentum bins for	70
2 01	Run-2 station 12.	78
3.21	Fit to the average vertical angle in momentum bins for Run-2 station 18	70
2 99		79
3.22	Fit to the average vertical angle in momentum bins for Run-3a station 12	80
3 93	Fit to the average vertical angle in momentum bins for	80
0.20	Run-3a station 18	81
3 24	Fit to the average vertical angle in momentum bins for	01
0.24	Run-3b station 12	82
3 25	Fit to the average vertical angle in momentum bins for	02
0.20	Run-3b station 18	83
3 26	Summary of the χ^2/NDF for the average vertical angle fits	
0.20	in each momentum bin for all datasets and both stations.	84
3 27	Summary of the p values for the average vertical angle fits	01
0.21	in each momentum bin for all datasets and both stations.	84
3.28	Summary of A_{EDM} from the average vertical angle fits be-	J 1
3.20	fore any corrections in each momentum bin for all datasets	
	and both stations	85
3.29	Summary of A_{g-2} from the average vertical angle fits in	
-	each momentum bin for all datasets and both stations.	85

3.30	The fitted A_{g-2} from a toy MC study before and after	
	applying an acceptance function with a bias of $+1$ mrad. The acceptance introduces a false amplitude in the fit in	
	phase with $g-2$	86
3.31	Summary of offset C from the average vertical angle fits in each momentum bin for all datasets and both stations.	86
	The fitted phase from the anomalous precession frequency after varying the lower cut on positron momentum ± 100 MeV from the nominal value of 1700 MeV for dataset 3N (a) S12 and (b) S18	V 89
3.33	The functional form of $R_{e^+}(\lambda)$ at the Born-level (red) compared to the extraction from MC including higher order radiative correction (green)	95
3.34	Fit to the anomalous precession frequency for track vertices $750 \le p < 2750$ MeV from S12 for all datasets	102
3.35	Fit to the anomalous precession frequency for track vertices $750 \le p < 2750$ MeV from S18 for all datasets	102
3.36	Fit to the average vertical angle for track vertices 750 \leq $p < 2750$ MeV from S12 for all datasets	103
3.37	Fit to the average vertical angle for track vertices 750 \leq $p < 2750$ MeV from S18 for all datasets	103
3.38	Fit start-time scans for $A_{\rm EDM}$ Run-3b S12 using the full momentum range $750 \le p < 2750$ MeV and unmodulated plots. This scan uses a nine-parameter fit fixing ω_a and $\omega_{\rm CBO}$	104
3.39	Example results for CBO cross-check fits for Run-2 S12 $1500 MeV showing (a) number oscillation fit and (b) vertical angle fit$	105
3.40	Example CBO cross-check vertical angle oscillation amplitudes for Run-2 showing (a) in-phase and (b) out-of-phase amplitudes for both stations	106
3.41	The total covariance matrices for blinded data including (a) systematic uncertainties and (b) statistical and systematic uncertainties	108
3.42	The combination of individual results in each momentum bin, station, and Run. For each result, the inner error bar represents the statistical uncertainty and the outer the combined statistical and systematic uncertainty	108
3.43	Combination using results from each Run	109
3.44	Combination using results from each station	109
3.45	Combination checks after dropping individual results showing (a) the combined EDM value, (b) the χ^2 of the combination and (c) the pull. The x-axis is the result dropped from the fit and the final plot (d) shows the projection of the pull distribution	110
3.46	The contributions to the uncertainty on the combination from each systematic source. The total statistical uncer-	
	tainties are included for comparison	110

3.47	Contours showing the limits on true EDM $ d_{\mu} $ for a given measured EDM $ d $ (both normalised to σ) at the (a) 90% and (b) 95% CL. Three methods are shown: FC, a one-sided Gaussian, and a two-sided Gaussian where d_{μ} can be negative	111
A.1	C_{drift} for the exponential fit to the beam scraping effect on 3N for both stations	121
A.2	χ^2/NDF for the exponential fit to the beam scraping effect on 3N for both stations	121
A.3	Constant from the straight line fit after the beam scraping correction to 3N for both stations. A discussion of a potential reason for the systematic shift from zero is given in Section 3.1.4	122
A.4	χ^2/NDF for the straight line fit after the beam scraping correction to 3N for both stations	122
B.1	Fit start time scans for Run-2 S12 fit parameter $A_{\rm EDM}$, the red line indicates the 1σ allowed variation	124
B.2	Fit start time scans for Run-2 S18 fit parameter $A_{\rm EDM}$, the red line indicates the 1σ allowed variation	125
В.3	Fit start time scans for Run-3a S12 fit parameter $A_{\rm EDM}$, the red line indicates the 1σ allowed variation	126
B.4	Fit start time scans for Run-3a S18 fit parameter $A_{\rm EDM}$, the red line indicates the 1σ allowed variation	127
B.5	Fit start time scans for Run-3b S12 fit parameter $A_{\rm EDM}$, the red line indicates the 1σ allowed variation	128
B.6	Fit start time scans for Run-3b S18 fit parameter $A_{\rm EDM},$	129
B.7	the red line indicates the 1σ allowed variation Fit start time scans for Run-2 S12 fit parameter A_{g-2} , the red line indicates the 1σ allowed variation	130
B.8	Fit start time scans for Run-2 S18 fit parameter A_{g-2} , the	
B.9	red line indicates the 1σ allowed variation Fit start time scans for Run-3a S12 fit parameter A_{g-2} , the red line indicates the 1σ allowed variation	131
B.10	the red line indicates the 1σ allowed variation Fit start time scans for Run-3a S18 fit parameter A_{g-2} , the red line indicates the 1σ allowed variation	132 133
B.11	Fit start time scans for Run-3b S12 fit parameter A_{g-2} , the red line indicates the 1σ allowed variation	134
B.12	Fit start time scans for Run-3b S18 fit parameter A_{g-2} , the red line indicates the 1σ allowed variation	135
B.13	Fit start time scans for Run-2 S12 fit parameter C , the red line indicates the 1σ allowed variation	136
B.14	Fit start time scans for Run-2 S18 fit parameter C , the red line indicates the 1σ allowed variation	137
B.15	Fit start time scans for Run-3a S12 fit parameter C , the red line indicates the 1σ allowed variation	138
B.16	Fit start time scans for Run-3a S18 fit parameter C , the red line indicates the 1σ allowed variation	139
B.17	Fit start time scans for Run-3b S12 fit parameter C , the	140
	red line indicates the 1σ allowed variation	140

B.18 Fit start time scans for Run-3b S18 fit parameter C , the	
red line indicates the 1σ allowed variation	141

List of Tables

1.1	A summary of the transformation properties of \vec{B} , \vec{E} , $\vec{\mu}$ and \vec{d} under charge conjugation (C), parity (P) and time reversal (T)	24
3.1	Summary of frequencies of relevant oscillations for EDM analysis take from [27]. The frequency's name, its symbol, and frequency value for a field index $n = 0.108$ in the continuous ESQ approximation are outlined. Note that the measured frequencies differ slightly from the continuous ESQ approximation frequencies	61
3.2	Summary of the measured ω_{CBO} in each Run	63
3.2	The Gaussian spread and associated uncertainty from a fit	00
ა.ა	to the distribution of measured $A_{\rm EDM}$ for each station and momentum bin from 50 random seeds for vertical betatron	
	randomisation. These numbers are for the 3N dataset	87
3.4	Summary of the beam scraping systematics in momentum bins for Run-2 in S12 and S18 where ~ 0 indicates the	
	uncertainty is $< 0.005 \mu rad. \dots \dots \dots \dots$	88
3.5	Summary of the beam scraping systematics in momentum bins for Run-3a S12 and S18 where ~ 0 indicates the uncertainty is < 0.005 yrad	89
2.6	certainty is < 0.005 µrad	09
3.6	Summary of the beam scraping systematics in momentum bins for Run-3b S12 and S18 where ~ 0 indicates the uncertainty is $< 0.005~\mu rad.$	89
3.7	The difference in measured $A_{\rm EDM}$ after shifting the fitted $g-2$ phase by the difference from using 1600–1800 MeV for Run-2 S12 and S18, where \sim 0 indicates the uncertainty	
	is $< 0.005 \mu rad. \dots$	90
3.8	The difference in measured $A_{\rm EDM}$ after shifting the fitted $g-2$ phase by the difference from using 1600–1800 MeV for Run-3a S12 and S18	90
3.9	The difference in measured $A_{\rm EDM}$ after shifting the fitted $g-2$ phase by the difference from using 1600–1800 MeV for Run-3b S12 and S18, where ~ 0 indicates the uncertainty	
	is < 0.005 µrad	90
3.10	Results from weighted least squares minimisation to align the data- and acceptance-weighted all decays to the data-	
	weighted <i>true track</i> EDM values for each dataset and station.	93
3.11	The total (unitless) uncertainty on the acceptance for S12	=
	from combining all uncertainties in quadrature	94

3.12	The total (unitless) uncertainty on the acceptance for S18	
	from combining all uncertainties in quadrature	94
3.13	Summary of the track reconstruction uncertainty in each	
	momentum bin and Run. The same MC sample is weighted	
	to better match each Run	94
3.14	The all decays amplitudes and their uncertainties scaled to	
	the injected tilt of 1.69 mrad to give the reduction factor	
	$R_{e^+}(\lambda)$ and its uncertainty	96
3.15	Results of extrapolating the average radial field using the	
	Run-4 data measurement. Showing the average radial field	
	and the corresponding lab frame precession plane tilt for	
	each of the three datasets	96
3.16	Summary of the systematics on the rest frame tilt in mo-	
	mentum bins for Run-2 S12 and S18 where ~ 0 indicates	
	the uncertainty is $< 0.5 \mu rad. \dots$	98
3.17	Summary of the systematics on the rest frame tilt in mo-	
	mentum bins for Run-3a S12 and S18 where ~ 0 indicates	
	the uncertainty is $< 0.5 \mu rad. \dots$	99
3.18	Summary of the systematics on the rest frame tilt in mo-	
	mentum bins for Run-3b S12 and S18 where ~ 0 indicates	
	the uncertainty is $< 0.5 \mu rad. \dots$	100
3.19	A comparison of the rest frame tilts as measured using one	
	momentum bin 750–2750 MeV for each dataset and station	. 101
3.20	Summary of systematic uncertainties from each source.	
	Some sources are absolute uncertainties on $A_{\rm EDM}$, and	
	some are uncertainties on the R -factors and, as such, will	
	scale with the size of the measured amplitude as seen in	
	equation 3.2.8. Whether the uncertainties scale is indi-	
	cated in the table, alongside the correlations between mo-	
	mentum bins, stations, and datasets	107
3.21	Summary the combinations and their uncertainties	107

Chapter 1

Theory

1.1 The Standard Model of particle physics

The Standard Model (SM) of particle physics is a quantum field theory describing all currently known elementary particles (leptons and quarks) and three fundamental forces (electromagnetic, weak and strong). After the development of quantum mechanics and the Schrödinger equation, Dirac proposed a Lorentz invariant equation, that is linear in both energy and momentum, to marry the concepts of quantum mechanics and special relativity. It can be written¹

$$\mathcal{L} = \bar{\psi}(i\hbar c\partial \!\!\!/ - mc^2)\psi \tag{1.1.1}$$

where ψ is the Dirac spinor, and $\bar{\psi} = \psi^{\dagger} \gamma^{0}$ the Dirac adjoint. Feynman slash notation is used such that $\partial = \gamma^{\mu} \partial_{\mu}$ and ∂_{μ} is the 4-gradient. The Dirac equation implies the existence of antimatter, provides theoretical backing for Pauli's picture of spin and gives the equations of motion for relativistic quantum particles.

By making this quantum field theory have a gauge-symmetry such that the Lagrangian is gauge-invariant, one can formulate the theory of quantum electrodynamics (QED) that describes the electromagnetic (EM) interaction. The Lagragian is given by

$$\mathcal{L}_{\text{QED}} = \bar{\psi}(i\hbar c \not\!\!D - mc^2)\psi - \frac{1}{4\mu_0} F_{\mu\nu} F^{\mu\nu}$$
 (1.1.2)

where D is now the gauge covariant derivative $D_{\mu} = \partial_{\mu} - ieA_{\mu}, A_{\mu}$ is the electromagnetic four-potential, and $F_{\mu\nu} = \partial_{\mu}A_{\nu} - \partial_{\nu}A_{\mu}$ is the electromagnetic field tensor. This can be extended to include the weak interaction via electroweak (EW) gauge theory of Glashow, Salam and Weinberg (GSW). Including colour symmetry, the strong interaction between quarks is described by quantum chromodynamics (QCD). The gauge group for the SM is $SU(3) \times SU(2)_L \times U(1)_Y$.

The fundamental forces in the SM are mediated by gauge (vector) bosons with unit spin. Two of the gauge bosons are massless and have zero electric charge, these are the photon, the carrier of the EM force,

¹Generally, factors of c and h are left in derivations in this thesis but units are often given in natural units where $c = \hbar = 1$.

and the gluon, carrier the strong force and colour charge. With masses of 91.1 GeV/c^2 and 80.4 GeV/c^2 respectively, the Z and W^{\pm} are the bosons that carry the weak force. Massive bosons break gauge-invariance and W^{\pm} bosons are the only bosons to carry electric charge.

To explain the non-zero mass of the W and Z bosons, the weak isospin symmetry must be broken. This is done via the Higgs mechanism. The Higgs field is introduced with a non-zero vacuum expectation value, which gives the bosons and all other SM particles their mass. In this theory a scalar boson with zero electric charge, that couples to mass, is necessarily introduced. This is the Higgs boson, which has been measured with a mass of $125.2 \text{ GeV}/c^2$.

Fermions are spin-1/2 particles divided into 6 quarks and 6 leptons. They are structured in three generations of matter organised by weak doublets, with each generation having greater mass. Quarks interact weakly, electromagnetically, and carry a colour charge so also interact via the strong interaction. They cannot exist individually and bind to other quarks to create colourless hadrons. Leptons do not interact via the strong interaction but do interact via the weak interaction. The electron, muon and tau leptons interact electromagnetically - unlike the neutral neutrinos that only interact via the weak force.

Although the SM provides an excellent basis for understanding the fundamental particles and their interactions, it fails to explain several known phenomena. For example, there is no candidate to explain dark matter that is estimated to make up $\sim\!26.5\%$ of the total mass of the universe. Furthermore, in its original formulation the SM does not explain neutrino masses or their oscillations. However, their masses have been incorporated by introducing a right-handed neutrino field and interaction with the Higgs field that preserves gauge invariance. Additionally, there is no mechanism to account for the baryon asymmetry - the dominance of matter over antimatter in the universe.

1.2 Charge-parity violation in the Standard Model

Conservation of the combined CPT transformation must be assumed for a Lorentz invariant quantum field theory with a Hermitian Hamiltonian. The three individual transformations are: charge conjugation (C) - switching particles with their antiparticles; parity (P) - changing the sign of spatial coordinates; and time reversal (T).

In 1967, in light of the observed baryon asymmetry, Andrei Sakharov proposed three necessary conditions that an interaction must meet to create more matter than antimatter [1, 2]. These requirements are:

- Baryon number is violated.
- C symmetry and CP symmetry are violated.
- Interactions happen out of thermal equilibrium.

The first of these is necessary for the creation of matter, while C-symmetry violation ensures that baryon-producing reactions will not be balanced

by anti-baryon producing reactions. Then, CP violation is required so that left-handed baryons and right-handed anti-baryons (or vice versa) are not produced with the same probabilities.

Finally, interactions occurring out of thermal equilibrium mean that any asymmetry produced can be preserved, this would otherwise not be the case given CPT symmetry. In the early universe, the rate of baryon-producing reactions must be slower than the rate of expansion, such that particles can never reach thermal equilibrium with their antiparticles because pair production and annihilation rates are decreased.

Individually, QED and QCD are exact symmetries under each of these three operations, but the weak force can violate C and P due to its left-handed nature. The combination of C and P symmetries is also violated by the weak force. Parity violation in the weak interaction was discovered by Chien-Shiung Wu in 1957 [3].

Levels of CP violation from known sources are not sufficient to explain the baryon asymmetry observed. Indirect CP violation was first observed in kaon decay in 1964, earning the Cronin and Fitch the Nobel Prize for Physics [4], and has since been found in B meson and D⁰ decays [5, 6, 7, 8].

Within the SM, CP violation can arise due to a complex phase in the Cabibbo–Kobayashi–Maskawa (CKM) matrix, that describes the quark mixing probabilities, or in the Pontecorvo–Maki–Nakagawa–Sakata (PMNS) matrix describing neutrino mixing. For the CKM matrix, the complex phase is a free parameter and has been measured to be $\delta = 1.147 \pm 0.026$ rad [9]. To quantify CP violation without a dependence on phase convention, the Jarlskog invariant J is defined as

$$Im[V_{ij}V_{kl}V_{il}^*V_{kj}^*] = J\sum_{m,n} \epsilon_{ikm}\epsilon_{jln}.$$
 (1.2.1)

 V_{ij} are the matrix components and ϵ_{ijk} is Levi-Civita symbol. The Jarlskog invariant $J = 3.12^{+0.13}_{-0.12} \times 10^{-5}$ [9], demonstrating that the CP violation in the CKM matrix is reasonably well determined.

This is less so the case for the PMNS complex phase $\delta_{CP} \in [0, 2\pi]$, where values of 0 or 180° would give no CP symmetry breaking. The current best fit of $\delta_{CP} \sim 200^{\circ}$, implies some CP violation in neutrino oscillations, but with CP conservation $\delta_{CP} = 180^{\circ} = \pi$ rad allowed at 1-2 σ confidence level [9].

Alternatively, within the QCD Langragian the P- and T-odd term $\bar{\theta}$ would also provide a source of CP violation [10]

$$\mathcal{L}_{\bar{\theta}} = \bar{\theta} \frac{g_s^2}{32\pi^2} \operatorname{Tr}(G^{\mu\nu}\tilde{G}_{\mu\nu}), \tag{1.2.2}$$

where g_s is the strong coupling constant, $G^{\mu\nu}$ is the QCD field strength tensor and $\tilde{G}_{\mu\nu} = \epsilon_{\mu\mu\alpha\beta}G^{\alpha\beta}/2$. This term induces a electric dipole moment (EDM) in the neutron

$$d_n = C_{\text{EDM}}\bar{\theta},\tag{1.2.3}$$

where the coefficient is calculated via lattice QCD calculation or QCD sum rules. From experimental measurements of the neutron EDM the inferred limit is $\bar{\theta} \lesssim 2 \times 10^{-10}$, meaning the CP violation from the strong

1.3. Muons 1. Theory

force is incredibly small. With no obvious motivation for this particular value over any other in $[0, 2\pi)$, it is considered a fine-tuning issue called the strong CP problem.

1.3 Muons

The muon is a second generation fermion with a charge of $\pm e$, mass of 105.7 MeV/c^2 (207 times that of the electron), and a lifetime 2.2 µs [11, 9]. It was discovered in 1936 by Anderson and Neddermeyer at CalTech in a cosmic ray experiment [12], although it was probably first observed by Kunze in 1933, also in a cosmic ray experiment [13, 14].

The unique properties of the muon make it a useful experimental tool. Observation of time dilation by the Rossi-Hall experiment was made measuring muon decay lifetimes in the atmosphere [15]. Antimuons decay primarily via

$$\mu^+ \to e^+ + \nu_e + \bar{\nu_\mu},$$
 (1.3.1)

with the Feynman diagram shown in Figure 1.1. In muon decay, the phase space distribution of the decay electron, including energy and decay angle, can be described by the Michel parameters [16]. SM predictions and experimental measurements of these four parameters have so far been show to agree, which places constraints on BSM physics in the weak interaction (see e.g. [17, 18]).

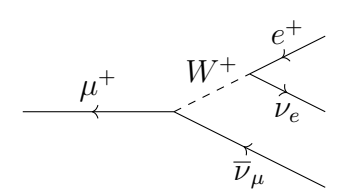


Figure 1.1: Feynman diagram for the decay of an antimuon to a positron and two neutrinos.

Some non-SM-allowed decays are searched for as evidence for new physics. Experiments are searching for evidence of charged lepton flavour violation (CLFV) by looking for decays such as $\mu^+ \to e^+ + \gamma$ at MEG, $\mu^+ \to e^+ + e^-$ at Mu3e, and muon to electron conversion in the presence of a nucleus $\mu^- N \to e^- N$ at Mu2e and COMET, see e.g. [19, 20, 21, 22].

1.4 Magnetic dipole moments

Any particle with spin has an intrinsic angular momentum. If the particle is also charged, it will have a magnetic dipole moment (MDM). The MDM $\vec{\mu}$ can be written as

$$\vec{\mu} = g \frac{q}{2m} \vec{s} \tag{1.4.1}$$

where q is the charge of the particle, m is the mass and \vec{s} is the spin vector. The g-factor is a dimensionless constant that characterises the coupling to the spin vector \vec{s} .

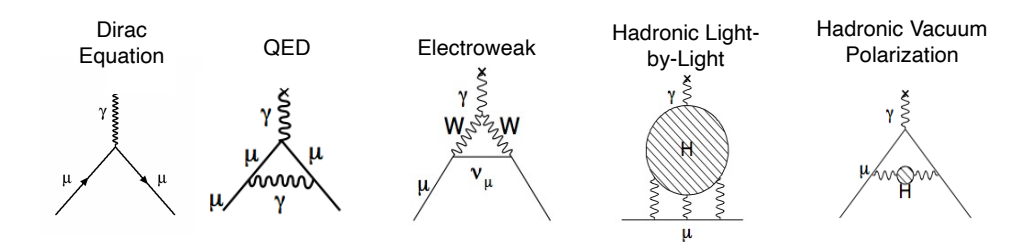


Figure 1.2: Five Feynman diagrams showing: the Dirac equation interaction giving g=2; and loop diagrams from QED, Electroweak and Hadronic interactions that contribute to a_{μ} .

The leading order Dirac equation predicts g=2 for the electron and other spin-1/2 particles [23]. After the measurement of the electron MDM by Kusch and Foley that found $g_e=2(1.00119+0.00005)$ [24], Schwinger showed that radiative corrections would also contribute to the value of g increasing it from 2 by $\alpha/2\pi$ [25]. These leading order contributions can be seen in the two leftmost Feynman diagrams in Figure 1.2. The contribution from other interactions leads to the definition of the anomalous magnetic dipole moment a_{μ} , that is the fractional difference of g from 2

$$a_{\mu} = \frac{g-2}{2}.\tag{1.4.2}$$

A summary of all the types of SM interactions can be seen in Figure 1.2 - they include interactions with photons, leptons, hadrons, and the W, Z, and Higgs bosons. For the electron, the electromagnetic interactions account for the majority of the contributions to g_e [26]. However, having mass 207 times that of the electron, the muon is 43,000 ($\approx m_{\mu}^2/m_e^2$) times more sensitive to heavy particle interactions, including beyond the standard model (BSM) interactions with new heavy particles [27]. Importantly, all particles in the SM contribute to the value of a_{μ} . As such, comparing SM predictions to experimentally measured values allows for a test of the SM and a potential probe of BSM physics.

The relative contributions to a_{μ} from the SM can be written as a sum of quantum electrodynamics (QED), electroweak (EW) and hadronic contributions

$$a_{\mu}^{\text{SM}} = a_{\mu}^{\text{QED}} + a_{\mu}^{\text{EW}} + a_{\mu}^{\text{Had}}.$$
 (1.4.3)

The hadronic contributions can be further separated into hadronic lightby-light (HLbL) and hadronic vacuum polarisation (HVP). Each of these contributions has an uncertainty based on SM calculations with the uncertainty on $a_{\mu}^{\rm HVP}$ dominating the total uncertainty.

SM predictions for HVP contributions are calculated in two ways; the dispersive method and lattice QCD method. The first uses measurements of $\sigma(e^+e^- \to \text{hadrons})$ to perform dispersion integrals over the cross section of the virtual photon, whereas the lattice QCD is an abinitio calculation that simulates the theory on a space-time grid. Only in the continuum limit of infinite grid size and zero lattice spacing is QCD recovered, so it can be very computationally expensive to achieve accurate results.

A series of experiments at CERN lay the groundwork for a precision measurement of a_{μ} , see e.g. [28, 29] and the references therein. Follow-

ing these experiments' principles, the anomalous magnetic moment of positive and negative muons was measured by the E821 collaboration at Brookhaven National Laboratory (BNL) giving a final precision of 0.54 ppm [30]. At the time, this was discrepant with the SM prediction by around three standard deviations. The first result from the E989 experiment at Fermi National Accelerator Laboratory (FNAL or Fermilab) was released in April 2021. This measurement of a_{μ} was consistent with BNL and had a precision of 0.46 ppm [31]. At the time, this was also discrepant with the SM prediction from the g-2 Theory Initiative White Paper [32]. The most recent results published in 2023 using Run-2/3 data increased the combined precision to 0.20 ppm [33].

However, between the first and second E989 releases, new SM calculations have called into question the recommended White Paper value. These include new experimental results that feed into the data driven method [34], and improvements in the precision of lattice calculations (e.g. [35]). Both give a_{μ} predictions that are closer to the experimental value. An updated SM number from the Theory Initiative and the final experimental result from Fermilab are both expected in 2025; this will provide one of the most stringent tests of the SM to date.

1.5 Electric dipole moments

In the simplest case of two point charges with a charge $\pm q$ separated by \vec{r} , the EDM is given by $\vec{d} = q\vec{r}$. A point-like particle such as a muon has no spatial extent, so classically it should have an EDM of zero. In the SM the EDM of a point-like particle is incredible small, but not zero due to quantum fluctuations polarising the vacuum around the particle. For bound states such as neutrons, whose internal charge structure should allow for an EDM, it is disallowed in the SM due to the CP symmetry in the strong interaction.

Any EDM must align with a point-like particle's one vector-like property, the spin \vec{s} . The EDM \vec{d} of a particle is given by

$$\vec{d} = \eta \left(\frac{q}{2mc}\right) \vec{s} \tag{1.5.1}$$

where c is the speed of light, q is the electric charge and m is the mass of the particle. Analogous to the g-factor in MDMs, η is a dimensionless constant that quantifies the coupling of the EDM and spin. For a spin-1/2 particle, it is given by the fundamental constants

$$\eta = \frac{4dmc}{q\hbar},\tag{1.5.2}$$

with

$$d = \vec{d} \cdot \hat{s}. \tag{1.5.3}$$

where \hat{s} is the spin unit vector.

The presence of a non-zero EDM would violate CP symmetry and be direct evidence for BSM physics. As mentioned, some amount of C and CP violation is required to satisfy Sakharov's second condition, but the levels currently observed are not enough to explain the matter-antimatter imbalance.

	\vec{B}	\vec{E}	$\vec{\mu}$ and \vec{d}
\overline{C}	-	-	-
Ρ	+	-	+
Τ	-	+	-

Table 1.1: A summary of the transformation properties of \vec{B} , \vec{E} , $\vec{\mu}$ and \vec{d} under charge conjugation (C), parity (P) and time reversal (T).

The only vector that can be constructed for a particle at rest is the spin vector, which is P-even but C- and T- odd. It is therefore odd under CP, a property which must be inherited by dipole moments (magnetic or electric). Furthermore, under CP transformation the magnetic field of a photon changes sign (CP-odd), but the electric field does not (CP-even); \vec{E} changes sign under parity as it is a polar vector, but not under time reversal. Considering the non-relativistic interaction Hamiltonian, which can be written as

$$\mathcal{H} = -\vec{\mu} \cdot \vec{B} - \vec{d} \cdot \vec{E}, \tag{1.5.4}$$

the magnetic field and MDM moment are both CP-odd and so CP is conserved in that part of the Hamiltonian. However, in the $-\vec{d} \cdot \vec{E}$ term CP is not conserved, as the transformation properties of the electric field and EDM do not match; \vec{E} is CP-even and \vec{d} is CP-odd. The Hamiltonian, then, is CP-violating in the case on a non-zero EDM.

This can be developed to the general spin interactions, that may be written as

$$\mathcal{L}_{MDM} = a_{\mu} \frac{e}{4m_{\mu}} \bar{\psi} \sigma^{\mu\nu} \psi F_{\mu\nu} \tag{1.5.5}$$

and

$$\mathcal{L}_{EDM} = -d_{\mu} \frac{i}{2} \bar{\psi} \sigma^{\mu\nu} \gamma_5 \psi F_{\mu\nu}, \qquad (1.5.6)$$

where $\sigma_{\mu\nu} = \frac{i}{2} [\gamma^{\mu}, \gamma^{\nu}]$ and $F_{\mu\nu}$ is the electromagnetic tensor [36]. Alternatively, this can be rearranged to give

$$\mathcal{L}_{EDM} = d_{\mu} \frac{1}{2} \epsilon^{\mu\nu\rho\eta} \bar{\psi} \sigma^{\mu\nu} \psi F_{\rho\eta}, \qquad (1.5.7)$$

from which it becomes apparent that the EDM term must be odd under P and T, due to the presence of the $\epsilon^{\mu\nu\rho\eta}$ Levi-Civita pseudo-tensor. The transformation properties of the fields and dipoles under C, P and T transformations are described in Table 1.1 and illustrated in Figure 1.3.

SM calculations for the EDM of the muon give $O(10^{-38}-10^{-35})$ e·cm [37, 38]. This includes SM-CKM induced contributions from the known Cabibbo-Kobayashi-Maskawa (CKM) matrix CP-violating phase [39] and SM- $\bar{\theta}$ contributions, where $|\bar{\theta}| \lesssim 10^{-10}$ based on the neutron EDM measurements [37].

At the same CERN experiments that measured a_{μ} , the EDM of the muon was measured, again developing an effective measurement concept [40] (outlined in Section 2.2.2). In due course, this led to the current best limit for the muon EDM to be set at BNL in 2009 [41], giving

$$|d_{\mu}| < 1.9 \times 10^{-19} \ e \cdot \text{cm}.$$
 (1.5.8)

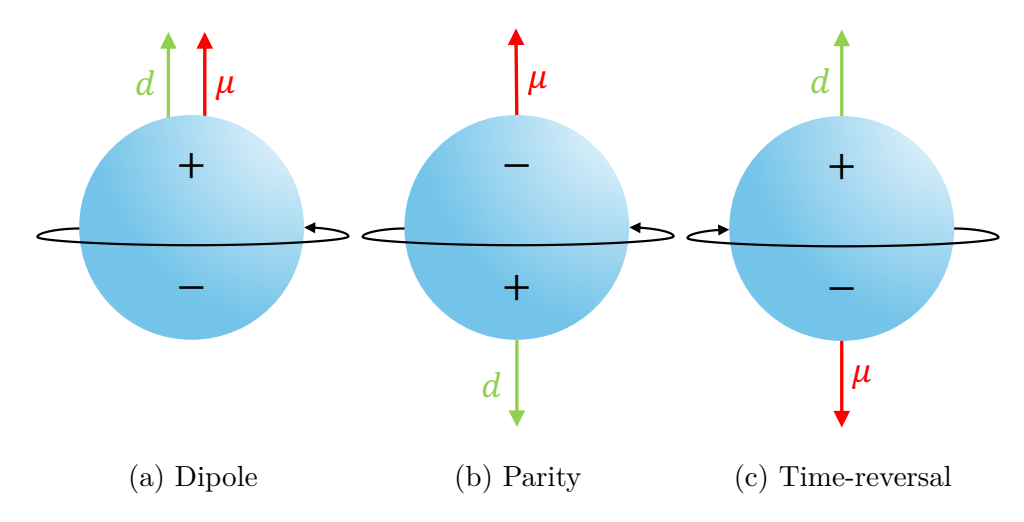


Figure 1.3: Illustration of (a) a dipole under (b) parity (P) and (c) timereversal (T) transformations showing that an EDM d violates both P and T symmetries.

This limit combines data from both μ^+ and μ^- decays, with the individual limits also consistent with zero. Notably, this limit is still many orders of magnitude above SM predictions as can be seen in Figure 1.4.

Indirect limits can be also be calculated via a simple mass scaling of the electron EDM $(d_{\mu}/d_{e} \approx m_{\mu}/m_{e})$ or using EDM measurements of heavy atoms and molecules. The first uses the assumption that the electroweak interaction is lepton flavour universal and, for the best current bound on the electron EDM from [42], gives $|d_{\mu}| < 4.1 \times 10^{-30} \times 207 = 8.5 \times 10^{-28}~e\cdot\text{cm}$. Recent results from the second method place indirect limits on the muon EDM around an order of magnitude smaller than those set at BNL with $|d_{\mu}| < 1.9 \times 10^{20}~e\cdot\text{cm}$ [43] and, notably, roughly equivalent to the final goal for Fermilab.

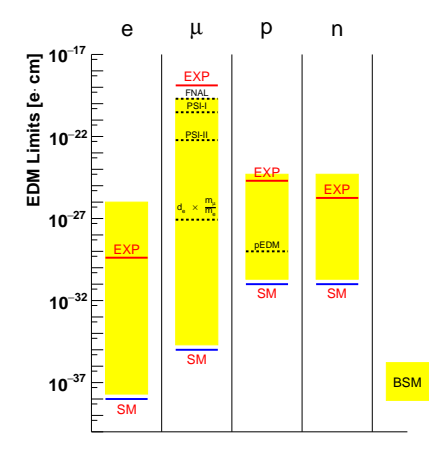


Figure 1.4: Summary of current best EDM limits for the electron, muon, neutron, and proton. SM predictions are included and a summary of various BSM theory predictions in yellow. The dashed lined represent expected limits from future experiments and the muon limit based on mass scaling using the electron EDM limit.

Doing a mass scaling of the electron EDM limit assumes lepton flavour

1.6. Summary 1. Theory

universality (LFU), which is an area that has recently received a lot of interest. Although there was some suggestion of lepton non-universality from LHCb measurements in 2021 [44] these have been succeeded by measurements that agree with SM LFU from differential branching fractions, e.g. [45], and rare decays e.g. [46].

However, there is no exact flavour symmetry in the SM as it broken in the gauge sector by the Yukawa interactions. As such, a minimal flavour violation (MFV) scenario can be hypothesised in which all flavour and CP-violating interactions are linked to the known structure of Yukawa couplings [47]. Similarly, this can be extended to the lepton sector to set the scale for potentially observable low-energy rare LFV processes [48].

Furthermore, non-zero EDMs are predicted in some dark matter models and improved limits can constrain the available parameter space [49, 50]. Generally, within supersymmetric models new CP-violating phases are introduced that give rise to CP-violating observables such as EDMs, see e.g. [51, 52]. Other BSM models that allow for EDMs at scales accessible by experiments include extra dimensions [53] and leptoquarks [54].

1.6 Summary

The SM is an invaluable framework that describes the fundamental particles and interactions. Yet, it is incomplete and cannot describe all experimental observations. The need for a mechanism to explain the baryon asymmetry motivates searches for CP-violating processes and EDMs of fundamental particles would contribute to this. Their measurements serve as precision tests of the SM and help put limits on BSM parameter space. A direct measurement of the muon EDM has not been completed since 2009, and the improvements in hardware and statistics at Fermilab Muon g-2 compared to BNL allow for an improvement in this. Overall, it is important to continue to scrutinise the SM in all sectors.

Chapter 2

Experimental Methods

The Muon g-2 experiment at Fermilab aims to measure the anomalous magnetic moment of the muon to 140 ppb. The measurement method is based on the principle first developed for the CERN III experiment [55]. Positive muons are stored in a 7.112 m radius superconducting storage ring magnet (pictured in Figure 2.1) and the decay positrons are measured. This is the same ring used at the predecessor experiment at BNL, with upgrades to the magnetic field instrumentation. Every 1.4 s 16 bunches of muons are delivered to the storage ring. This results in ~ 5000 stored muons per bunch, with momentum 3.094 GeV, and momentum RMS of 0.15%.

The rest of this chapter describes the measurement principles and experiment by firstly considering spin precession in external fields. The methods for measuring a_{μ} and the muon EDM are then discussed, including a consideration of the sensitivity of the EDM search. Following this, the experimental techniques and the setup at the Fermilab Muon g-2 experiment are explained, with a focus on the components that are most relevant for the EDM search. Subsequently, the simulation implementation, which is used to characterise detector acceptance and alignment, is set out. Lastly, techniques to measure any radial component of the storage ring magnetic field are outlined, with regard to the potential for generating a EDM-like signal.

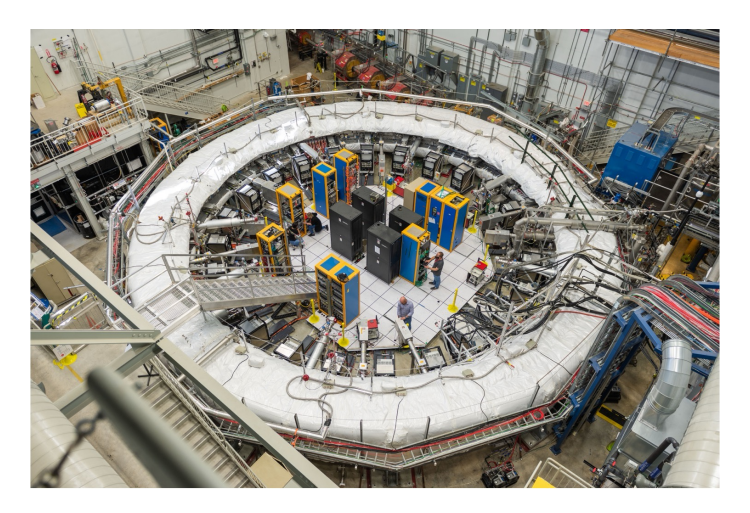


Figure 2.1: Picture of the storage ring in the experiment hall at FNAL. The white covering is insulation to minimise temperature fluctuations in order to keep the magnetic field more stable.

2.1 Spin precession

Moments can be measured using the principles of spin precession, which is defined as $d\vec{s}/dt = \vec{\omega}_s \times \vec{s}$, where \vec{s} is the spin vector, t is time and $\vec{\omega}_s$ is the spin precession frequency. In an external magnetic field the MDM $\vec{\mu}$ experiences a torque causing the spin to precess. The torque $\vec{\tau}$ on the MDM is given by

$$\vec{\tau} = \vec{\mu} \times \vec{B},\tag{2.1.1}$$

where \vec{B} is the external magnetic field. Then, the rate at which the spin precesses (for a muon at rest in a magnetic field) is called the Larmor frequency

$$\vec{\omega}_L = -g \frac{q}{2m} \vec{B},\tag{2.1.2}$$

which is proportional to g and the magnetic field. Similarly, the EDM will experience a torque in an electric field \vec{E} ,

$$\vec{\tau} = \vec{d} \times \vec{E}.\tag{2.1.3}$$

This causes the spin to precess with frequency

$$\vec{\omega}_{\eta} = -\eta \frac{q}{2m} \vec{E},\tag{2.1.4}$$

which is, correspondingly, proportional to η and the electric field.

For the case of a relativistic particle, the effects of Thomas precession must also be included. The effect arises from non-commutativity of Lorentz transformations; due to the relativistic kinematics of moving in a curve, the spin will precess [56, 57]. Thomas precession is given by

$$\vec{\omega}_T = -\frac{\gamma^2}{\gamma + 1} \vec{\beta} \times \frac{d\vec{\beta}}{dt} \tag{2.1.5}$$

where γ is the Lorentz factor and β is the ratio of the particle's velocity to the speed of light. An external force must be applied for the acceleration (with the condition the force does not produce a torque on the particle) - this could come from any source including gravitational or electromagnetic.

For a particle moving in external electric and magnetic fields the spin precession is described by the Bargmann–Michel–Telegdi (BMT) equation [58] (sometimes called the Thomas-BMT (T-BMT) equation). Including the torques on the MDM, EDM and Thomas precession discussed above, the spin precession is given by [59]

$$\vec{\omega}_{s} = -\frac{q}{mc} \left[\left(a + \frac{1}{\gamma} \right) c\vec{B} - \frac{ca\gamma}{1+\gamma} \left(\vec{\beta} \cdot \vec{B} \right) \vec{\beta} - \left(a + \frac{1}{1+\gamma} \right) \vec{\beta} \times \vec{E} + \frac{\eta}{2} \left(\vec{E} - \frac{\gamma}{1+\gamma} \left(\vec{\beta} \cdot \vec{E} \right) \vec{\beta} + c\vec{\beta} \times \vec{B} \right) \right],$$
(2.1.6)

where the electric field \vec{E} and the magnetic field \vec{B} are in the lab frame. It can be noted that for the EDM term in Equation 2.1.6, the first term is simply the effect of a lab frame electric field. Next, there is a term that

quantifies the effect of motion in the longitudinal directions. Finally, the Lorentz transformation of a lab–frame magnetic field into the muon rest frame (MRF) gives rise to the term $\vec{\beta} \times \vec{B} = \vec{E}^*$, where E^* denotes the rest frame electric field. Importantly, for a relativistic particle only in a lab frame magnetic field, there is rest frame electric field exerting a torque on the EDM. With a swapping of the fields, parallel arguments can be made for the terms dependent on the anomalous moment a.

Also, it can be seen that setting $\eta=0$ will recover the BMT spin precession in the absence of an EDM as is assumed for the measurement of the muon anomalous magnetic moment a_{μ} in Section 2.2.1. Under ideal conditions for storage ring experiments the particle moves transverse to the electric and magnetic fields so that $\vec{\beta} \cdot \vec{B} = 0$ and $\vec{\beta} \cdot \vec{E} = 0$ and the equation is further simplified.

2.2 Measurement principles

2.2.1 a_{μ} measurement principle

Relativistic muons¹ are stored in a dipole magnet storage ring with field \vec{B} and focusing electric field \vec{E} . For g > 2 the spin will precess faster than the cyclotron frequency. The difference between the spin frequency $\vec{\omega}_s$ and cyclotron frequency $\vec{\omega}_c$ can be measured to give the anomalous precession frequency $\vec{\omega}_a = \vec{\omega}_s - \vec{\omega}_c$.

The cyclotron frequency is given by

$$\vec{\omega}_c = \frac{q}{mc\gamma} \left(\frac{\hat{\beta} \times \vec{E}}{\beta} - c\vec{B} \right), \qquad (2.2.1)$$

and, assuming $\eta=0$ for now, can be combined with the Equation 2.1.6 to give

$$\vec{\omega}_a = -\frac{q}{mc} \left[a_\mu c \vec{B} - \left(a_\mu - \frac{1}{\gamma^2 - 1} \right) \vec{\beta} \times \vec{E} - \frac{a_\mu c \gamma}{\gamma + 1} (\vec{\beta} \cdot \vec{B}) \vec{\beta} \right]. \quad (2.2.2)$$

Here q is the charge, m is the mass, β is the ratio of the velocity to speed of light, and γ is the Lorentz factor. By choosing $\gamma = \sqrt{1 + (1/a_{\mu})}$, it is possible to cancel the term proportional to \vec{E} . This Lorentz factor corresponds to the 'magic momentum' where $p_0 \approx 3.094$ GeV/c. With no vertical motion and exclusively vertical magnetic field, the final term in this equation also cancels.

Under these conditions the spin will precess in a plane defined by a normal vector parallel to \vec{B} . Consequently, the anomalous spin precession frequency reduces to

$$\vec{\omega}_a = -\frac{q}{m} a_\mu \vec{B} = -\frac{q}{m} a_\mu B \hat{y}. \tag{2.2.3}$$

where we have assumed a vertical magnetic field $\vec{B} = B\hat{y}$. This is illustrated in Figure 2.2. Thereby, in this idealised case, it is clear that a measurement of ω_a and B allows the anomalous magnetic moment to be extracted

¹Muon is used for antimuon throughout this thesis unless there would otherwise be ambiguity.

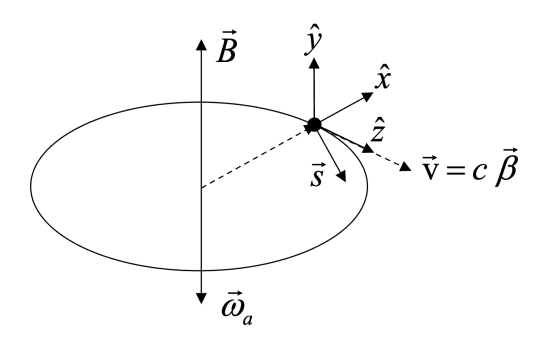


Figure 2.2: Illustration of a muon in storage ring, undergoing circular motion with spin precessing in \hat{x} - \hat{z} plane. Courtesy of P. Debevec.

In practice, the magnetic field is given in terms of the measured NMR frequency of protons $\tilde{\omega}'_p$ in a spherical water sample at a reference temperature,

$$\tilde{\omega}_p' = \gamma_p'(T_r)\tilde{B} \tag{2.2.4}$$

where γ'_p is the gyromagnetic ratio of protons in H₂O at temperature T_r , and \tilde{B} represents the magnetic field averaged over the muon distribution in time and space. Using Equations 2.2.3 and 2.2.4, a_{μ} can be written as

$$a_{\mu} \propto \frac{\omega_a}{\tilde{\omega}_p'(T_r)} \equiv \mathcal{R}_{\mu}'(T_r),$$
 (2.2.5)

where we have defined the a_{μ} as a ratio of frequencies - the \mathcal{R} value.

The measurement of ω_a relies on the parity violation in the weak decay of the muon. Consider that at the maximum positron energy the neutrinos are emitted parallel to each other, with zero total angular momentum, and the positron is emitted at 180°, carrying all the muon's angular momentum. This positron is favourably right-handed due to the V-A weak decay and so it is preferentially emitted parallel to the muon spin in the MRF. The opposite is true for the lowest energy positrons [60].

In the lab frame the energy spectrum is modulated at ω_a , such that there are more high energy positrons when the spin is aligned with the momentum, compared to when it is anti-aligned. If all decays could be counted the distribution would simply show the exponential decrease. However, by applying a cut on the lab frame energy of the positron it is possible to select a subset of decays where the number of positrons is oscillating with frequency ω_a .

The simplest function to extract ω_a is a five parameter fit function to the oscillation in number of positrons

$$N(t) = N_0 e^{\frac{-t}{\gamma \tau_{\mu}}} \left(1 - A_N \cos \omega_a t + \phi_a \right), \qquad (2.2.6)$$

where t is time, N_0 is the normalisation factor, τ_{μ} is the muon lifetime, A_N is the asymmetry and ϕ_a is the phase. With no energy cut the distribution would just be an exponential decrease in number of positrons as the muons decay. This gives the first term in the equation. The asymmetry quantifies the change in the number of electrons above the threshold energy as the spin precesses around and is dependent on the chosen energy cut. The phase is the initial phase of the muon spins relative to the

momentum. In the real case, this fit is expanded to up to 38 parameters to account for beam dynamics effects including muon losses, coherent betatron oscillations (CBO) and vertical waist [27]. These effects are elaborated on in Section 2.3.1.

2.2.2 EDM measurement principle

The effect of a non-zero EDM is now included in the context of the experimental setup designed for the measurement of a_{μ} . With an EDM there is an additional contribution to the spin precession frequency due to the term dependent on η in Equation 2.1.6, such that $\vec{\omega}_s \to \vec{\omega}_s + \vec{\omega}_{\eta}$. By extension

$$\vec{\omega} = \vec{\omega}_a + \vec{\omega}_\eta, \tag{2.2.7}$$

where the total anomalous spin precession frequency is now labelled $\vec{\omega}$ and an EDM will modify this frequency by a small amount in both magnitude and direction compared to the case described in Section 2.2.1.

Using the BMT equation (2.1.6) and neglecting any E field in the lab frame², the contribution to the spin precession from an EDM is

$$\vec{\omega}_{\eta} = -\eta \frac{q}{2mc} \left(\vec{\beta} \times B \right) = -\eta \frac{q}{2mc} \beta B \hat{x}. \tag{2.2.8}$$

As in Section 2.2.1, an ideal storage ring with vertical magnetic field $\vec{B} = B\hat{y}$ has been assumed, and with longitudinal momentum $\vec{p} = p\hat{z}$, it follows that that $\vec{\beta} \times \vec{B} = -\beta B\hat{x}$. This additional frequency is orthogonal to $\vec{\omega}_a$ as given in Equation 2.2.3 and its inclusion causes the spin precession plane to be tilted relative to the zero EDM case. A vertical component to the precession plane is introduced as the normal vector is now aligned with $\vec{\omega} = \vec{\omega}_a + \vec{\omega}_{\eta}$. An illustration of this can be seen in Figure 2.3.

This tilt in the precession plane can be written as

$$\delta = \tan^{-1} \frac{\omega_{\eta}}{\omega_{a}} \approx \frac{\omega_{\eta}}{\omega_{a}} = \frac{\beta \eta}{2a_{\mu}}, \tag{2.2.9}$$

where a_{μ} is the anomalous magnetic moment of the muon and using the small angles $\omega_{\eta} \ll \omega_{a}$ which is valid based on expected ω_{a} and the muon EDM limit. Taking this with Equation 1.5.2, the EDM of the muon is related to the rest frame tilt by

$$d_{\mu} = \frac{q\hbar a_{\mu}}{2m_{\mu}c\beta}\delta,\tag{2.2.10}$$

demonstrating that the EDM is proportional to the tilt in the spin precession plane.

Subsequently, assuming the spin and momentum are initially aligned and there is zero EDM, the spin will precess in time t as

$$\hat{s}(t) = -\sin \omega t \,\,\hat{x} + \cos \omega t \,\,\hat{z}. \tag{2.2.11}$$

²Assuming $\beta \approx 1$, and $|\vec{B}| = 1.45 \text{T}$ a lab-frame electric field of $|\vec{E}| \sim 435 \text{MV/m}$ is needed to satisfy $|\omega_{\eta}| = \omega_a$. The effect of the quadrupole electric field $(|\vec{E}| \sim 1.8 \text{kV/m})$ is therefore neglected.

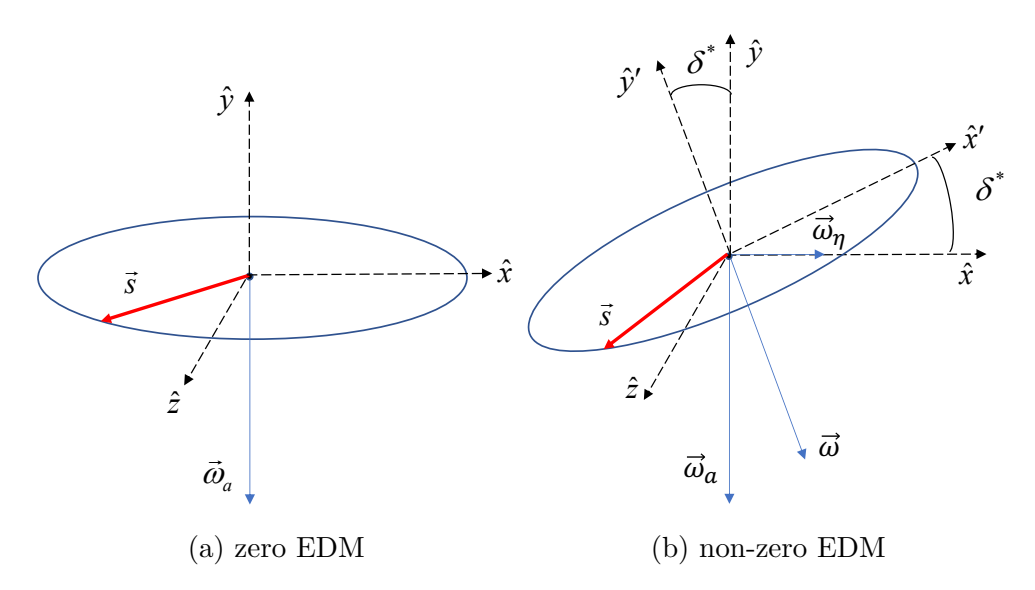


Figure 2.3: Illustration of the spin precession plane for an antimuon when (a) there is no EDM and the spin precesses in the \hat{x} - \hat{z} plane, and (b) when there is a non-zero EDM and the precession plan is the tilted. Courtesy of P. Debevec.

With the introduction of an EDM, the spin vector will precess as

$$\hat{s}(t) = -\cos \delta^* \sin \omega t \ \hat{x} - \sin \delta^* \sin \omega t \ \hat{y} + \cos \omega t \ \hat{z}, \tag{2.2.12}$$

where δ^* is the angle the precession plane makes with horizontal as in Figure 2.3b and * denotes the muon rest frame. From this, it is apparent that when the spin vector is longitudinal - aligned or anti-aligned with \hat{z} such that $t = n\pi/\omega$ for $n \in \mathbb{N}$ - there can be no sensitivity to an EDM. In addition, the vertical component is maximal when $\sin \omega t$ is maximal - at $t = (2n+1)\pi/2\omega$ for $n \in \mathbb{N}$, giving $\hat{s} = \pm(\cos \delta^* \hat{x} + \sin \delta^* \hat{y})$.

Considering Equation 2.2.12, when the vertical component of the spin is maximal, there is no component in \hat{z} . Hence, the vertical decay angle of the positron will be maximal when the spin vector is orthogonal to the momentum. On the other hand, the anomalous precession oscillation is maximal when the spin vector is parallel to the momentum. Therefore, the average vertical decay angle of positrons will oscillate at ω , but be maximised $\pi/2$ out of phase with the anomalous precession oscillation. A measurement of the amplitude of this oscillation will give access to the tilt and, thus, the muon EDM.

2.2.3 EDM measurement in the lab frame

To understand the vertical decay angle as seen in the lab frame, take a positron emitted parallel to the maximally vertical spin vector. Its momentum is $\vec{p}^* = p^* \cos \delta^* \ \hat{x} + p^* \sin \delta^* \ \hat{y}$ in the MRF and $\vec{p} = p^* \cos \delta^* \ \hat{x} + p^* \sin \delta^* \ \hat{y} + \gamma \beta E^* \hat{z}$ in the lab frame. Then, define the vertical decay angle θ_y as the lab frame angle between the positron momentum and the \hat{x} - \hat{z} plane,

$$\sin \theta_y = \frac{p_y}{p}.\tag{2.2.13}$$

It follows that

$$\sin \theta_y = \frac{p_y}{\sqrt{p_x^2 + p_y^2 + p_z^2}} = \frac{p^* \sin \delta^*}{\sqrt{p^{*2} + \gamma^2 \beta^2 (p^{*2} + m_e^2)}},$$
 (2.2.14)

using the small angle approximation and taking $m_e \approx 0$ this simplifies to

$$\theta_y \approx \frac{\delta^*}{\gamma}.$$
 (2.2.15)

Hence, at the maximal vertical emission, the lab frame vertical decay angle is proportional to the precession plane tilt.

This can be generalised to show that the angle of emission in the muon rest frame is always reduced by a factor of γ in the lab frame. The scaling between the rest frame tilt and the observed angle in the lab frame is represented in this analysis by the reduction factor

$$R_{\gamma} = \frac{1}{\gamma}.\tag{2.2.16}$$

Alongside this, the measurement of g-2 utilises a highly polarised beam, but it is not perfect; from accelerator simulations of the muon campus the average muon beam polarisation is predicted to be 96% [61].³ This has impacts on measured values within the EDM analysis - it decreases the amplitude of the number oscillation and the amplitude of the EDM oscillation. The first change is absorbed into the number normalisation and does not affect the measured EDM, but the second must be accounted for. For this reason, another reduction factor R_P is introduced that is not momentum dependent and is equal to the average polarisation P of the muon beam

$$R_P = P = 0.96. (2.2.17)$$

Additionally, there is a reduction due to tracker acceptance $R_{\rm acc}(\lambda)$ that is documented fully in Section 2.4.2 and is momentum dependent. In brief, it occurs as the trackers do not reconstruct all vertical decay angles with equal probability.

2.2.4 Sensitivity to an EDM

The final factor needed to correctly convert the amplitude of the oscillation in $\langle \theta_y \rangle$ as measured in the lab frame to a rest frame tilt is more complicated, and comes from the decay properties of the muon. It is detailed in this section.

The relative sensitivity to an EDM as a function of momentum is investigated using a similar approach to the ω_a analysis. In order to minimise the fractional uncertainty in ω_a , the number distribution multiplied by the decay asymmetry squared should be maximised [60]. Unique to the EDM analysis, is that the asymmetry is instead defined in the up or down decays. This derivation uses only Born-level equations, and thus does not account for higher order contributions, it also assumes $|\beta|=1$ and $m_e=0$.

³This value is not given with an associated uncertainty, but one must be chosen for the analysis as it impacts the measured EDM (See Section 3.2.9).

To begin with, take the probability density of positron emission as a function of time given a tilted spin precession plane [62]

$$P(\lambda^*, \theta^*, \phi^*, t) \propto n(\lambda^*) \left(1 + a(\lambda^*) \cos \alpha^*(\theta^*, \phi^*, t)\right), \tag{2.2.18}$$

where $\lambda^* = E/E_{max}$, θ^* is the angle between the positron momentum \vec{p} and the z-axis in the MRF. Then, ϕ^* is the angle between the x-axis and the projection of \vec{p} to the x-y plane such that $\tan \phi^* = p_x/p_y$ and α^* is the angle between the muon spin vector and \vec{p} . Finally, $n(\lambda^*)$ and $a(\lambda^*)$ are the number density and decay asymmetry in the muon rest frame given by [60]

$$n(\lambda^*) = 2\lambda^{*2}(3 - 2\lambda^*), \tag{2.2.19}$$

and

$$a(\lambda^*) = \frac{2\lambda^* - 1}{3 - 2\lambda^*}. (2.2.20)$$

After time averaging, integrating (with $\lambda^* \in [\lambda, 1)$), and transforming to the laboratory frame, the number of positrons is given by

$$N(\lambda) = \frac{1}{6\pi} (1 - \lambda)(5 + 5\lambda - 4\lambda^2), \tag{2.2.21}$$

where N is integral over a volume element and the normalisation is chosen so that the integral over all λ is one. Similarly, the decay asymmetry can be transformed into the lab frame to determine a figure of merit for the ω_a analysis

$$A(\lambda) = \frac{8\lambda^2 - \lambda - 1}{-4\lambda^2 + 5\lambda + 5}.$$
 (2.2.22)

For the EDM analysis an up-down asymmetry in the lab frame A_{\pm} is defined, where the \pm simply differentiates this from the decay asymmetry. It is given in terms of the number of decays above (N_{+}) and below (N_{-}) the $\hat{x} - \hat{z}$ plane:

$$A_{\pm}(\lambda) = \frac{N_{+} - N_{-}}{N_{+} + N_{-}} = -\frac{8}{5} \frac{\sqrt{\lambda(1-\lambda)}(1+4\lambda)}{5+5\lambda-4\lambda^{2}}.$$
 (2.2.23)

As with the ω_a , the statistical figure-of-merit (FOM) is then

$$N(\lambda)A^{2}(\lambda) \propto \frac{\lambda(1-\lambda)^{2}(1+4\lambda)^{2}}{5+5\lambda-4\lambda^{2}}.$$
 (2.2.24)

and visualised in Figure 2.4, indicating that the statistical sensitivity to an EDM is greatest at middling positron energies.

For a tilted precession plane, where the average vertical decay angle is being considered, the boost to the lab frame becomes significant. The maximum vertical decay angle in the lab frame is momentum dependent, with smaller maxima at higher energies. An explanation of this based on kinematics is given in Appendix B of [63].

Considering both the asymmetry and the Lorentz transformation of the vertical decay angle, the expression for the average vertical decay angle in the laboratory frame for decays occurring at the maximum tilt is

$$\langle \theta_y \rangle (\lambda) \propto \frac{(\lambda - 1)(2\lambda + 1)}{4\lambda^2 - 5\lambda - 5} \delta.$$
 (2.2.25)

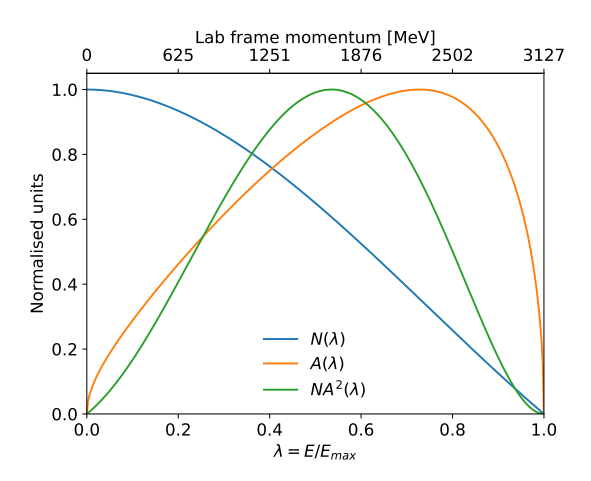


Figure 2.4: The number function $N(\lambda)$, EDM asymmetry function $A_{\pm}(\lambda)$ and statistical Figure-of-Merit $NA^{2}(\lambda)$ in the lab frame.

This is a second reduction of the tilt when measured in the lab frame. Thus, another factor $R_{e^+}(\lambda)$ is defined, with e^+ denoting that the reduction arises from the decay properties given to the positron,

$$R_{e^{+}}(\lambda) = \frac{(\lambda - 1)(2\lambda + 1)}{4\lambda^{2} - 5\lambda - 5}.$$
 (2.2.26)

This analytical form of the reduction due to decay properties is illustrated in Figure 2.5 and due to the approximations used in the derivation, is only valid for $\lambda > 0.1$.

Equation 2.2.26 is indicative of the observed behaviour but not exact. More precise values for this reduction must take into account radiative corrections where $\mu^+ \to e^+ \nu_e \bar{\nu}_\mu \gamma$, and include both initial and final state radiation where the photon is real or virtual [64, 65, 66]. In the end, the reduction is found using MC as outlined in Section 3.2.8.

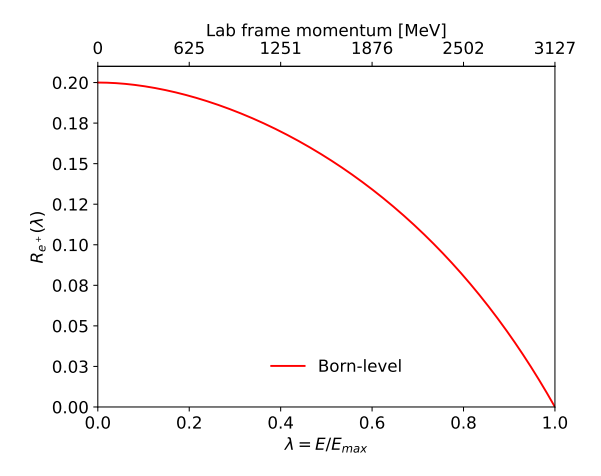


Figure 2.5: Reduction in the average vertical angle in the lab frame at point of maximum tilt in the MRF $R_{e^+}(\lambda)$.

In summary, the measured amplitude of the oscillation in the lab frame, labelled $A_{\rm EDM}$, is reduced from the rest frame tilt via four mechanisms giving

$$A_{\rm EDM} = R_{\gamma} R_P R_{e^+}(\lambda) R_{\rm acc}(\lambda) \delta^*. \tag{2.2.27}$$

Further details on the calculation of $R_{e^+}(\lambda)$ and $R_{\rm acc}(\lambda)$ are presented in Section 2.4 and the associated uncertainty for the reduction factors are presented in Section 3.2.

2.3 Experimental setup

The measurement of g-2 requires a highly polarised beam that is achieved by exploiting the decay nature of pions. Charged pions decay via the weak interaction into a muon and muon neutrino via

$$\pi^+ \to \mu^+ + \nu_{\mu}.$$
 (2.3.1)

with a branching fraction of 0.999877 [67]. As the pion spin is zero and the neutrino is left-handed, the antimuon must be right-handed such that the spin is antiparallel to the neutrino spin. For a moving pion, the momentum of the muon can be 'forward' or 'backward' relative to the pion momentum in the centre-of-mass frame. The forward or backward muons have distinct energies and different spin directions so, by selecting either the highest or lowest energy muons, a highly polarised beam can be isolated [60]. Muon g-2 uses forward going antimuons with polarisation opposite to their lab frame momenta.

The Fermilab Muon Campus delivers 16 bunches of highly polarised muons every 1.4 s, which is divided into two sets of 8 bunches totalling O() muons [61]. Each bunch has an average energy of 3.094 GeV with initial spread of 1.6% and is around 120 ns long [60]. Collimators confine stable orbit muons so that approximately 5000 are stored per 700 µs fill with an RMS of $\sim 0.15\%$.

The muons travel around in a 7.112 m radius superconducting dipole magnet - a cross section showing the C-shape of the magnet is shown in Figure 2.6. The ring is made of 12 segments of iron yoke, around which are four liquid helium-cooled superconducting coils that produce a strong vertical field. Using the pole pieces, wedges, edge shims, 'top hats' (shim plates), surface iron foils, and correction coils, the magnetic field is tuned to increase its homogeneity and symmetry in the storage region. After the first data-taking run, thermal insulation was added around the ring to improve temperature stability, thereby increasing magnetic field stability.

Just prior to entering the storage ring the muons pass through a plastic scintillating detector read out by photomultiplier tubes (PMTs). This gives the injection a time reference, or T_0 . Then, the muons pass through the inflector beam monitoring system (IBMS), which is comprised of two scintillating fibre grids and a set of vertical-only fibres connected to silicon photomultipliers (SiPM). The grids characterise the beam profile at injection and the latter is only deployed for systematic studies, to avoid degrading the beam. These systems are shown at 0° in Figure 2.7.

At the point of entry an inflector magnet locally zeroes the magnetic field such that the muons can enter tangentially. After injection, the muons are displaced outward from the magic radius by 77 mm. To correct for this, three pulsed kicker magnets at $\sim 90^{\circ}$ from the point of injection are used to briefly reduce the magnetic field and deflect the muons onto

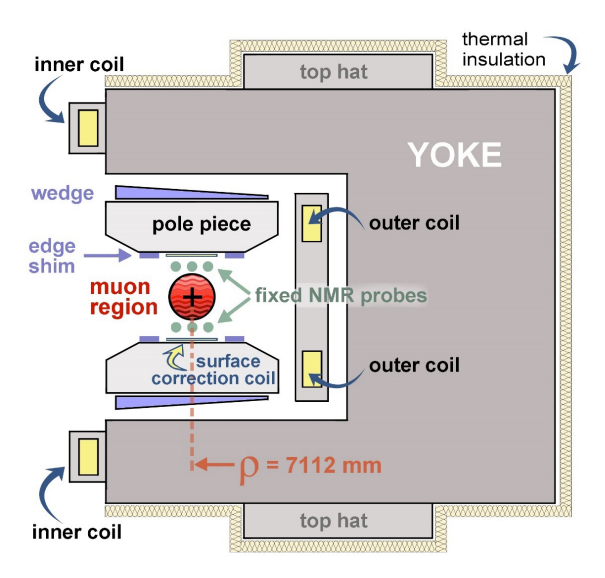


Figure 2.6: A cross section of the storage ring dipole showing the storage region and the various tools for making minor adjustments to improve the magnetic field uniformity.

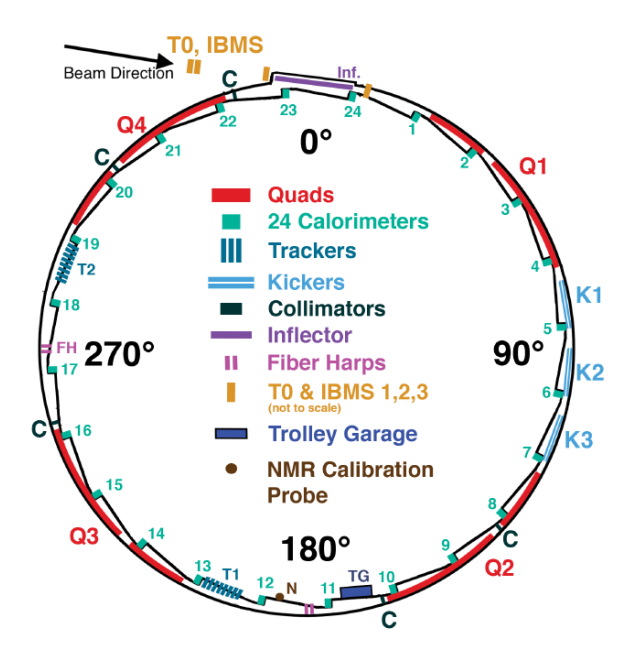


Figure 2.7: A schematic drawing of the storage ring including the systems for muon injection and focusing, as well as the detectors.

the central radius. There is some transient magnetic field from eddy currents that last beyond the initial kick and must be characterised to account for any effect on ω_a .

Further, to vertically focus the beam there are four electrostatic quadrupoles (ESQs). Each ESQ plate is charged before injection and pulses for the whole period of the fill to keep the voltage stable. The ESQs are also used for beam scraping - they displace the beam just after injection in order to remove muons at the edge of the beam that would be potentially lost during the fit period. The bottom plates' voltage is lowered to move the beam down, and an inner and outer ESQ plate on opposite sides of the ring are lowered to move the beam radially. With the beam shifted, edge muons collide with collimators and are scattered out of the storage ring, which 'scrapes' off the outermost muons before the beam is returned to its nominal position.

In order to reach the precision goals for the determination of a_{μ} , the muon weighted magnetic field must be known to 70 ppb [60]. This is achieved using a movable trolley with 17 NMR probes that can traverse around the storage ring while there is no beam, measuring the azimuthal and transverse magnetic fields in the storage region. These measurements are synchronised with 378 fixed NMR probes that sit above and below the storage region and continue to track the field during data taking. The magnetic field measurements must also be weighted to the beam distribution to ascertain the magnetic field experienced by the muons.

Decay positrons are detected by two types of detectors. Primarily, there are 24 calorimeters spaced evenly around the ring that are made up of lead fluoride crystals producing Cherenkov radiation to be detected by silicon photomultipliers (SiPMs) [68, 69]. This achieves sub-ns timing resolution in order to separate positron events. Secondly, there are two straw tracker detectors that sit in-vacuum, upstream of two calorimeters. Having two trackers allows for more of the beam to be measured and helps to minimise impacts of beam dynamics (see Section 2.3.1). For the purposes of the analysis presented here, they are the means of making the measurement. Thus, additional details of the straw tracker detectors are presented in the Section 2.3.2.

These detectors are readout by the data acquisition (DAQ) systems that utilise Graphical Processing Units (GPUs) to handle rates up to 20 GB/s and are based on the Maximum Integrated Data Acquisition System (MIDAS) software [70]. Data are combined in bunches of muon fills that last around 700 μ s called events, which contain around 2000 hits from the calorimeters. Subsequently, roughly 100 events are stored in each raw file, which are further grouped every 500 files into runs⁴ each being ~ 1 TB [71]. Datasets are collections of runs categorised based on beam and field conditions and there are 84 in total.

Data production consists of pre- and full-production, where the preproduction is required to perform calibrations and data quality checks (DQCs), and full-production completes the final reconstruction for all detectors. Calibration constants are determined using light reconstruction for each muon fill, alongside completing DQCs at the fill level. After

 $^{^4}$ Note than a run refers to this group of ~ 500 sub-runs, but a Run is the total data taken during each year of beam time from autumn to spring

a test is validated to check for any remaining issues on around 10% of the data, full-production is completed for the dataset. A final round of quality checks removes about 1% of positron events and the remaining files are used for analysis.

The Muon g-2 experiment at Fermilab collected data from May 2018 to July 2023, which are divided into 6 Runs. Each Run is separated by a lab-wide summer shutdown which pauses accelerator facilities in the main complex at Fermilab for maintenance and upgrades. Data from Run-2/3 is used for the EDM search presented here. There were damaged resistors in Run-1 that introduced time dependent issues and it is a much smaller dataset. For Run-4/5/6, data production was not complete when this analysis began, hence it is not included either.

2.3.1 Beam dynamics effects

During a muon fill there are several beam oscillation frequencies introduced as a result of the beam conditions. The observation of such frequencies depends on their relation to detector acceptance. Some of these are important sources of systematic uncertainty in the ω_a analysis and have to be characterised with corrections or extra fit parameters. Here, the mechanisms are described briefly, with implications for the EDM analysis discussed in Section 3.1.3 and assessed as systematic uncertainties in Section 3.2.

Due to the short injection time (120 ns), there is a modulation of detected positrons in individual calorimeters at the cyclotron period T_c , which is called fast rotation. The momentum spread of the stored muon causes the initial bunching to gradually spread out azimuthally as the high momentum muons have to travel further to complete one cyclotron orbit, meaning the lower momentum muons move ahead and eventually catch up. This causes the 'fast rotation' signal to decohere over the period of the fill. Effects from this are reduced when data from all the calorimeters are combined and by using other analysis methods as discussed in Section 3.1.

Charged particles in a storage ring will undergo transverse oscillations called betatron oscillations caused by focussing elements, namely, the ESQs. As muons move away from the ideal radial or vertical position, they experience a force from the ESQs restoring them towards the correct orbit and causing them to oscillate about the ideal orbital position. The muons undergo both vertical (f_y) and radial (f_x) betatron oscillations. As the muons pass the detector once per cyclotron period, the oscillation in radial centroid is observed at a frequency $f_{\text{CBO}} = f_c - f_x$, where CBO stands for coherent betatron oscillations.

Leading effects of the CBO are modelled by adding a perturbation to the N_0 term of Equation 2.2.6

$$N_x(t) = 1 + A_{\text{CBO}}e^{-t/\tau_{\text{CBO}}}\cos(\omega_{\text{CBO}} + \phi_{\text{CBO}})$$
 (2.3.2)

with parameters describing the CBO amplitude A_{CBO} , frequency ω_{CBO} , phase ϕ_{CBO} , and decoherence time constant τ_{CBO} . As the muon bunch spreads out around the ring during a fill, the amplitude of the CBO oscillation reduces or *decoheres*. As visible in Figure 2.8, the CBO is

responsible for the largest peak in the ω_a fit residuals if not accounted for.

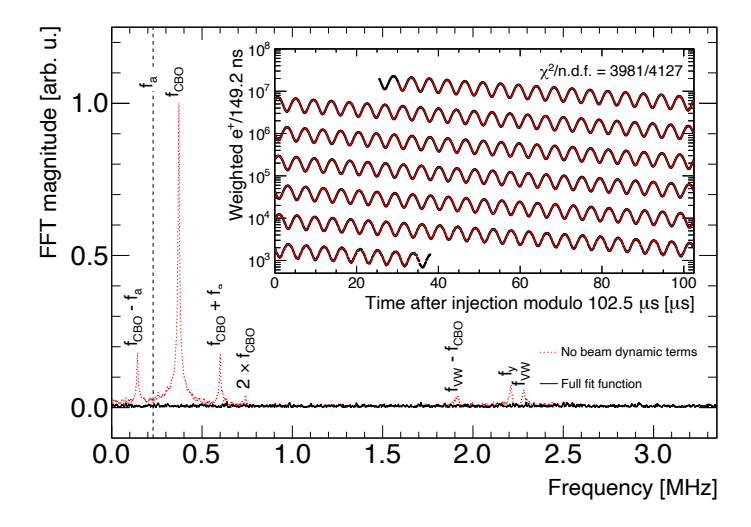


Figure 2.8: Fourier transform of the residuals from a fit following Equation 2.2.6 (red dashed line) and from the full fit (black line). The peaks correspond to the missing betatron frequencies and muon losses. Data are from the Run-3a data set. Inset: corresponding asymmetry-weighted e^+ time spectrum (black line) with the full fit function (red line) overlaid. Caption adapted and figure taken from [33].

Relevant to the EDM search, the vertical betatron (VB) motion introduces an oscillation in the observed $\langle \theta_y \rangle$ because the angular acceptance is highly dependent on the beam's vertical position. However, in the anomalous precession frequency plots, the vertical width oscillation is observed at $f_{\rm VW} = f_c - 2f_y$ called the vertical width (VW) and is visible as a peak in Figure 2.8.

2.3.2 Straw trackers

There are two straw tracker stations at 180° (station 12 or S12) and 270° (station 18 or S18) from the point of muon injection. They are designed to monitor the muon beam distribution by sitting in vacuum ahead of two calorimeters. As such, they must be non-magnetic, with low leak-rate, and only minimally reduce the positron energy [72].

Each of these tracker stations (illustrated in Figure 2.9) is made up of 8 modules consisting of 4 layers with 32 straws per layer. One of these modules can be seen in Figure 2.10. Each module has dimensions $426 \times 191 \times 93$ cm³, with the straws being 10 cm long with a 5 mm outer diameter. Alternating straw layers are aligned at $\pm 7.5^{\circ}$ from the vertical to improve the vertical resolution. The trackers are in vacuum and, to minimise any material effects, the straws are made of aluminised Mylar. Each straw contains a central tungsten cathode and is filled with a 1:1 ratio of argon and ethane. Argon is the ionisation gas and ethane acts a quencher to absorb photons and prevent new avalanches.

When a positron passes through a tracker straw it ionises the gas within it. The liberated electrons then drift to the central wire and, in the high E-field near the wire, avalanche, producing a signal. Above a

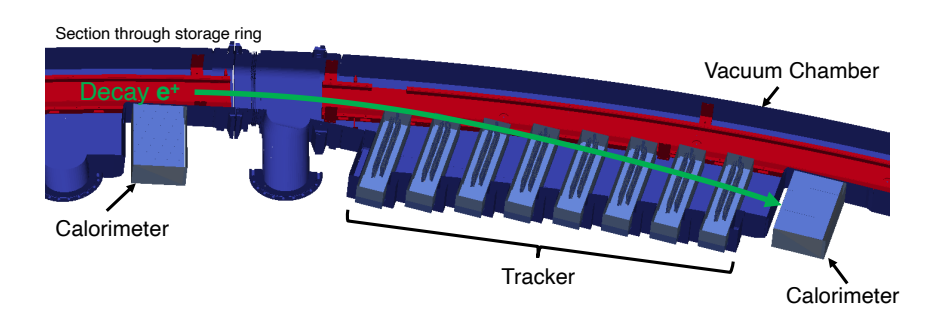


Figure 2.9: A top down view of a tracker station in the storage ring. The decay positron travels inwards towards a calorimeter, passing through the straw tracker modules.



Figure 2.10: One tracker module containing 4 layers of 32 straws. A tracker station is made up of 8 of these modules.

configured threshold, these hits are read out and the hit time t_h recorded. Hits are grouped together in time islands of 80 ns to find the track candidates for fitting. This time island is chosen to be longer than the maximum drift time - the time taken for the liberated electrons to travel to the wire in a straw. Within a time island, information on the position and time is used to group hits into track candidates.

Firstly, the fit to a track candidate must determine the arrival time of the positron t_0 . In short, this is done by utilising the relationship between the hit time, the time taken for the electrons to drift to the wire t_d , and the arrival time, such that $t_0 \approx t_h - t_d$. In reality, the t_0 method (outlined in detail in [73]) first calculates the angle of incidence ($\theta = p_x/p_z$) for hits in adjacent layers. This pair of hits is called a doublet. Within a doublet a left-right index is defined describing whether the positron passed to the left or the right of the wires e.g. LL, RR, LR, RL. Importantly, before the fit there is no momentum information, so θ must be estimated by fitting a circle to the track candidate hits.

Then, the fact that the sum of the drift times in a doublet $t_{\rm ds}$ has a linear relationship to θ is used:

$$t_{\rm ds} = \frac{\theta - P_1}{P_0},\tag{2.3.3}$$

where P_0 and P_1 are determined for each LR combination. This allows for an estimate of t_0 via

$$t_0 = \frac{t_{\rm hs} - t_{\rm ds}}{2} \tag{2.3.4}$$

where $t_{\rm hs}$ is the sum of the hit times in the doublet. For large and small

angles the LR ambiguity is harder to determine, so the mean drift time is instead subtracted giving

$$t_0 = t_{\rm hs} - \langle t_{\rm d} \rangle. \tag{2.3.5}$$

This average drift time $\langle t_{\rm d} \rangle$ is estimated using tracker data by taking the time between tracker and calorimeter hits, adjusted for time of flight. It is calibrated separately for each LR combination at large and small angles of incidence.

From the drift time, the distance of closest approach (DCA) of the positron to the wire (as shown in Figure 2.11) can be calculated via a conversion polynomial, which is discussed in more detail in Section 2.3.3. The track is then fit following a GEANE (Geometry and Error Propagation) method. The set of hits defines objects such as transport matrices, error matrices, and predicted parameter vectors using the full g-2 Geant4 software [74] based on initial guesses. This takes account of the tracker geometry and material, as well as the non-uniformity of the magnetic field. The track objects are passed through a global chi-squared minimisation algorithm to give a optimal vector at the track entry point defining the track.

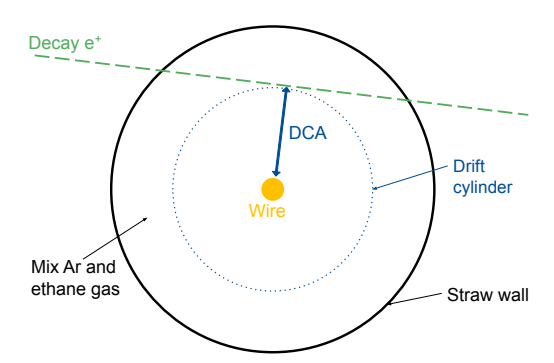


Figure 2.11: A cross-section of a straw indicating the distance of closest approach (DCA) of the positron.

Once fitted, the track is extrapolated forwards to the calorimeters and backwards to the point of tangency - when the radial momentum is zero. This point is used as a proxy for the decay position (decay vertex), assuming the positron is emitted parallel to the muon momentum. Forwards extrapolation provides information on pile-up and is used to measure the tracking efficiency. Moreover, the backward extrapolation allows for a measurement of the positron 3-momentum and position, to characterise the muon beam distribution.

2.3.3 Improving the tracking efficiency

DCA calibration

There were several improvements made to the tracking algorithm between Run-1 and Run-2/3 to help improve the tracking efficiency. Firstly, the drift time to distance of closest approach (DCA) conversion - which uses a fifth order polynomial fit for each layer and each station - is recalibrated for Run-2/3. This polynomial is determined using the DCA and

drift time information from tracks that have the layer-to-be-calibrated dropped from the track fit. An example of this relation can be seen in Figure 2.12.

By taking time slices and fitting the projection of the DCA with a Gaussian, a set of data points are created for the fit. An example of this projection fit is shown in Figure 2.13. The data points and the fifth order polynomial fit are shown for an example run in Figure 2.14. The fifth order fit is chosen to minimise residuals compared to lower order fits.

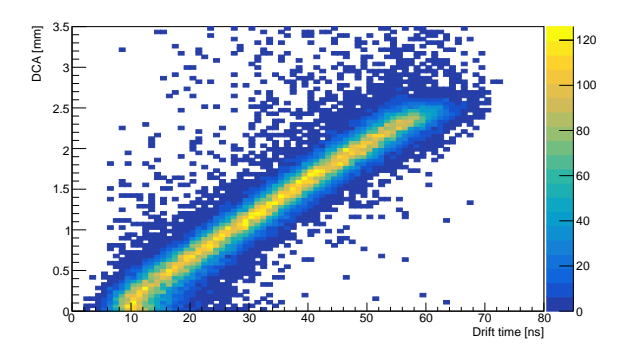


Figure 2.12: Example of a 2D histogram of drift time and DCA for layer 49 in run 15921. The colour axis shows the number of entries.

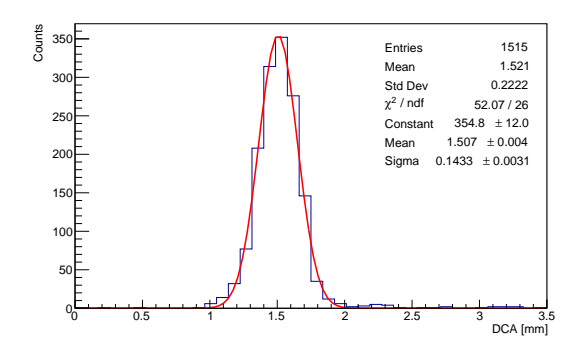


Figure 2.13: Example of the Gaussian fit to the projection of DCA for a slice in drift time around 40 ns for layer 49 in run 15921. The histogram statistics are shown above the fit results.

Hit width

For a given straw hit there is an associated width that is the length of time the signal is above the threshold value. A cut can be applied to this hit width to help reduce the number of bad hits at the track candidate level and improve the tracking efficiency. Most of these hits are cross-talk and the distribution of widths can be seen in Figure 2.15, where the cut is chosen to be 14 ns. This cut was previously optimised using tracker studies from earlier Runs, but was not implemented as it contributes to a loss of tracks early in the fill.

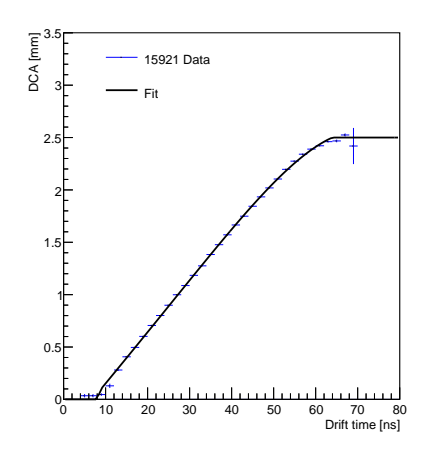


Figure 2.14: Example of the fifth order polynomial fit to the DCA calibration in for layer 49 in run 15921. The $\chi^2/\text{NDF}=4.8$, which is larger than the ideal 1 and is probably caused by the difficulty in fitting drift times for positrons that pass very near the edge of the straw or near the central wire.

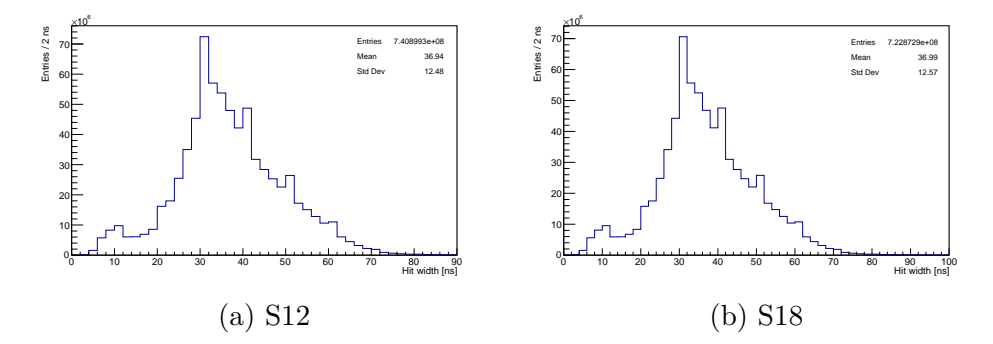


Figure 2.15: The hit width distributions for each station with 0 < t < 300 µs from a subset of data in Run-3. The impact of cross-talk can be seen in the peak at at low hit width, with good hits peaking around 30 ns width.

Fill-time dependent measures

At the start of the fill there are many tracker hits from lost muons, positrons and some protons. The high hit rate gives rise to a space charge effect where ions created during the electron avalanches are drifting slowly back to the straw wall, reducing the E-field near the wire. This leads to a drop in tracking efficiency early in the fill, but levels off around 50μ s. Adding a hit width cut exacerbates this as it is likely too stringent at early times when the E-field near the wire is reduced. Further, the space charge effect changes the drift time of positrons, meaning the DCA calibration described above is not as accurate early in the fill.

To account for this, the size of the DCA uncertainty is scaled exponentially with fill-time such that there is greater leeway in the track fitting. This increases the efficiency at early times so it is flatter over the fill. The uncertainty scaling factor for both stations can be seen in Figure 2.16. Uncertainties in station 12 have larger scaling as this station sees a greater drop in efficiency because of its proximity to the muon injection point. The efficiency over a fill after implementing this scaling can be seen in Figure 2.17, where there is an improvement at early times. This efficiency measures the percentage of successfully reconstructed quality decay vertices, where their track candidate coincides with a calorimeter cluster.

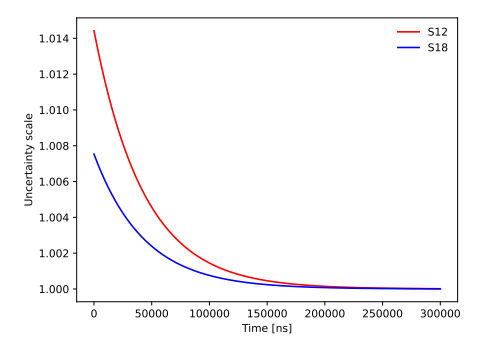


Figure 2.16: The scaling applied the uncertainty on the DCA for stations 12 and 18.

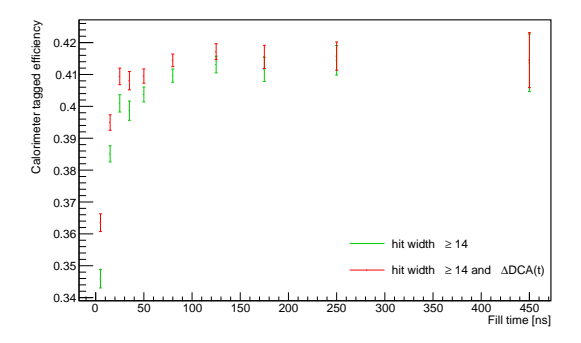


Figure 2.17: A comparison of the quality vertex tracking efficiency in station 12 with a hit width cut versus with both a hit width cut and the fill-time dependent uncertainty on the DCA. The results are alike in station 18.

Other improvements

After the initial track fit, all tracks have any hits with large residuals cut to remove noise. The residual in this case being the difference between the predicted position of a positron in a straw based on the DCA and the position in the final track fit. The time the positron entered the tracker t_0 is then recalculated without these hits to minimise all remaining hit residuals and the whole track fit repeated.

One of the quality cuts on reconstructed tracks described in Section 2.3.4 requires the track p value p>0.05. As part of the tracking efficiency improvements, tracks that do not meet this criteria are refitted with the four most likely L-R combinations and the best fit kept. This allows tracks that would have previously failed QCs to potentially be saved for use in analysis. With all these tools in place, we see a quality vertex track efficiency of $\sim 42\%$ compared to the $\sim 14\%$ efficiency previously achieved from the Run-2/3 production tracking as used in [33].

2.3.4 Quality cut adjustment

After the track reconstruction, various cuts are applied to select the tracks used for analysis. There are cuts at the hit level, track level and decay vertex level (the end point of backwards extrapolation). If a track passes all of these cuts it is referred to as a quality vertex (QV) track. As part of this analysis, the nominal cuts were adjusted from those used in beam studies and other parts of the ω_a analysis.

Once the tracks have been refitted, the quality cuts (QCs) are extended to maximise the efficiency for the EDM analysis while maintaining quality of tracks and ensuring MC continues to describe the data well. The two changes are that the minimum number of hits required is reduced from 12 to 11 and the maximum fraction of tracker straw layers missing a hit is increased from 0.3 to 0.4. These final changes increase the total number of tracks by 13% in the range 750 - 2750 MeV. There is no efficiency in relation to calorimeter matching for this as it is done post track production, but, naively, the efficiency would increase from 42% to $\sim 47\%$.

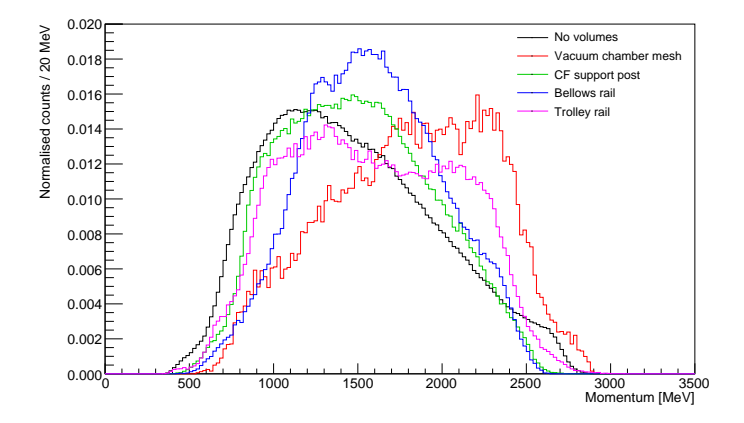


Figure 2.18: Comparison of momentum distributions in data for tracks that hit no volumes and tracks hitting the four most commonly hit volumes.

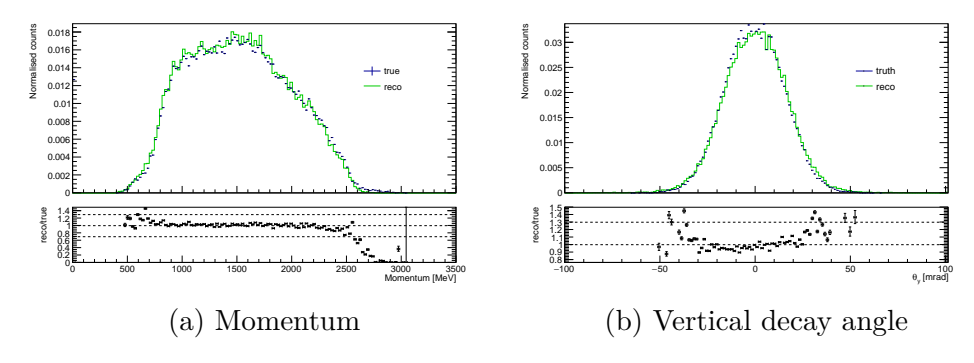


Figure 2.19: The distributions and residuals for *true tracks* and *reco tracks* that hit the carbon fibre post and pass all other QV cuts for (a) momentum and (b) vertical decay angle.

The biggest loss in tracks after these improvements is due to the cut on tracks that hit a volume, which requires that positrons did not pass through material before reaching the trackers. This rejects almost half the tracks. Indeed, most of these volume interactions cause too much scattering for the tracks to be viable for analysis. However, there is potential to use tracks which pass through the small and light the carbon fibre (CF) support post (which supports the end of each tracker module and can be seen in Figure 2.10). These tracks have similar beam distributions and acceptable residuals compared to nominal QV tracks. An example of the momentum distributions for several commonly hit volumes can be seen in Figure 2.18. The momentum and vertical decay angle residuals for the CF post are shown in Figure 2.19.

Including tracks that hit the support post for analysis would improve the statistics by around 10%, but would also require a more thorough investigation, including a consideration of the changes in acceptance and momentum. Given the expected statistical limitation on the EDM search, it is still worth exploring any potential gains in the number of tracks.

2.4 Simulation

2.4.1 EDM in simulation

Simulation is an essential tool for verifying methods, assessing systematics, and characterising detector acceptance. This analysis benefits from a high-statistics Monte Carlo simulation made using the g-2 simulation package gm2ringsim based on GEANT4 software [74]. Within this, muon decay times are randomly sampled from an exponentially decreasing distribution. Based on the time (taken as time since the injection), the energy-momentum four-vector, position, and polarisation of the muon are calculated. The muon is then considered to decay instantaneously at the calculated position in the ring and the positron is extrapolated to the detectors.

For the EDM analysis, three types of MC event are considered from the output of this simulation. The *all decays* sample includes the information from every decay positron produced in the sample. *Reconstructed* (reco) track vertices includes all the tracks successfully reconstructed

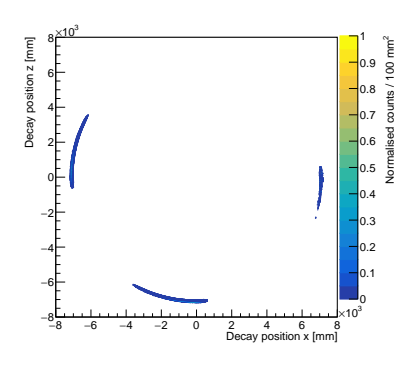


Figure 2.20: Azimuthal decay positions for reco track vertices in MC showing an acceptance of $\sim 25^{\circ}$ in azimuth.

from the total positron sample and extrapolated back to the decay vertex. Then, the *true track vertices* simply uses the truth information for this reconstructed set of vertices.

The all decays sample is uniformly distributed around the ring and the track vertices come from three separate straw tracker stations. The first tracker station, referred to as station 0 (S0), exists only in simulation is positioned 0° from the muon injection point and has 'perfect' alignment, making it a useful reference. Stations 12 and 18 are located as in the experiment setup outlined in Section 2.3.2 and they include a relative alignment based on pre-Run-1 measurements [75]. Each of these tracker stations has an acceptance of $\sim 25^{\circ}$ azimuthally as seen in Figure 2.20⁵.

An EDM is added to this simulation by introducing an oscillating vertical component to the muon polarisation vector [76]. The injected signal is set to $d_{\mu} = 5.4 \times 10^{-18} e \cdot \text{cm}$, which is $30 \times$ the upper limit set at BNL, to ensure the signal is large enough to be seen given the statistics generated.

2.4.2 Tracker acceptance

Due to the locations and dimensions of the tracker stations, only a subset of the total positrons are detected. To characterise the tracker acceptance, MC is used to compare the track distributions to the distributions from *all decays* and, ultimately, translated to a difference in the measured EDM.

From Figure 2.21 it can be seen that the measured EDM amplitude is reduced in the reco track vertices compared to that measured in the all decays, especially at low momentum. This arises because at lower momentum the spread in θ_y is greater and the tracker acceptance is higher for small vertical decay angles as seen in Figure 2.22. Therefore, the EDM amplitude is underestimated most at low momentum where the tracker is seeing fractionally less of the minimal and maximal decay angles.

The simplest method to obtain the acceptance factor would be to take the ratio of EDM amplitudes from *track vertices* to *all decays* and use this to scale the measured amplitude in data back to the true value

⁵A bug in the MC reconstruction meant S0 tracks were not reconstructed properly and hence the azimuthal acceptance is reduced.

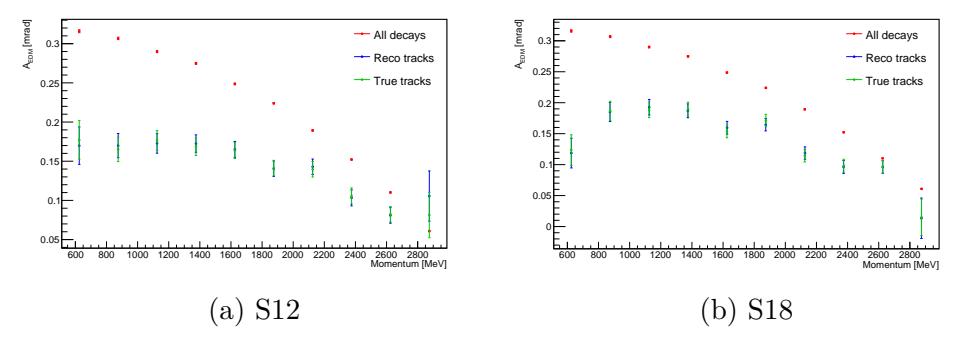


Figure 2.21: Fitted EDM amplitude for each momentum bin for *all decays*, reco track vertices and true track vertices. Due to acceptance effects, the measured amplitude from track vertices is reduced compared to the *all decays* amplitude.

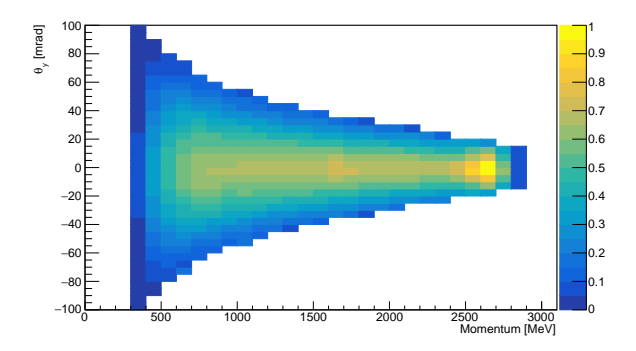


Figure 2.22: Acceptance of vertical angles in momentum from MC with injected EDM of $5.4 \times 10^{-18}~e \cdot \mathrm{cm}$. The z axis is normalised so that the peak is at 1.

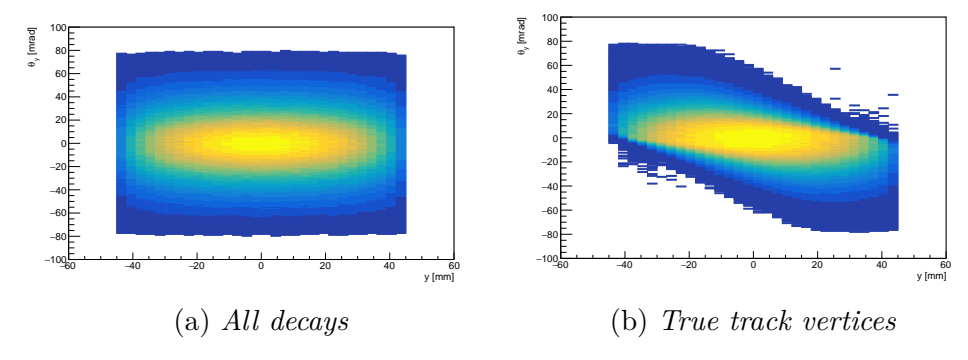


Figure 2.23: The vertical angle θ_y and vertical decay position y in the momentum range 500 - 3000 MeV for the (a) all decays sample and (b) true track vertices, demonstrating the effects of tracker acceptance.

if all decays were detected. However, this method is limited due to the statistical error on the amplitude from the MC track vertices as seen in Figure 2.21. The solution is to apply an acceptance 'map' to the larger all decays sample, such that each event is weighted by the vertical decay angle θ_y and vertical position y of the track vertices. The difference in the 2D distributions can be seen in Figure 2.23, where the all decays distribution is near Gaussian, compared to true track vertices, which shows a distinct correlation between θ_y and y.

After weighting the *all decays* sample, the EDM analysis is repeated using this larger dataset, decreasing the uncertainty on the EDM amplitudes. These amplitudes after weighting are assumed to represent the true value expected to be measured by the trackers. Any systematic uncertainties this assumption and method may introduce are detailed in Section 3.2.7.

The procedure for producing and using these acceptance maps consists of five steps:

- Produce 2D distributions of θ_y and y for true track vertices and all decays in each momentum bin.
- Take the ratio of these to create an acceptance map such that each histogram bin has the value $b_{i,j}^{map} = b_{i,j}^{true}/b_{i,j}^{all\ decays}$.
- Weight each event in the *all decays* sample using the corresponding bin value, including a bilinear interpolation within the map and linear interpolation between maps for each momentum bin.
- Use the weighted sample to repeat the EDM analysis.
- Take the ratio of the weighted to the unweighted all decays EDM to give the acceptance reduction.

This is the primary method to reduce the statistical uncertainty on the acceptance, however one also has to consider how well the simulation matches the data. The 2D distributions, as in 2.23, vary slightly between data and MC and this is further exaggerated by the use of an unrealistic beam shape (see Section 2.4.3). To account for this, there is an additional weighting of the *true track vertices* to data before the maps are created. In a similar way to the maps, the weighted distributions are made with these steps:

- Produce 2D distributions of θ_y and y for true track vertices and data in each momentum bin.
- Take the ratio of these such that the new histogram has bin values $b_{i,j}^{weight}=b_{i,j}^{data}/b_{i,j}^{true}$.
- Reproduce the θ_y and y distributions for true track vertices weighting each vertex to the corresponding bin, including a bilinear interpolation between histogram bins and linear interpolation between momentum bins.

Ultimately, the *true track* distributions after weighting to data are used to produce the acceptance maps. Given that the data distributions vary slightly between datasets, there is a unique acceptance value for each.

2.4.3 Updates to simulation

The acceptance correction for the EDM analysis is based on maps parameterised in vertical angle and position. To ensure sufficient MC statistics to populate these maps at the extremes of the vertical position, the MC beam was adjusted from nominal settings: the beam distribution was flattened in y, and the simulated collimators removed. The beam distribution in y after this adjustment can be seen in Figure 2.24 with a 10-20 times improvement in stats at the highest and lowest vertical positions. It is worth noting, however, that these modifications pull the beam characteristics further from the real world case and the impacts of this must be quantified as part of the acceptance studies.

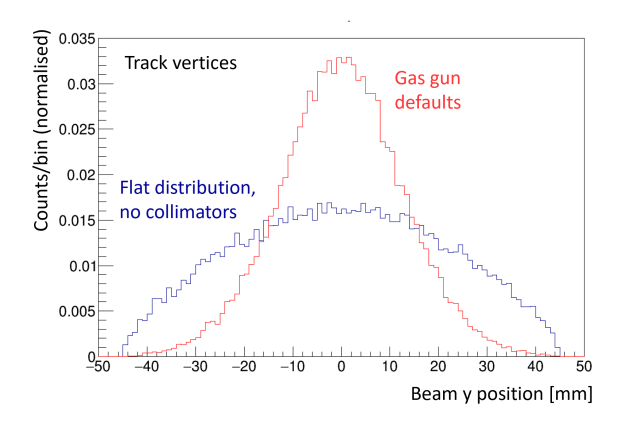


Figure 2.24: The vertical beam distributions from MC track vertices using the default gas gun settings (red) and the flattened distribution used for the EDM analysis (blue).

The model used to calculate a drift time for a given DCA was updated for this MC production. Previously, a straight line was used to convert the DCA to a drift time assuming a fixed drift velocity. The updated method uses a fifth order polynomial to model this relation and this fit is done for each tracker layer in stations 12 and 18. Similarly to the reverse case in track reconstruction (Section 2.3.2), a 2D histogram such as Figure 2.12 is used to create the data points to fit the polynomial. An example of the old calibration and the new calibration fit to data is shown in Figure 2.25. Although the old model was sufficient, the new calibration better matches the data allowing for a more representative simulation. Finally, a Gaussian smearing is applied to the extracted drift-time to give the final 'measured' drift time for hits in MC.

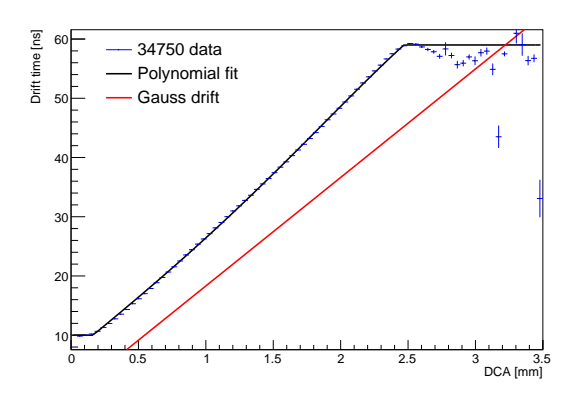


Figure 2.25: The DCA to drift time relation for producing hits in MC showing the updated conversion using a fit to data for layer 47 (blue) compared to the previous linear relationship used for all layers (red).

2.5 Radial magnetic field

As part of the EDM search, mechanisms that could also result in an oscillation in the vertical angle must be considered. A radial component of the magnetic field of the storage ring, henceforth called the radial field, would produce a tilt in the spin precession plane that would be seen as a false EDM-like signal. In this section the mechanism for this is described, and the methods employed to measure the radial field are outlined. This includes a procedure to extrapolate measurements to any given dataset, such that the relevant tilt induced by a radial field can be subtracted from the measured tilt.

2.5.1 Tilt in the spin precession plane

The storage ring has a highly uniform vertical magnetic field, but any radial component that exists will produce a torque on the magnetic dipole moment. This will result in a tilt of the spin precession plane, such that the precession frequency vector remains aligned with the total magnetic field as in Equation 2.2.3.

Given a radial field component $B_x \neq 0$, with $B_r = B_x$ in beam coordinates, there will be some component of ω_a parallel to ω_{η} as given in Equation 2.2.8. This is visualised in Figure 2.26. Assuming a radial field component but no EDM, the anomalous precession frequency may be written as

$$\vec{\omega}_a = -\frac{q}{mc} \begin{bmatrix} acB_x \\ acB_y \\ 0 \end{bmatrix}. \tag{2.5.1}$$

In the same way as an EDM, this tilts the spin precession plane so that

$$\delta_{B_r}^* = \tan^{-1} \frac{\omega_a \cdot \hat{x}}{\omega_a \cdot \hat{y}} = \frac{B_x}{B_y}, \tag{2.5.2}$$

where $\delta_{B_r}^*$ is the rest frame tilt due to a radial field.

The average radial field is measured as $\langle B_r \rangle / B_y$ in ppm following the methods outlined in the next sections, and so is translated to a rest frame

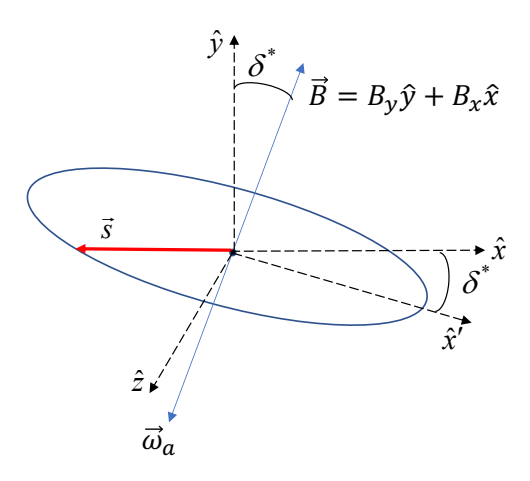


Figure 2.26: Illustration of the tilt in the spin precession plane due to a radial magnetic field.

tilt via

$$\frac{\langle B_r \rangle}{B_y} \text{ ppm} = \delta_{B_r}^* \text{ µrad.}$$
 (2.5.3)

This tilt will cause the vertical decay angle to oscillate just as an EDM would. Hence, the radial field must be measured and the subsequent tilt accounted to complete the measurement of the EDM.

2.5.2 Direct measurement

As part of the commissioning of the storage ring, a measurement of the radial field was taken using a Hall probe at 170 points around the magnet. Then, during the summer shutdown between Run-5 and Run-6, a direct measurement was taken again in the trolley garage - an opening to the storage region where the trolley NMR probe is parked during data taking. This measurement helps to set an uncertainty on the applied radial field from the surface coils, which is needed for the indirect measurement described in Section 2.5.3.

The direct measurement uses a 1D Hall probe fixed on a sliding platform that can be moved horizontally, propped vertically, and the tilt adjusted via three fine threaded screws. The platform also contains two electrolytic tilt sensors allowing the platform to be levelled. For each position the measurement is made and then repeated with the Hall probe rotated 180° to cancel impacts from ohmic offset or the planar Hall effect. The Hall probe is calibrated by measuring the known vertical 1.45 T vertical field.

With this setup, the accuracy of the applied from field from the surface correction coils (SCCs) can be determined. The nominal Run-5 SCC settings are measured, followed by measurements with 4 different induced radial fields. This is compared to the relative shift in radial field as measured by the Hall probe. The results of this can be seen in Figure 2.27, where the straight line fit gives a gradient above the expected value of 1, but within 2.4σ . The uncertainty on the field induced by the SCC is used in the systematics of the measurement described in Section 2.5.4.

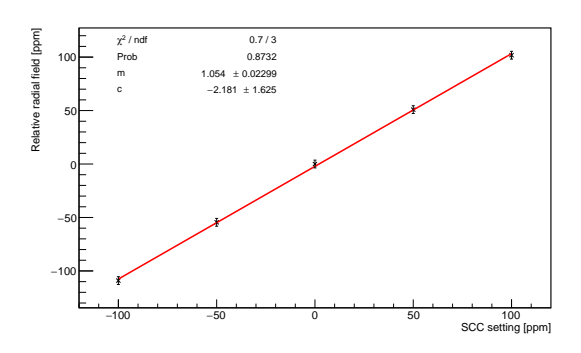


Figure 2.27: The expected radial field from the SCC settings compared to the radial field as measured by the Hall probe. These are both relative to the nominal Run-5 SCC setting. A straight line fit is shown.

2.5.3 Measurement using the ESQs

It is also possible to take an indirect measurement of the radial field using the muon beam, ESQs, and SCCs. The principle underlying this measurement is that the SCCs can be used to apply a known radial magnetic field: if the point of zero total radial field can be determined, the background field must be equal and opposite to the applied field. Furthermore, given a non-zero radial field, the Lorentz force on the muons will have a component in \hat{y} and the restoring force from the ESQs will be equal and opposite to this for some vertical position dependent on the potential difference V. Combining these two ideas, a method to measure the average radial field can be derived.

The average total radial field component $\langle B_r \rangle$ can be described as the sum of the radial field applied by the SCCs $\langle B_r^{app} \rangle$ and any background field $\langle B_r^{bg} \rangle$ such that

$$\langle B_r \rangle = \langle B_r^{app} \rangle + \langle B_r^{bg} \rangle.$$
 (2.5.4)

If the applied field and the point at which $\langle B_r \rangle = 0$ can be found, then the average background radial field can be determined.

By taking the average vertical beam position around the ring $\langle y \rangle$, many effects from closed orbit distortion are cancelled and

$$\langle y \rangle = \frac{R_0}{vB_0} \frac{\langle B_r \rangle}{n} \tag{2.5.5}$$

where R_0 is the magic radius, B_0 is the dominant magnetic field (B_y) , v is the muon velocity, and n, the field index, is given by

$$n = \frac{R_0}{vB_0} \frac{\partial E}{\partial y}.$$
 (2.5.6)

As $n \propto \partial E/\partial y$, the electric quadrupole field gradient, it is also true that $n \propto V$, the voltage potential across the ESQs. Consequently,

$$\langle y \rangle \propto \frac{\langle B_r \rangle}{V},$$
 (2.5.7)

which is the key relationship exploited in this methodology. The proportionality is determined by scanning through applied radial fields and ESQ voltages.

In practice, $\langle y \rangle$ is measured for four quadrupole voltages each at six applied radial field strengths. This measurement is made by taking the vertical crystal hit-position from the calorimeters after cuts are applied to fill-time and energy to isolate stable regions of vertical position. For a given applied field, $\langle y \rangle$ is plotted against the inverse of the four quadrupole voltages and a straight line is fit to these points, thereby extracting gradients that are proportional to the total radial field.

$$\frac{d\langle y\rangle}{du} \propto \langle B_r \rangle = \langle B_r^{app} \rangle + \langle B_r^{bg} \rangle \tag{2.5.8}$$

where u=1/V. To determine the point where the total radial field is zero, these four gradients are considered against the applied field and another straight line fit to determine the zero-crossing. The applied field value for zero-crossing will be equal and opposite to the background radial field.

2.5.4 Extrapolating the radial field

Following the method in [63], the results from an ESQ-based radial field measurement can be extrapolated to give the average radial field for any given dataset. Again, this uses the fact that the average vertical beam position is changed by the average radial field and analyses the same data from the radial field measurement.

Consider that for any point in the run the average radial field is shifted from a reference measurement by $\Delta \langle B_r \rangle$, such that

$$\langle B_r \rangle = \langle B_r \rangle_{\text{REF}} + \Delta \langle B_r \rangle.$$
 (2.5.9)

This difference in radial field is proportional to the change in vertical position. From Equation 2.5.7, it is possible to determine the constant of proportionality between $\langle y \rangle$ and radial field for a given potential

$$\frac{d\langle y\rangle}{d\langle B_r^{app}\rangle} \propto \frac{1}{V}.$$
 (2.5.10)

Combining these gradients for the four voltage settings used allows for a linear fit of the form

$$\frac{d\langle y\rangle}{d\langle B_r^{\text{app}}\rangle} = \frac{m}{V} + c, \qquad (2.5.11)$$

giving the V-dependent conversion between the change in $\langle y \rangle$ and radial field

$$\Delta \langle B_r \rangle = \Delta \langle y \rangle \frac{1}{\frac{m}{V} + c}.$$
 (2.5.12)

Thus, using the change in average vertical position, the average radial field can be determined for any point in the run.

2.5.5 Run-6 measurement and extrapolation

The ESQ-based measurement was completed near the start of Run-6 in December 2022. Firstly, the ESQ pulsing and beam scraping were turned off so that the vertical position was not impacted by these systems. The relevant surface coil settings were then used to apply a known radial field component and the ESQs ramped to the appropriate voltage. For a given combination of settings, data was taken for around 20 minutes to achieve the desired precision.

The average vertical position was then extracted from the calorimeter information, with quality cuts applied to time (30 < t < 300 µs) and cluster energy (1000 < E < 2500 MeV) to isolate a stable beam position. The analysis of the background radial field in Run-6 was completed by F. Rodriguez and determined the background field to be 3.45 \pm 0.23 ppm.

The extrapolation based on the data from the scan is presented here as the author's own work. With the reference average radial field known, the reference vertical position must then be determined. This is done using data from a period of approximately three days either side of the radial field measurement. The results from this are shown in Figure 2.28.

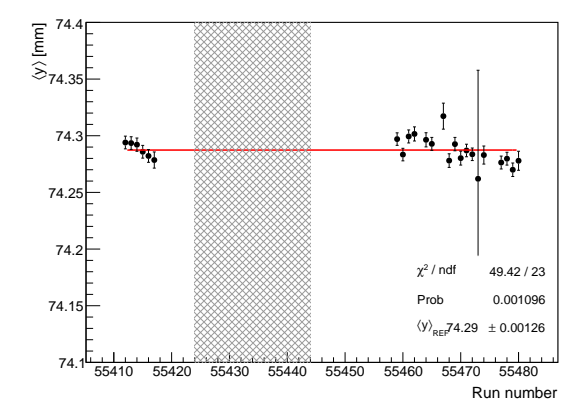


Figure 2.28: The data used to fit the reference vertical position around the time of the ESQ-based radial field measurement in Run-6. The hashed box indicates when the radial field measurement was made.

Using data from the scan and the method described in Section 2.5.4, the average radial field is extrapolated over the whole of Run-6. The gradients $d\langle y \rangle/d\langle B_r^{\rm app} \rangle$ on the left hand side of Equation 2.5.11 are determined for four ESQ voltages shown in Figure 2.29. These gradients are then fit with a straight line as shown in Figure 2.30. As expected, the final fit result is comparable to those found in Run-4 [63] and Run-5 [77] measurements. The offset $c \neq 0$ implies there is some $V < \infty$ at which $d\langle y \rangle/d\langle B_r^{\rm app} \rangle = 0$. However, given the approximations made in this method (such as assuming complete cancellation of beam distortions around the ring when using $\langle y \rangle$), the small $\langle B_r \rangle$ applied relative to B_0 , and limit $V \to \infty$ being non-physical this offset is not a concern.

With this relationship determined, the change in radial field is calculated for all data runs in Run-6 and the total average radial field across Run-6 is presented in Figure 2.31. Statistical uncertainties come only from the statistical uncertainty on $\Delta \langle y \rangle$.

The systematic uncertainties arise from a variety of sources: there is an error associated with the fit used for the conversion to radial field, the relative calorimeter alignment, and the spread in y over a given data range. Around run 57400 the systematic uncertainty increases due to an increase in the alignment uncertainty. This uncertainty addresses

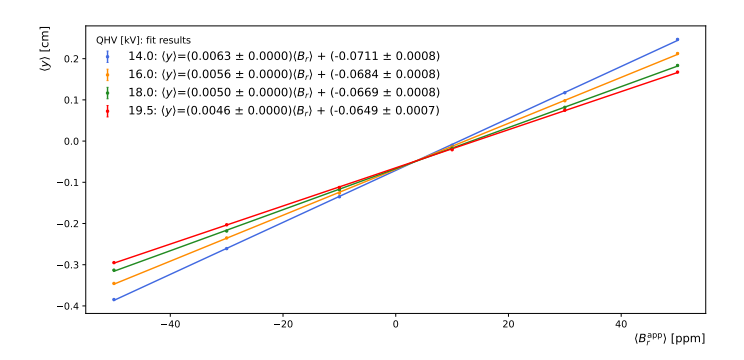


Figure 2.29: The results from the linear fit to the vertical position and applied field for four ESQ voltages.

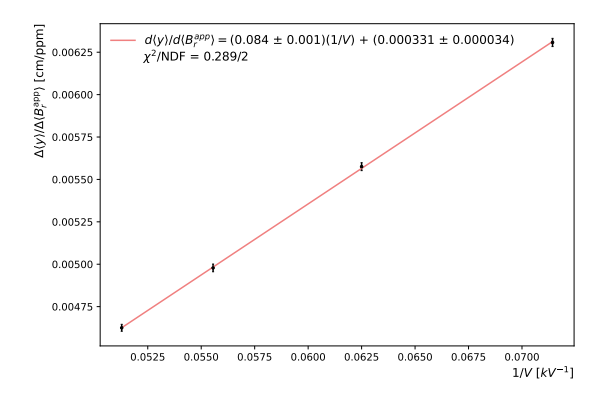


Figure 2.30: The linear fit to the gradients from Figure 2.29 against the inverse of the ESQ voltages.

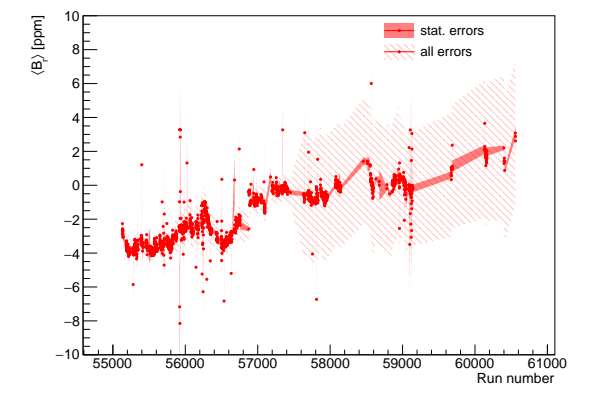


Figure 2.31: The extrapolated average radial field in Run-6 using the Run-6 ESQ-based radial field measurement, showing the statistical and systematic uncertainties determined for each dataset.

the difference in positions of adjacent calorimeters for a given run and compares these to the reference point. Between runs labelled 6G and 6H, this uncertainty increases likely due to the work carried out in the experiment hall in this period.

An ESQ-based radial field measurement was completed in Run-4, 5, and 6, but an extrapolation to Run-2 and Run-3 is required to complete the EDM analysis. Being the nearest measurement in time, the Run-4 reference point in [63] is used to minimise the systematic uncertainties compared to using later scans. The results are presented in Section 3.2.11 with the Run-2/3 EDM analysis.

Chapter 3

Analysis

This chapter details the EDM analysis. To begin, the data used are described including the subsets to be analysed and any adjustments that are applied before the main analysis. Following this, the analysis method and blinding procedure are described in detail. The blinded fit results are then presented. The chapter then moves to the consideration and quantifying of systematic uncertainties, which come from data handling, simulation, and experimental setup. Lastly, some cross-checks are performed before setting out the final blinded EDM result and expected limit.

3.1 EDM analysis

The EDM analysis follows these main steps:

- Dividing the data based on Run, station and momenta.
- Applying randomisations and corrections to account for effects of beam dynamics.
- Adding a blinding signal to the data.
- Fitting the blinded data.
- Evaluating systematics.
- Combining measurements from all datasets.

3.1.1 Data analysed

This analysis uses data from Run-2 and Run-3, with both divided into datasets labelled with a capital letter. Run-2 includes 7 datasets from 2B to 2H and Run-3 is made up of 13 datasets from 3B to 3O excluding 3H, which was removed due to problems with the quadrupoles. Two MIDAS runs that passed the nominal data quality checks are not included due to a time synchronisation issue with the tracker DAQ. These are runs 32455 from 3F, and 34841 from 3O, which represent $\lesssim 0.15\%$ of the data in Run-3. The lettered datasets are combined in the same way as the g-2 analysis: based on beam storage characteristics, electrostatic

quadrupole voltage, and kicker strength [33]. This gives three datasets: Run-2=[2B-2H], Run-3a [3B-3G, 3I-3M], and Run-3b=[3N-3O].

All track vertices passing the extended QCs and with $26.2 \le t \le 602.4$ µs are used for the fitting (equivalent to $6T_a \le t \le 138T_a$ where $T_a = 2\pi/\omega_a$). The start time is chosen avoid most of the flash at the start of the fill, but still maximise the statistics. There are very few muons remaining after ~ 600 µs. After these requirements, the number of track vertices available for analysis totals 8.20062×10^8 from Run-2, 1.09227×10^9 from Run-3a, and 4.31736×10^8 from Run-3b.

3.1.2 Momentum binning

This analysis uses a momentum-binned approach to improve sensitivity to an EDM where the characteristics of the decay are highly momentum dependent. As already discussed, $R_{e^+}(\lambda)$ is a momentum dependent reduction in the observed tilt - a momentum binned analysis allows this to be calculated more accurately. Additionally, the variation of acceptance correction with momentum is motivated and described in Section 2.4.2.

The total momentum range is $750 \le p \le 2750$ MeV, which is chosen to maximise statistics and avoid dramatic changes in acceptance at the edges of the total range. Eight momentum bins are used; each is 250 MeV wide and visualised in Figure 3.1. The momentum range was validated by confirming the acceptance in θ_y is reasonable from Figure 2.22 and the method to calculate $R_{\rm acc}(\lambda)$ is effective in the edge bins. The χ^2 values for fits in these bins are also in line with the central bins as shown in Section 3.1.4.

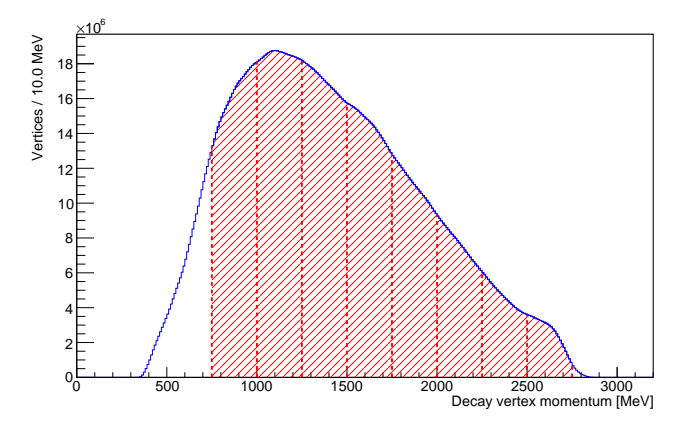


Figure 3.1: Run-2/3 combined positron momentum distribution for analysis vertices with the 8 momentum bins used in the EDM analysis shown by red dashed lines.

3.1.3 Handling of data prior to fitting

Minimising effects of beam dynamics

With the aim of reducing any effects from beam dynamics, the VB motion is randomised out before fitting. This is done with a flat smearing with width equal to the VB period applied to the time. A different random seed is used for each sub-run. Fitting the VB oscillation would also

be a possibility, but the fit is often unstable due to the amplitude of the VB and the choice of bin size. If not accounted for, the VB oscillation produces a peak in the FFTs of the EDM fit residuals as seen in Figure 3.2. The fit quality without randomisation is also reduced [77]. Although the fast rotation frequency is mostly an early time effect and not seen in the FFTs, it should also be randomised out to achieve modest improvements in the fit quality [77]. However, since the cyclotron period (the period of the fast rotation) is less than the period of the VB, no additional randomisation is applied.

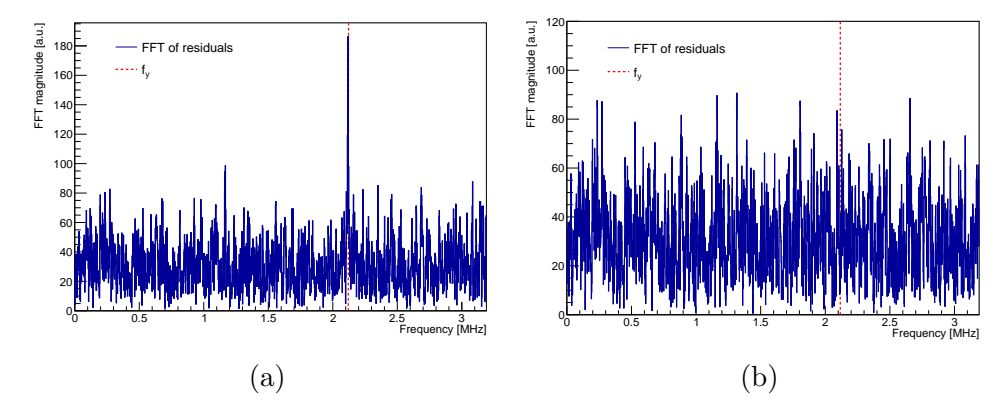


Figure 3.2: FFT of the EDM fit residuals from 3N, stations combined, 750 MeV with (a) before VB randomisation and (b) after VB randomisation is applied.

Alongside this, the decay-time is plotted modulo the ω_a period to maximise sensitivity to any signal with that frequency, as well as minimise effects at any other frequency, such as the CBO. Additionally, the modulo plots are binned as close as possible to the cyclotron period $T_c = 149.1$ ns; with 29 bins per modulo plot, the bin width is $T_a/29 = 150.5$ ns. This further cancels effects from fast rotation and means that frequencies greater than the Nyquist limit $f_c/2$ are also filtered out. The beam and other frequencies are taken from [27] and repeated here in Table 3.1.

Term	Symbol	Frequency (MHz)
g-2	f_a	0.229
Cyclotron	f_c	6.70
Vertical betatron	f_y	2.20
Coherent betatron	$f_{\rm CBO}$	0.372

Table 3.1: Summary of frequencies of relevant oscillations for EDM analysis take from [27]. The frequency's name, its symbol, and frequency value for a field index n=0.108 in the continuous ESQ approximation are outlined. Note that the measured frequencies differ slightly from the continuous ESQ approximation frequencies.

Beam scraping correction

At the start of a fill, the average vertical position of the beam increases quickly with fill-time due to beam scraping, which stabilises around 30 µs

after injection. Relevant to the EDM search, this effect also manifests as the average vertical angle decreasing at early fill-time - if the beam is lower, more upwards going positrons are seen and vice versa. Tracks are used for the EDM fits from $26.2~\mu s$, within the time scale of the scraping, but used in order to maximise the statistics. Accordingly, the drift is characterised and corrected for in each station before the filling the time-modulated vertical angle plots.

The decrease in the average vertical angle is slightly different within each tracker station due to their locations in the ring relative to the injection point, ESQs, and collimators. The drift is fitted separately for each station and momentum bin with a simple exponential

$$\langle \theta_y \rangle (t) = A_{\text{drift}} e^{-t/\tau_{\text{drift}}} + C_{\text{drift}}$$
 (3.1.1)

between 10 μ s and the end EDM fit time of 602.4 μ s. It is corrected for each vertex individually such that

$$\theta_y^{\text{corrected}} = \theta_y - (A_{\text{drift}} e^{-t/\tau_{\text{drift}}} + C_{\text{drift}}),$$
 (3.1.2)

giving, in principle, $\langle \theta_y \rangle = 0$ in each momentum bin. This zeroing of the average vertical angle is also useful as it allows the letter datasets to be combined.

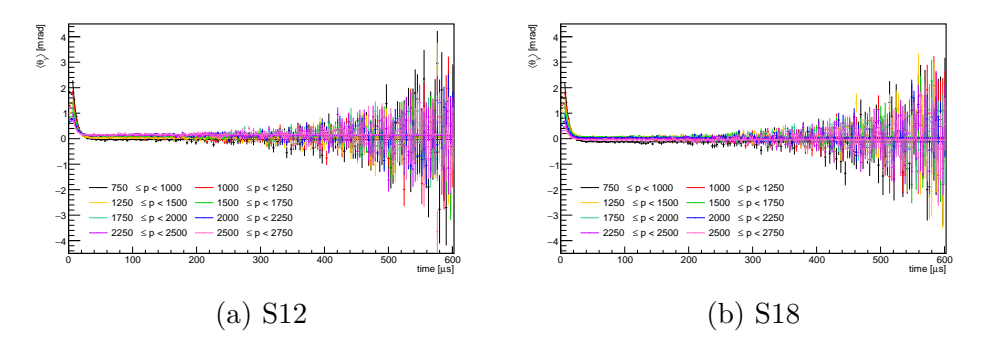


Figure 3.3: Fits to the drift in vertical angle due to beam scraping for dataset 3N and shown for each momentum bin and both stations.

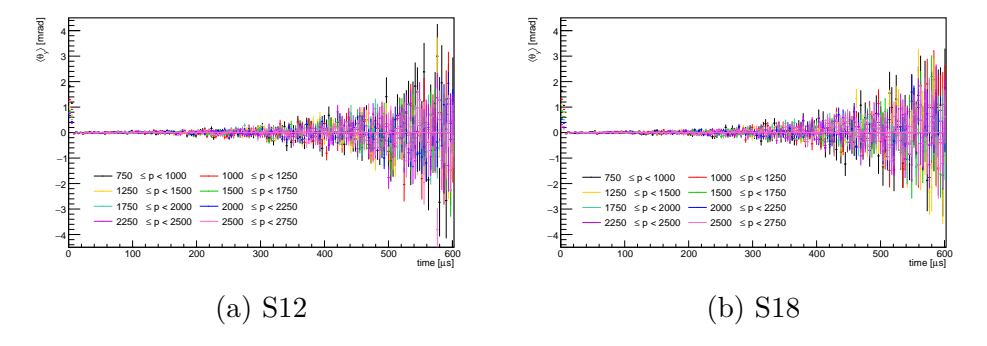


Figure 3.4: The result of applying the beam scraping correction to dataset 3N for both stations and all momentum bins.

An example of these fits is shown in Figure 3.3, where it is apparent the average vertical angle is slightly shifted in each momentum bin and, hence, the correction must be applied separately to each. The results of applying this correction are then shown in Figure 3.4 - the drift at early time is accounted for and the average vertical angle is shifted to zero. A straight line is fit to this confirming $\langle \theta_y \rangle$ is consistent with 0 within errors, and the χ^2 values are satisfactory. These are shown in Appendix A.

3.1.4 Fitting

EDM amplitude fit

As discussed in Section 2.2.2, a non-zero EDM will produce an oscillation in the average vertical decay angle that is $\pi/2$ out of phase with the anomalous precession. To measure this, the average vertical decay angle is fitted with

$$\langle \theta_y \rangle (t) = \frac{A_{g-2} \cos(\omega_a t + \phi_a) + A_{\text{EDM}} \sin(\omega_a t + \phi_a)}{(1 + A_N \cos(\omega_a t + \phi_a^p)) (1 + A_{\text{CBO}} \cos(\omega_{\text{CBO}} t + \phi_{\text{CBO}}))} + C,$$
(3.1.3)

where A_{g-2} accounts for any oscillation in phase with g-2, $A_{\rm EDM}$ is the amplitude of the EDM oscillation $\pi/2$ out of phase with g-2, and C is a constant offset. These three parameters are floated in the fit. The value of ω_a is fixed to the Run-2/3 value to 5 s.f. [33] and $\omega_{\rm CBO}$ to the value extracted from tracker fits in each Run. Parameters ϕ_a , A_N , ϕ_a^p , $A_{\rm CBO}$, and $\phi_{\rm CBO}$ are fixed to the extracted values from the corresponding anomalous precession fit as described in the next sections. The denominator normalises the average angle to the number oscillation in that momentum bin.

Dataset	$\omega_{\rm CBO} \ [{\rm rads}^{-1}]$
Run-2	2.340031
Run-3a	2.328583
Run-3b	2.331814

Table 3.2: Summary of the measured ω_{CBO} in each Run.

The two phases ϕ_a and ϕ_a^p are different: ϕ_a is taken from a p > 1.7 GeV fit and is the 'true' g-2 phase - the phase that the EDM oscillation is referenced to in the numerator. However, the denominator must use the momentum-dependent phase of the g-2 oscillation ϕ_a^p such that the number normalisation is correct. This phase changes with momentum due to positrons that decayed concurrently arriving at the detector at different times.

Figure 3.5 shows the fitted EDM phase using MC decays, where the EDM oscillation is fitted allowing ϕ_a to float. There is no momentum dependence like that seen in the g-2 phase, which discussed more in Section 3.1.4, but there are some statistical variations are on the order of 0.02 rad. As A_{g-2} is specifically allowing for an oscillation orthogonal to $A_{\rm EDM}$, it is also referenced to the true phase.

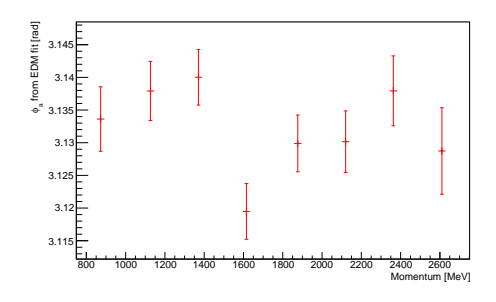


Figure 3.5: The phase from EDM fits to MC decays, where the phase, ϕ_a , is allowed to float in the numerator of Equation 3.1.3.

Anomalous precession frequency fit

To determine the phase of the anomalous precession ϕ_a used in the numerator of the EDM fit, the number of extended QC tracks with p>1.7 GeV is plotted against time, modulo the g-2 period. A nine-parameter fit function is used, but the exponential decay of the CBO amplitude $e^{-t/\tau_{\rm CBO}}$ is set to 1. This approximation is valid in the case of the modulated plots and allows for better fit stability. The resulting 8-parameter fit function is

$$N(t) = N_0 e^{-t/\gamma \tau} (1 + A_N \cos(\omega_a t + \phi_a)) (1 + A_{CBO} \cos(\omega_{CBO} t + \phi_{CBO}),$$
(3.1.4)

where N_0 is the normalisation, t is time since fill, $\gamma \tau$ is the boosted muon lifetime, A_N is the amplitude, ω_a is the anomalous precession frequency and ϕ_a is the phase to be determined. $A_{\rm CBO}$, $\omega_{\rm CBO}$, and $\phi_{\rm CBO}$ are the amplitude, frequency, and phase of the CBO, respectively. As above, the value of ω_a is fixed to the measured frequency in the primary Run-2/3 g-2 analysis [33] and $\omega_{\rm CBO}$ is fixed to the value measured using the trackers. The remaining six parameters are allowed to float.

Fit results for stations 12 and 18 in all three datasets are shown in Figures 3.6 and 3.7. The χ^2 values and probabilities are determined to be satisfactory, especially given that only first order beam dynamics corrections are included.

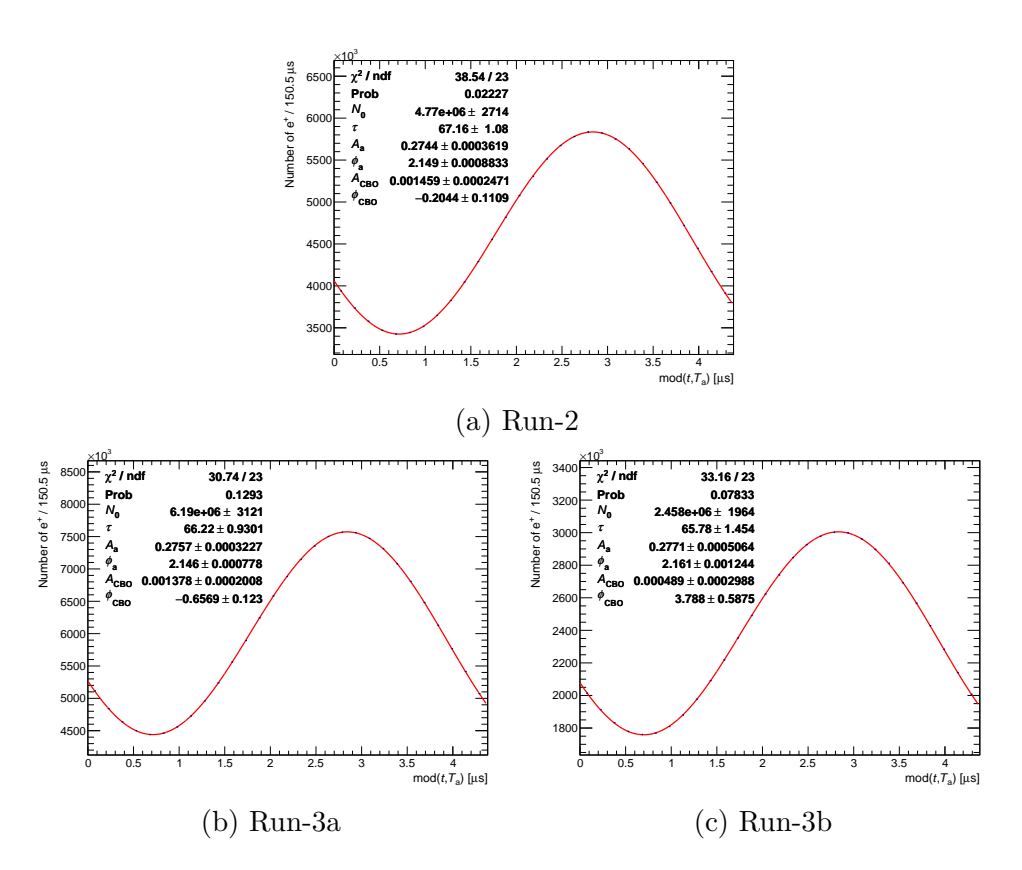


Figure 3.6: Fit to the anomalous precession frequency for quality track vertices with p > 1.7 GeV for station 12.

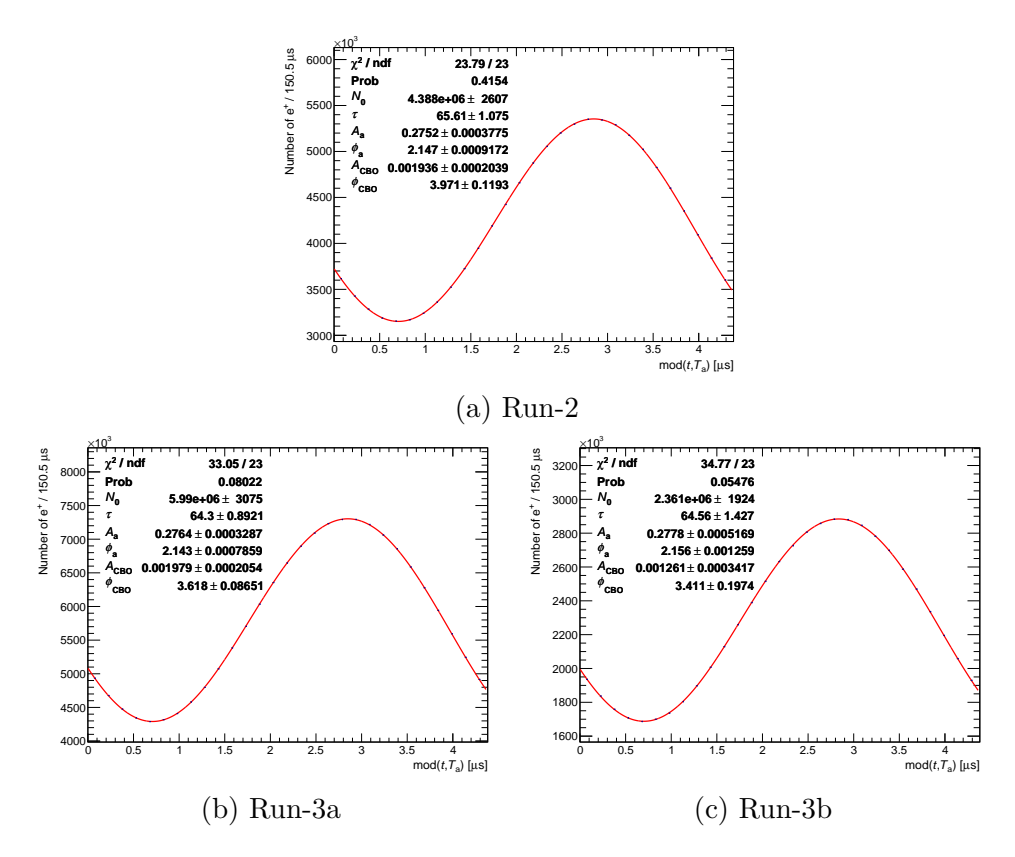


Figure 3.7: Fit to the anomalous precession frequency for quality track vertices with p > 1.7 GeV for station 18.

Momentum-dependent anomalous precession frequency fit

Once the reference phase ϕ_a has been extracted for p > 1.7 GeV, the momentum-dependent terms in the denominator of Equation 3.1.3 must be determined $(A_N, \phi_a^p, A_{\text{CBO}})$ and ϕ_{CBO} . To do this, the 8-parameter fit to the anomalous precession (Equation 3.1.4) is repeated for tracks in each momentum bin following the same method.

The momentum-dependent anomalous precession fits are shown in Figures 3.8 – 3.13. In these fits, ω_a and ω_{CBO} are fixed, and the momentum-dependent phase is forced to lie within the range $\phi_a^p \in [0, 2\pi]$. Summaries of the parameters across momentum bins are shown in Figures 3.14 – 3.17. $\chi^2/\text{NDF} \approx 1$ for all datasets, which is shown in Figure 3.18.

Generally, the parameters are expected to be similar across datasets, but not identical, due to the different beam conditions. The asymmetry in Figure 3.14 is larger at the highest positron momentum and decreases until around 1300 MeV, where positrons are emitted isotropically, before increasing again below this momentum. The phase (Figure 3.15) is seen to shift by $\sim 2\pi$ at this threshold as expected. It should be noted that both theses figures have their uncertainties inflated by a factor of 10 to make the data more visible.

In Figure 3.16 the CBO amplitude is expected to be similar between the stations as seen. However, the CBO phase in Figure 3.17 should be shifted by $\pi/2$ given the locations of the tracker stations relative to each other in the ring. This seen as $3\pi/2$ in the plots, equivalent to flipping the amplitude. In Run-3b the kicker was upgraded moving the beam closer to the central orbit and decreasing the CBO amplitude. This can make it harder to fit the CBO oscillation and, coupled with the modulo plots and it being the smallest dataset, motivates the fluctuations seen in Figure 3.17c.

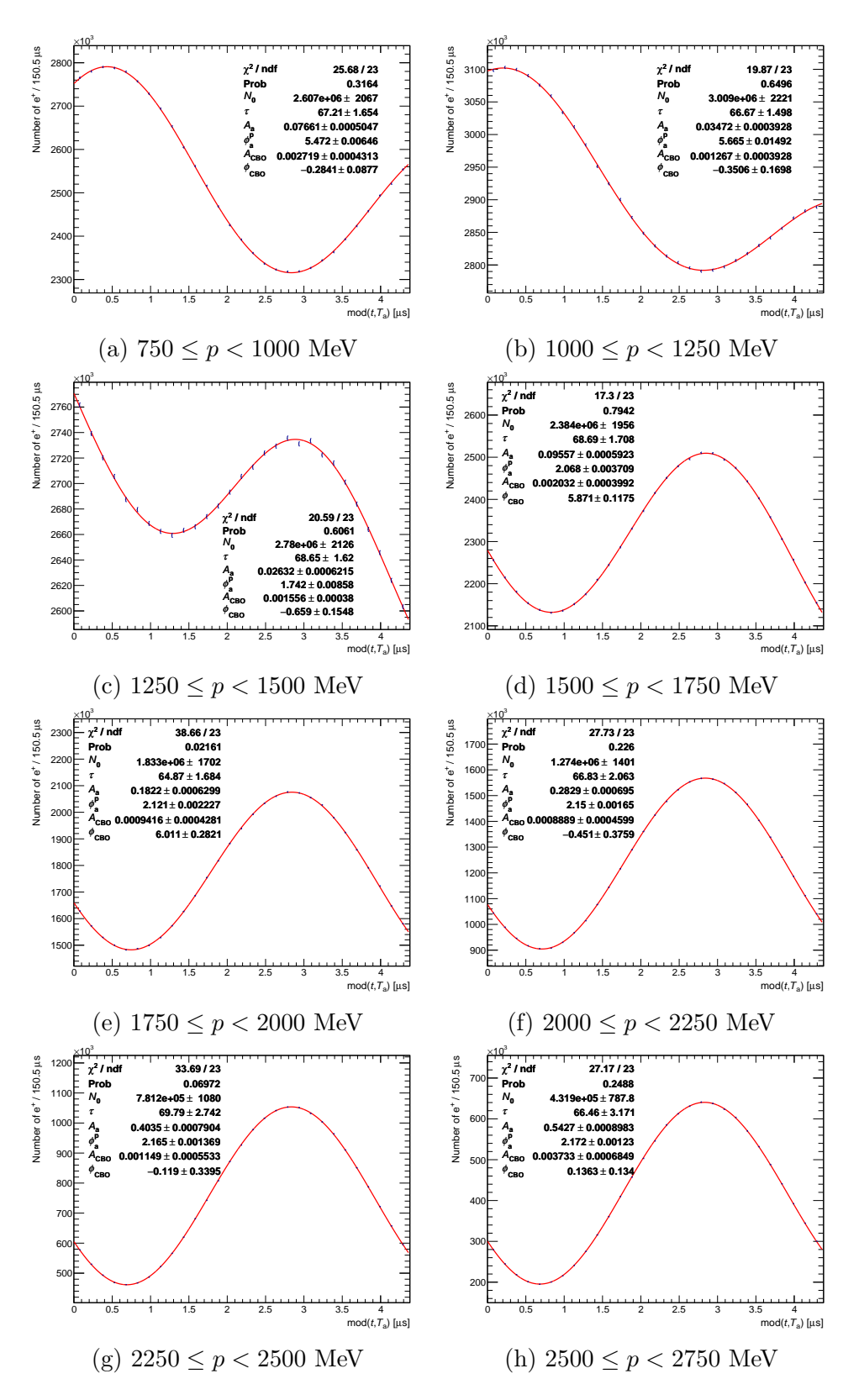


Figure 3.8: Fit to the anomalous precession frequency in momentum bins for Run-2 station 12.

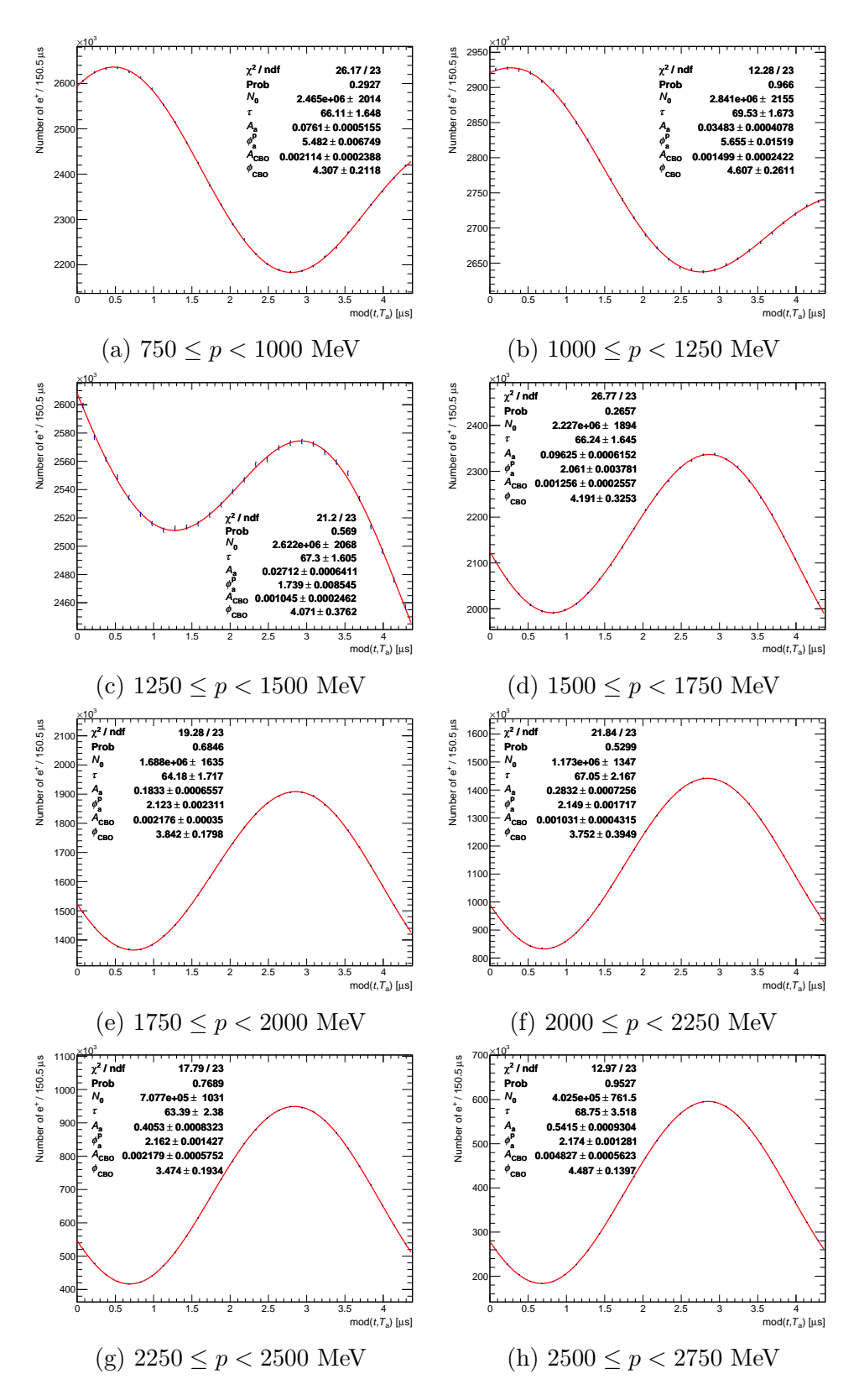


Figure 3.9: Fit to the anomalous precession frequency in momentum bins for Run-2 station 18.

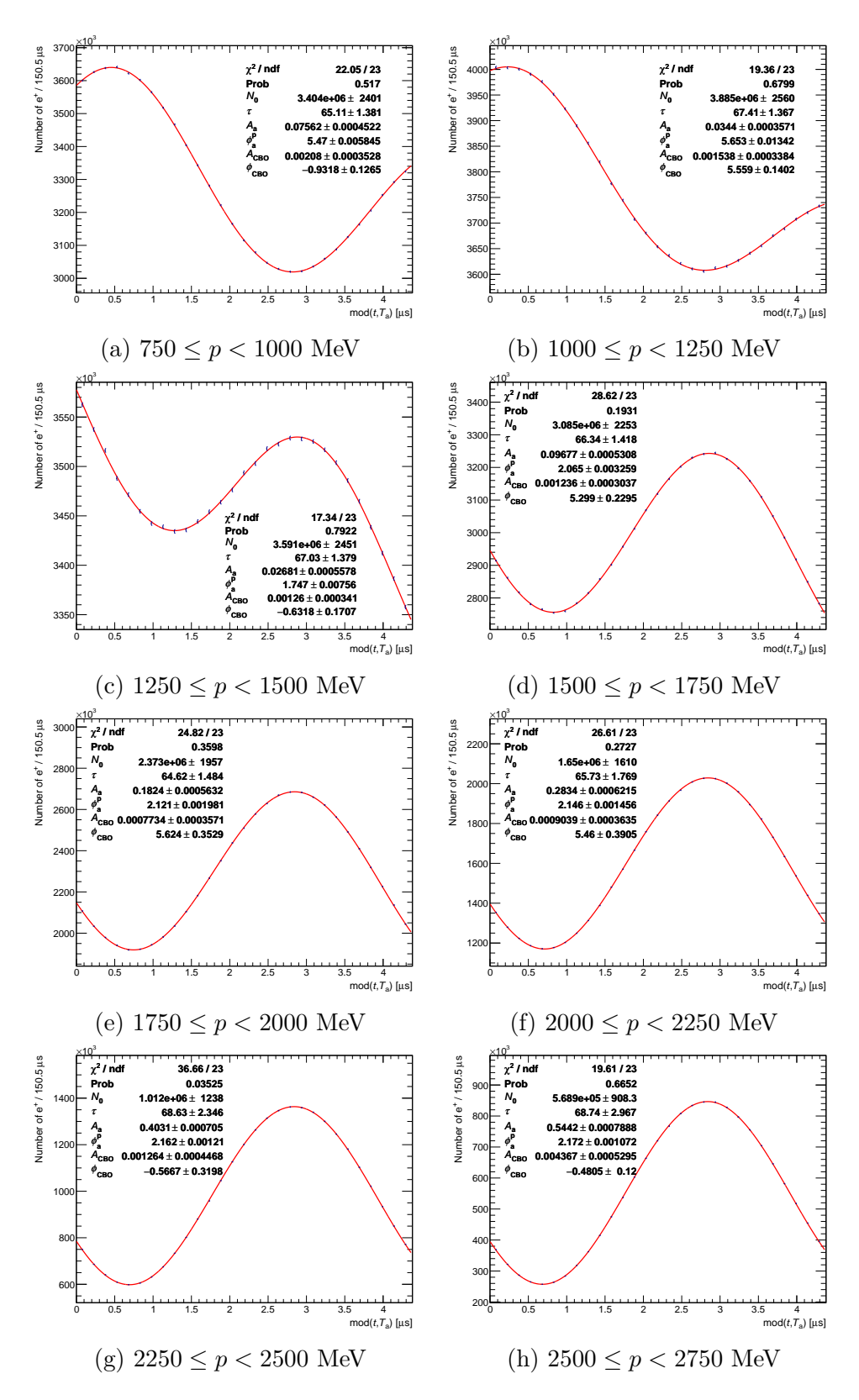


Figure 3.10: Fit to the anomalous precession frequency in momentum bins for Run-3a station 12.

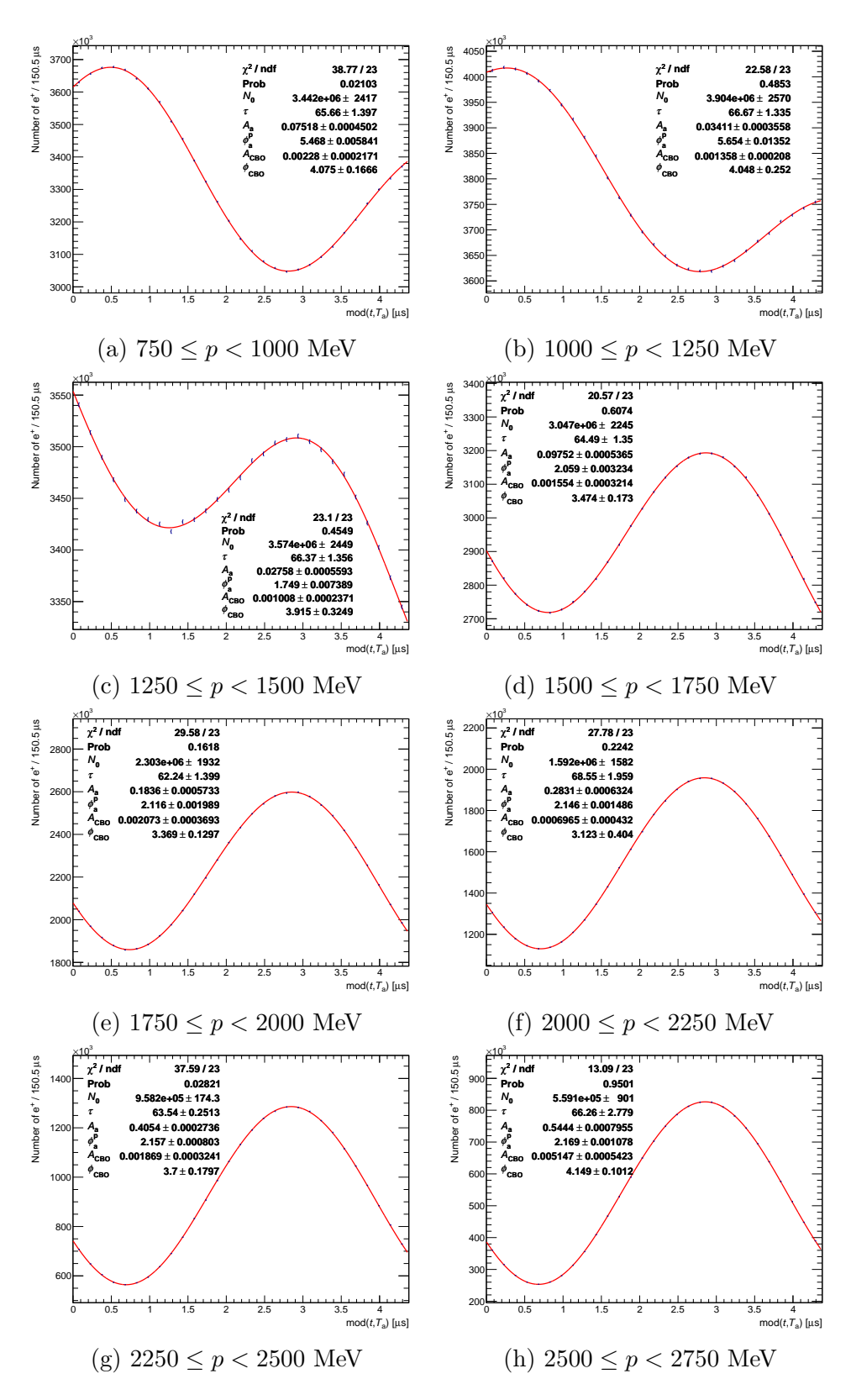


Figure 3.11: Fit to the anomalous precession frequency in momentum bins for Run-3a station 18.

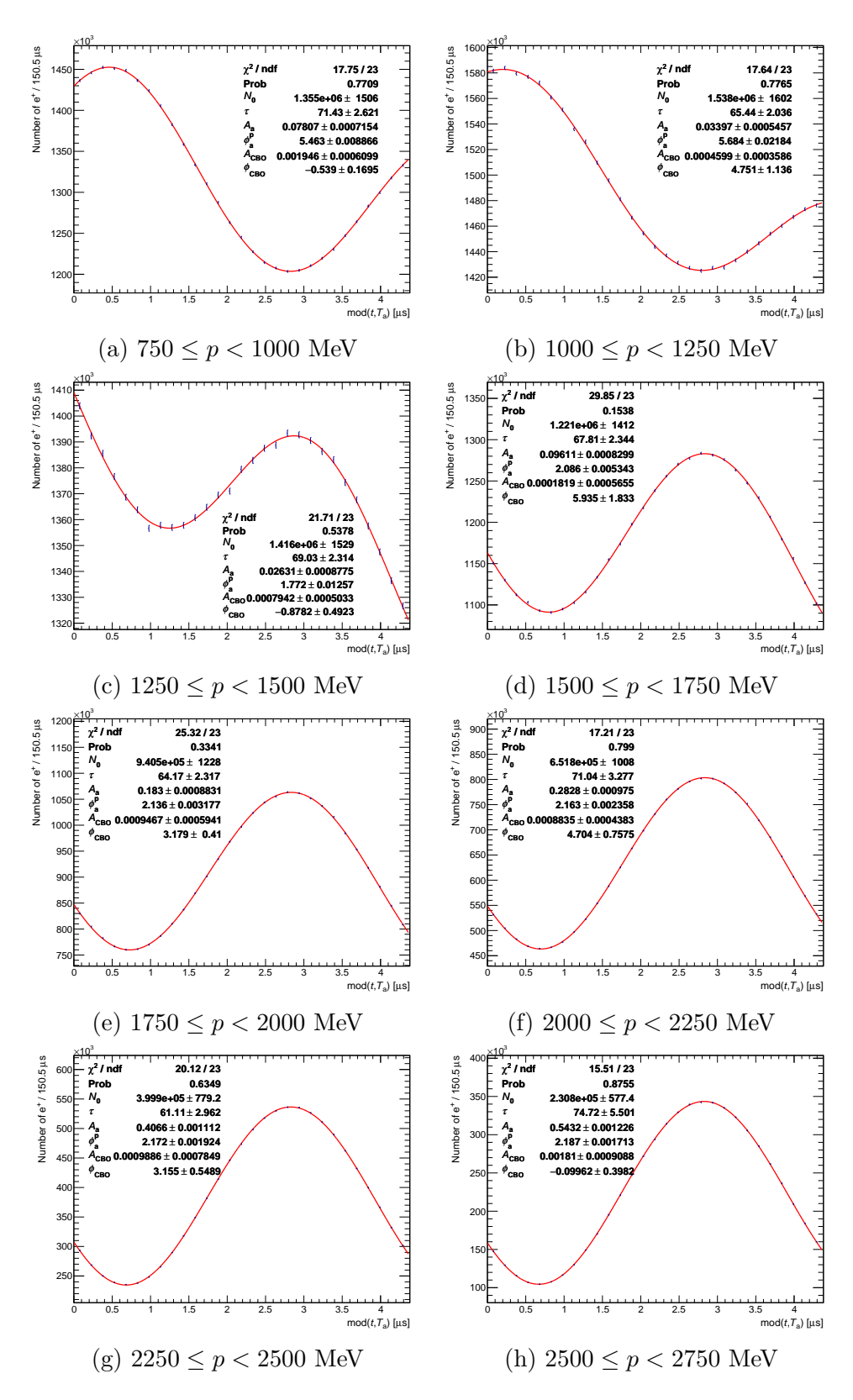


Figure 3.12: Fit to the anomalous precession frequency in momentum bins for Run-3b station 12.

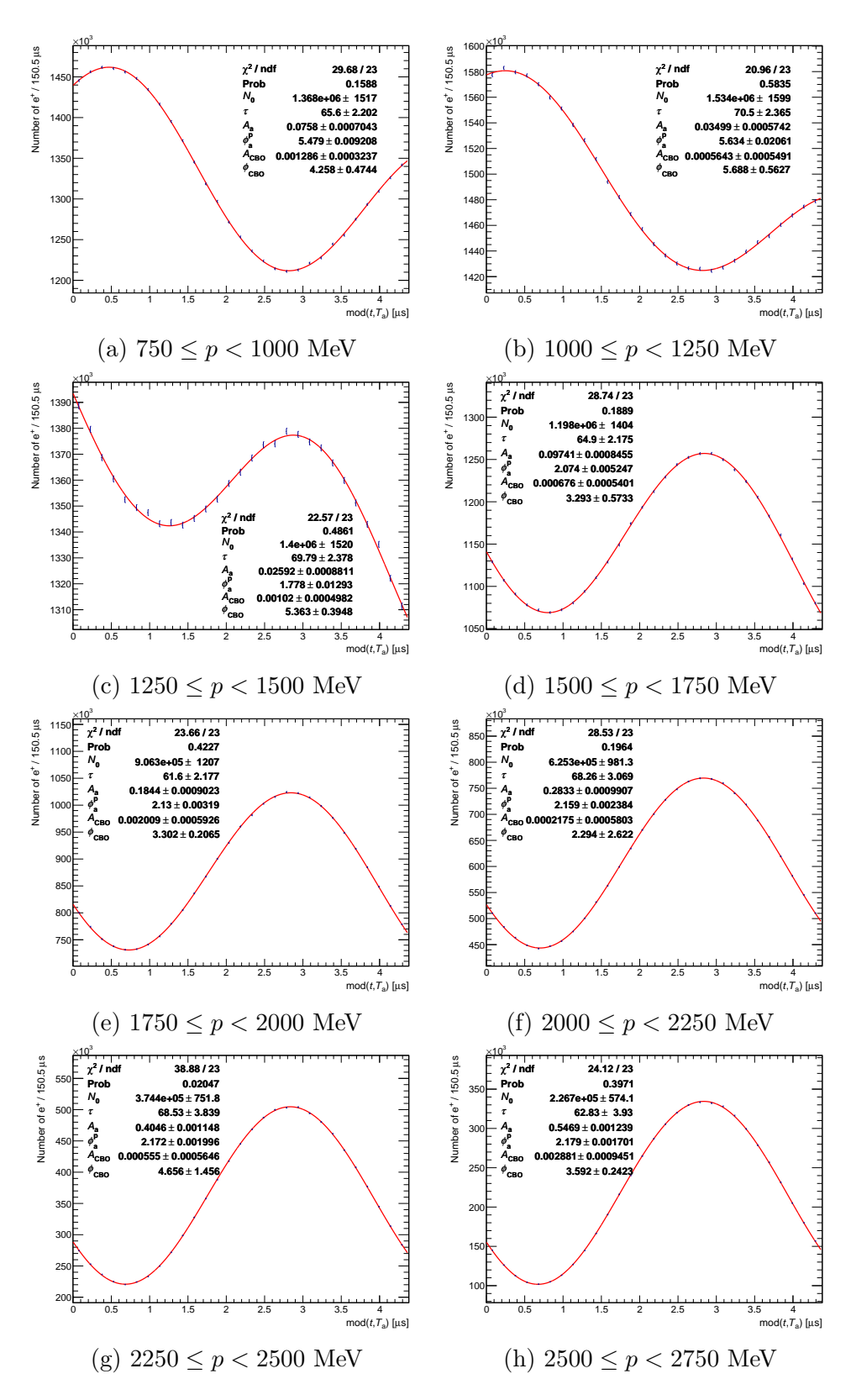


Figure 3.13: Fit to the anomalous precession frequency in momentum bins for Run-3b station 18.

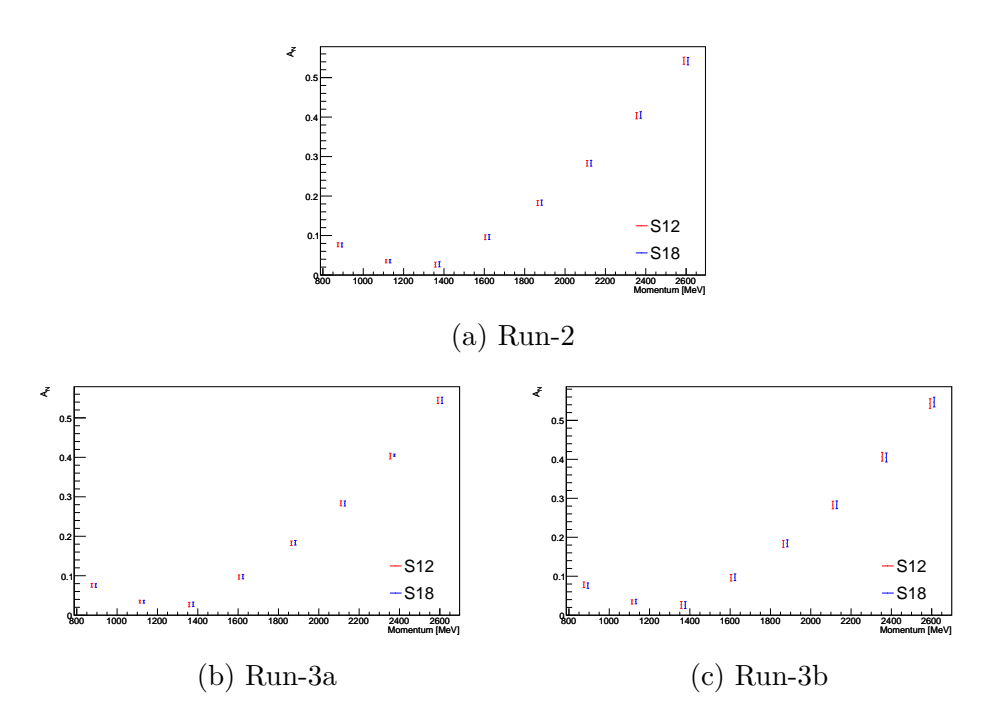


Figure 3.14: Summary of the amplitude from the anomalous precession frequency fits in each momentum bin for all datasets and both stations. The uncertainties on all point have been multiplied by 10 to improve readability.

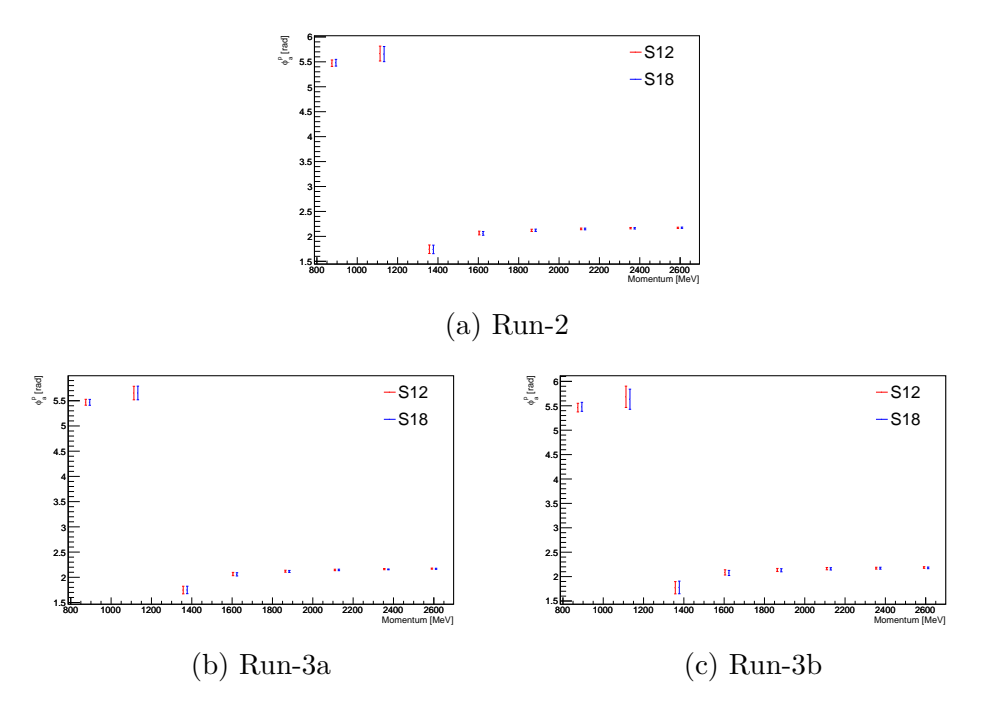


Figure 3.15: Summary of the phase from the anomalous precession frequency fits in each momentum bin for all datasets and both stations. The uncertainties on all point have been multiplied by 10 to improve readability.

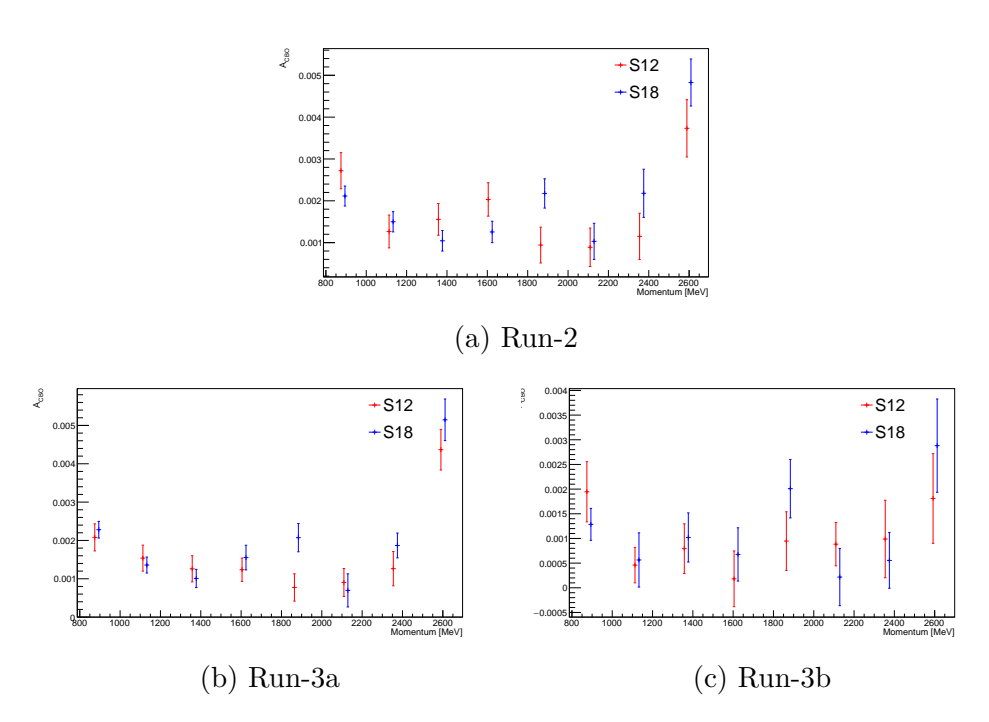


Figure 3.16: Summary of the CBO amplitude from the anomalous precession frequency fits in each momentum bin for all datasets and both stations.

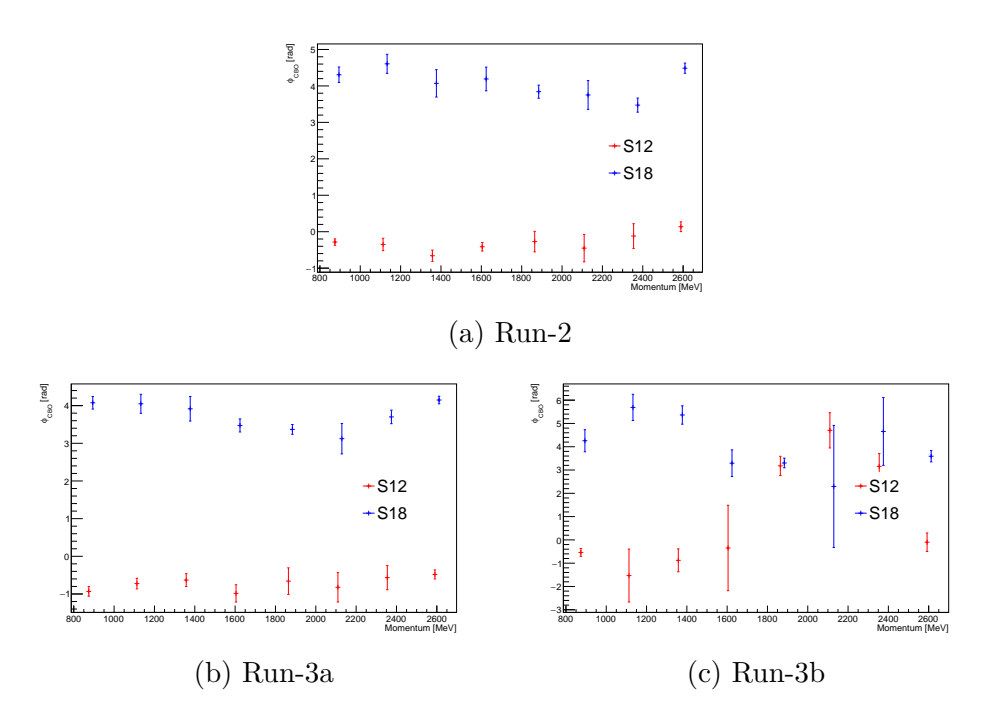


Figure 3.17: Summary of the CBO phase from the anomalous precession frequency fits in each momentum bin for all datasets and both stations.

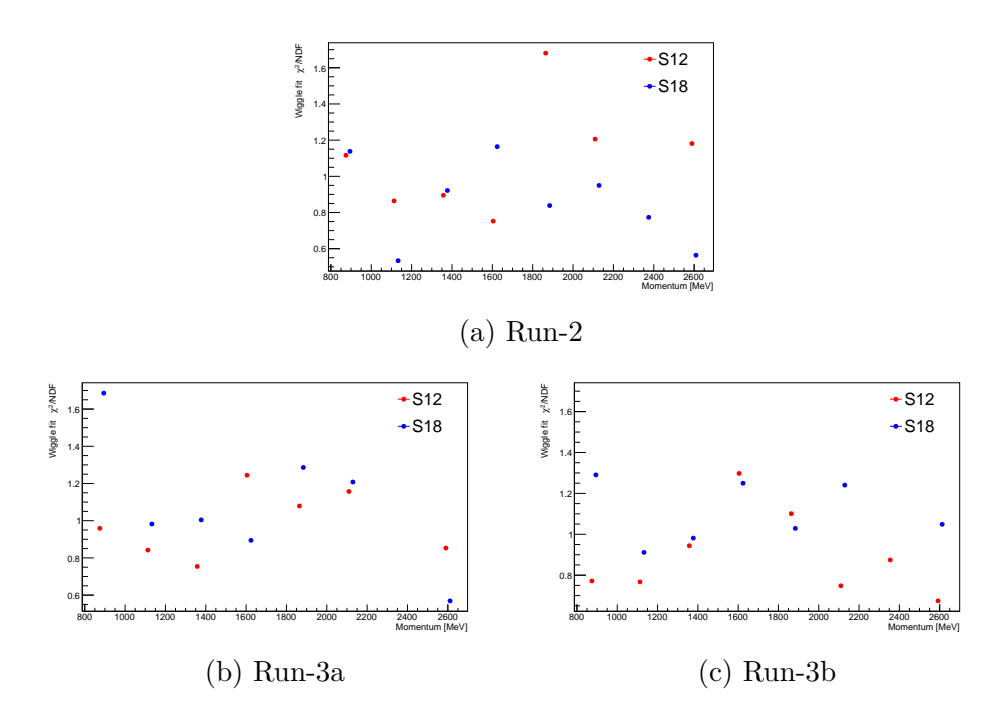


Figure 3.18: Summary of the reduced χ^2 from the anomalous precession frequency fits in each momentum bin for all datasets and both stations.

3.1.5 Blinding

To prevent the introduction of any biases during the analysis, the data are blinded such that the true measurement result is unknown until the methodology has been satisfactorily tested and completed. The blinding is achieved by adding a false signal amplitude in phase with an EDM oscillation on top of the data. This is applied using the same blinding software employed in the ω_a analyses. The results from Run-2, Run-3a, and Run-3b presented here all use same blinding¹.

A blinding string, whose hash seeds a random number generator, is used to sample from a distribution comparable to that in Figure 3.19 which was produced using 100,000 blinding strings. This number is then used as a multiplier on the BNL muon EDM limit to give the size of the blinding EDM. Assuming any possible measurement is at most the BNL direct limit, the blinding must be constructed to be greater than this.

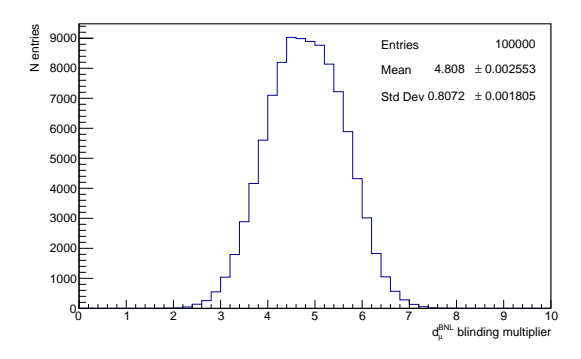


Figure 3.19: The distribution of blinding multipliers from 100,000 unique blinding strings. Adapted from [63].

The blinding EDM value is converted to a tilt via Equation 2.2.27 and the four factors for Lorentz transform R_{γ} , polarisation R_{P} , maximum vertical angle reduction $R_{e^{+}}(\lambda)$, and acceptance $R_{acc}(\lambda)$ are applied to take this tilt to what would be the observed amplitude in each momentum bin

$$A_{\text{EDM}}^{\text{Blind}} = R_{\gamma} R_{P} R_{e^{+}}(\lambda) R_{\text{acc}}(\lambda) \delta^{*,\text{Blind}}.$$
 (3.1.5)

The fitted data then becomes

$$\langle \theta_y \rangle^{\text{Blind}}(t) = \langle \theta_y \rangle(t) + \frac{A_{\text{EDM}}^{\text{Blind}} \sin(\omega_a t + \phi_a)}{(1 + A_N \cos(\omega_a t + \phi_a^p)) (1 + A_{\text{CBO}} \cos(\omega_{\text{CBO}} t + \phi_{\text{CBO}}))},$$
(3.1.6)

where the blinding signal is normalised to the anomalous precession oscillation and uses the fitted phases, amplitude, and CBO parameters in each momentum bin as in the EDM analysis described in Section 3.1.4. In order to extract the final unblinded results, the fits will be repeated on the data without any injected signal.

¹Initially, Run 2 was blinded separately to Run-3a and Run-3b, but after the necessary checks, these were relatively unblinded ahead of a global unblinding.

3.1.6 EDM fit results

Using the parameters ϕ_a , ϕ_a^p , A_N , $A_{\rm CBO}$, and $\phi_{\rm CBO}$ extracted from fits in Section 3.1.4, and fixing ω_a and $\omega_{\rm CBO}$ as described, the blinded average vertical angle is fitted in each momentum bin. The blinded fits are shown for both stations for Run-2 in Figures 3.20 and 3.21, Run-3a in Figures 3.22 and 3.23, and Run-3b in Figures 3.24 and 3.25. Across momentum bins, datasets, and stations, the quality of the fit is acceptable, with $\chi^2/{\rm NDF} \approx 1$ shown in Figure 3.26 and the fit probabilities shown in Figure 3.27.

The EDM amplitudes before any *R*-factors are applied are summarised in Figure 3.28. These are not expected to be the same across momentum due to the lab-frame sensitivity and acceptance effects discussed in Sections 2.2.4 and 2.4.2. Differences between the Runs and stations are also expected due to the changes in beam conditions, which also affect the acceptance.

 A_{g-2} , is summarised in Figure 3.29. As expected after applying the beam scraping correction, the constant offset is consistent with zero. A_{g-2} has a similar momentum-dependent shape in all the datasets. It has been shown that an in-phase oscillation could arise from a bias in the vertical angle acceptance. By using a toy MC with no in-phase oscillation added, a false in-phase amplitude can be produced if an acceptance function is applied with a bias in the vertical angle. This is possibly due to the denominator of the fit function in Equation 3.1.3 introducing an in-phase signal given all the parameters are fixed. Results of this are shown in Figure 3.30. It can also be seen that this bias in θ_y did not produce a false $A_{\rm EDM}$. The phase difference between the numerator and denominator was also exaggerated producing a false $A_{\rm EDM} < 0.1~\mu rad$, which is deemed negligible.

Figure 3.31 shows a summary of the offset C. The constant offset sits slightly above zero, which likely arises due to the beam scraping correction being affected by the VB randomisation. Any randomisation will smear out the data and this, in turn, reduces the values of $A_{\rm drift}$ and $\tau_{\rm drift}$ such that the correction applied is slightly too small. The effect would be the same in all datasets and so is not expected to have an impact, especially as the systematic uncertainties associated with this correction are small (see Section 3.2.2). Going forward, this effect should be accounted for by fitting the beam scraping correction before randomisations. Furthermore, the spread of these offsets is small compared to their uncertainties, but this is likely an artefact of shifting $\langle \theta_y \rangle$ to be (nearly) zero. As the distributions of A_{g-2} and $A_{\rm EDM}$ are more comparable to their errors, we would expect to also see this for C before the correction. The average angle in each momentum bin as fitted in the beam scraping correction can be seen in Figure A.1.

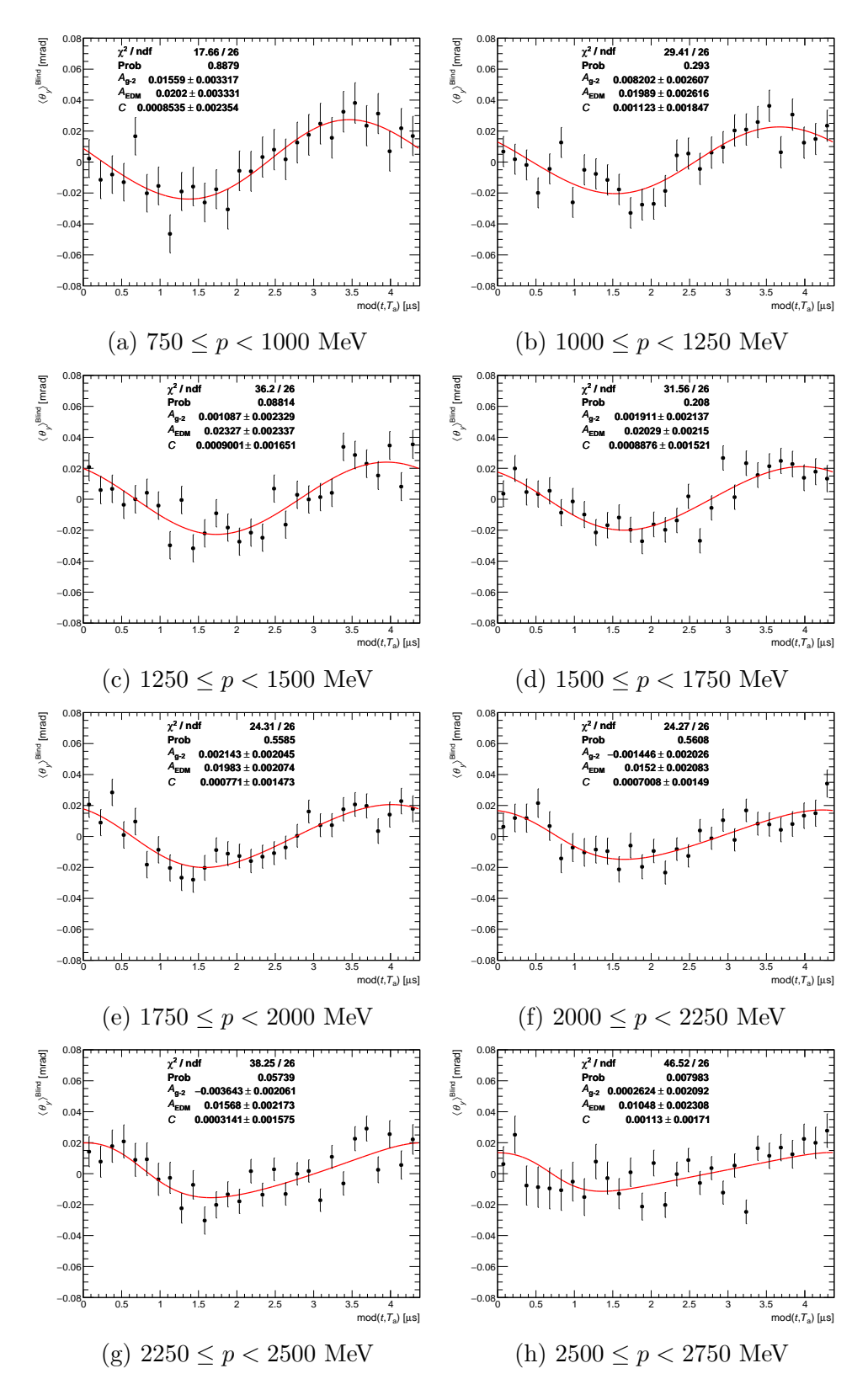


Figure 3.20: Fit to the average vertical angle in momentum bins for Run-2 station 12.

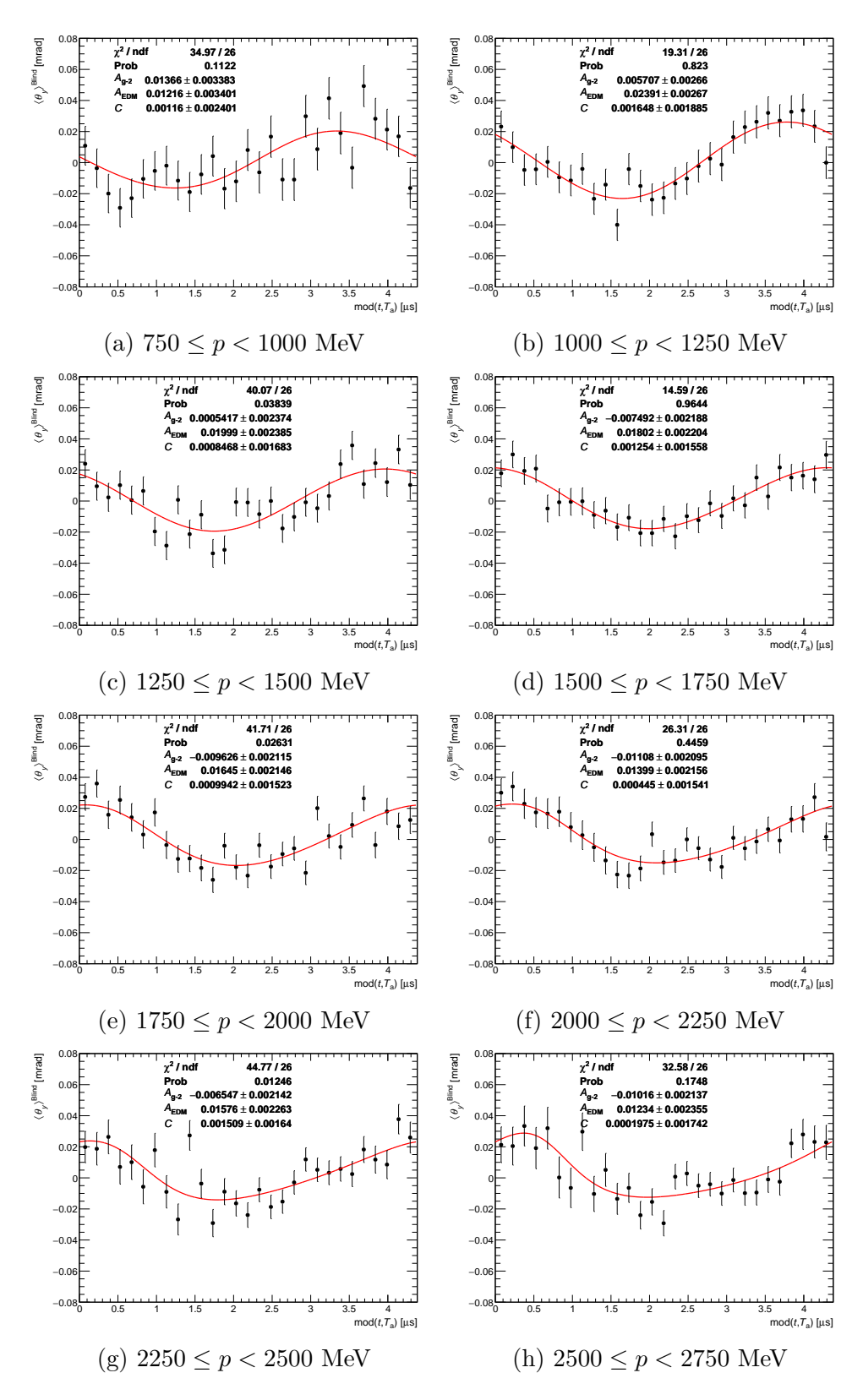


Figure 3.21: Fit to the average vertical angle in momentum bins for Run-2 station 18.

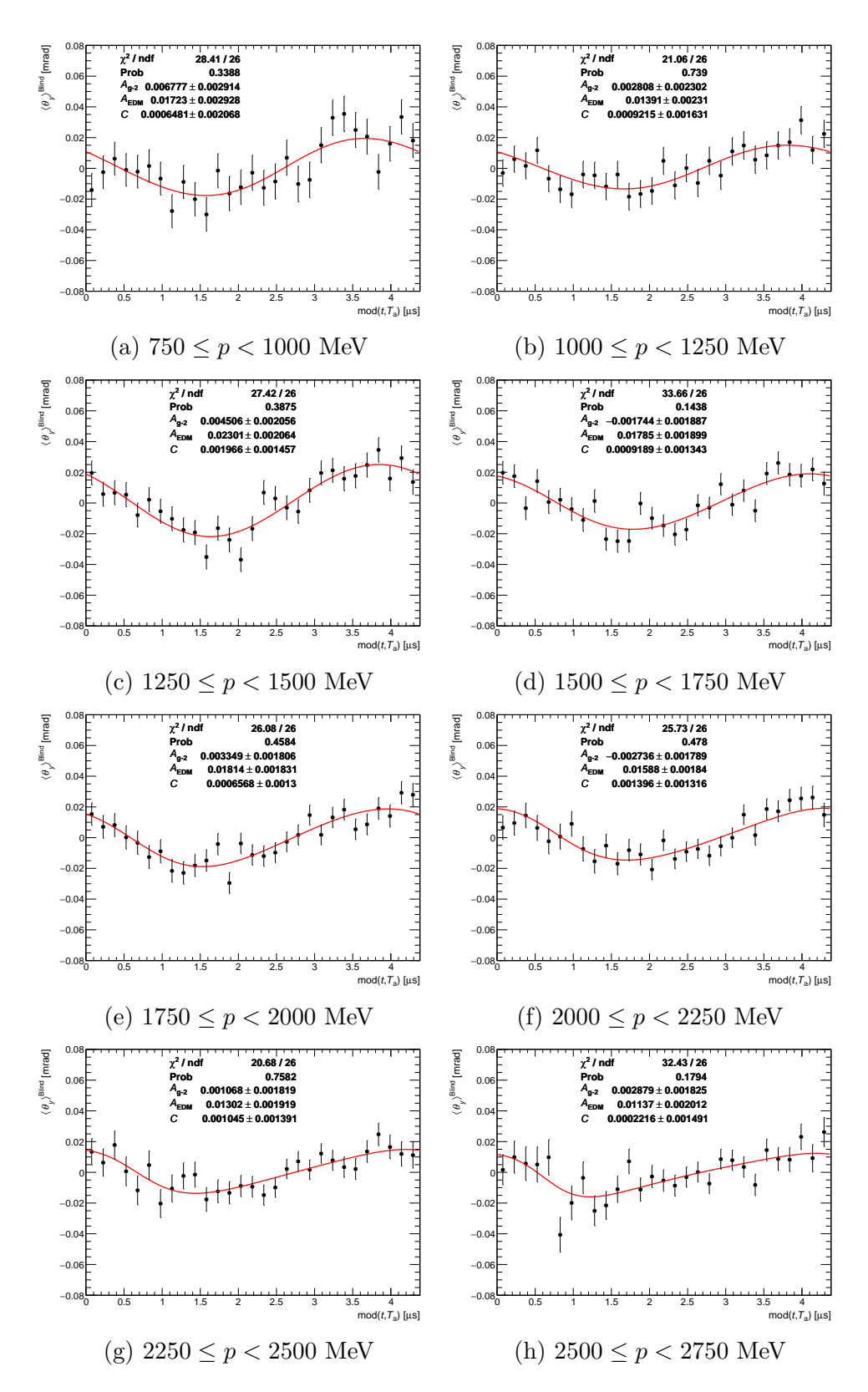


Figure 3.22: Fit to the average vertical angle in momentum bins for Run-3a station 12.

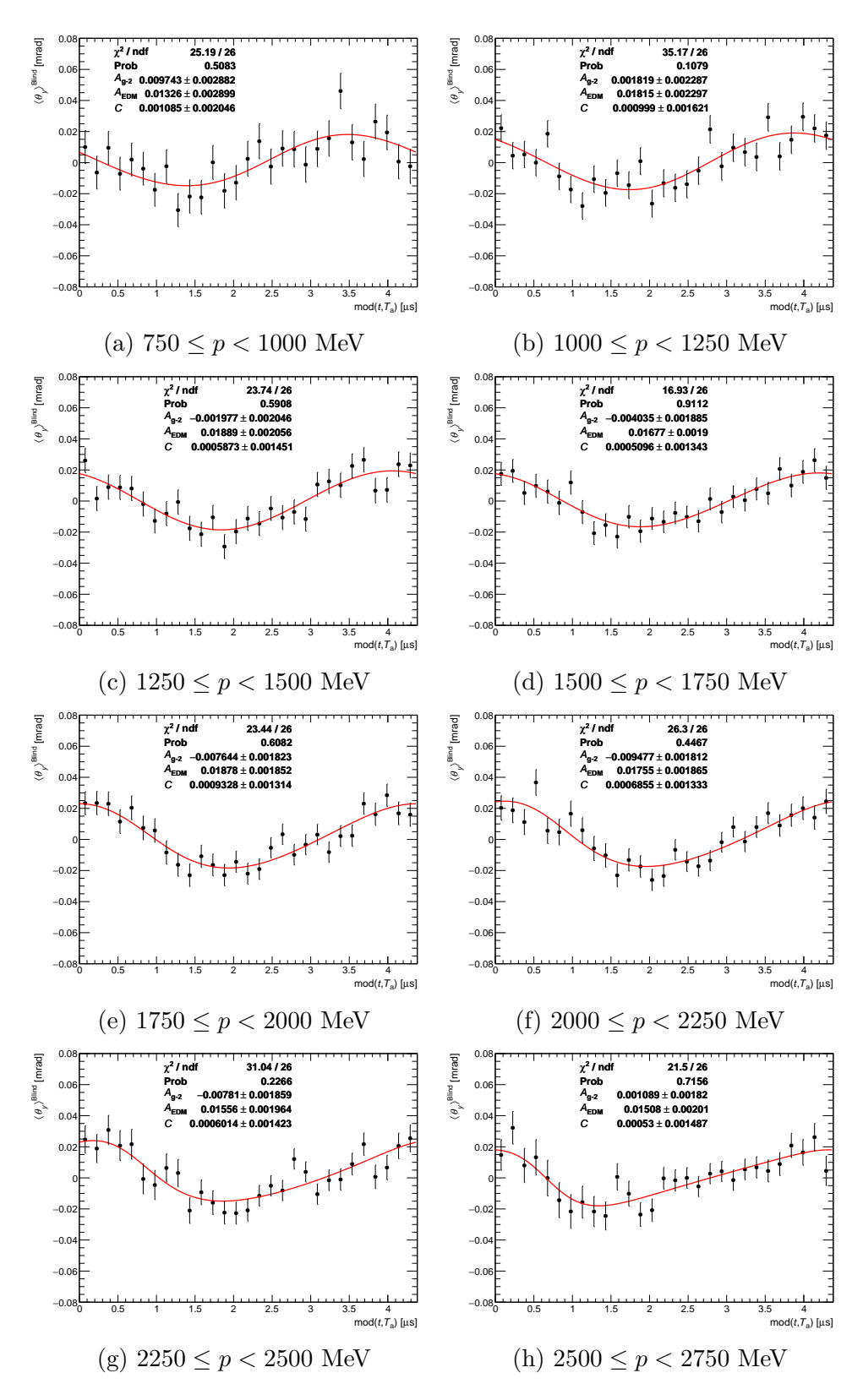


Figure 3.23: Fit to the average vertical angle in momentum bins for Run-3a station 18.

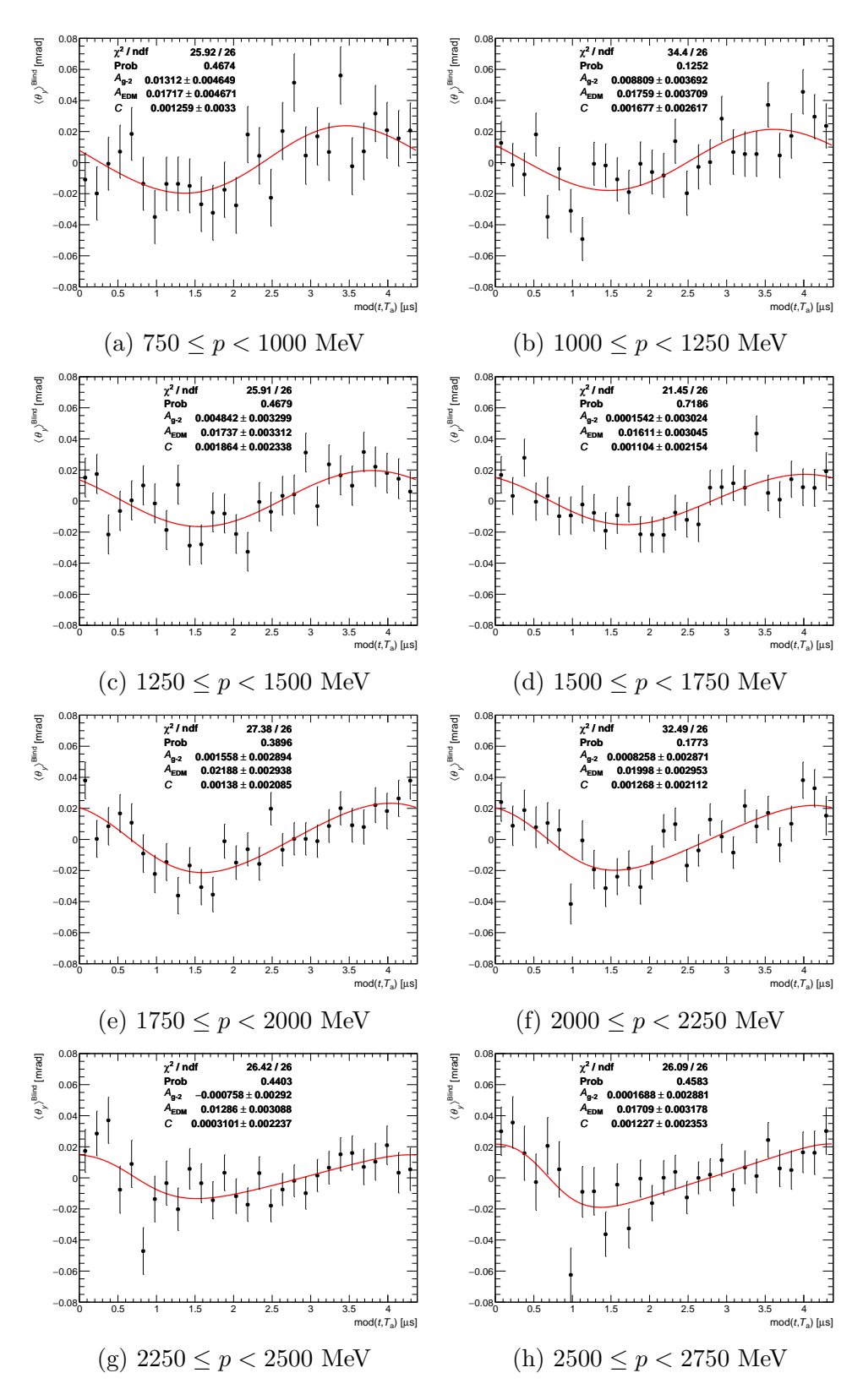


Figure 3.24: Fit to the average vertical angle in momentum bins for Run-3b station 12.

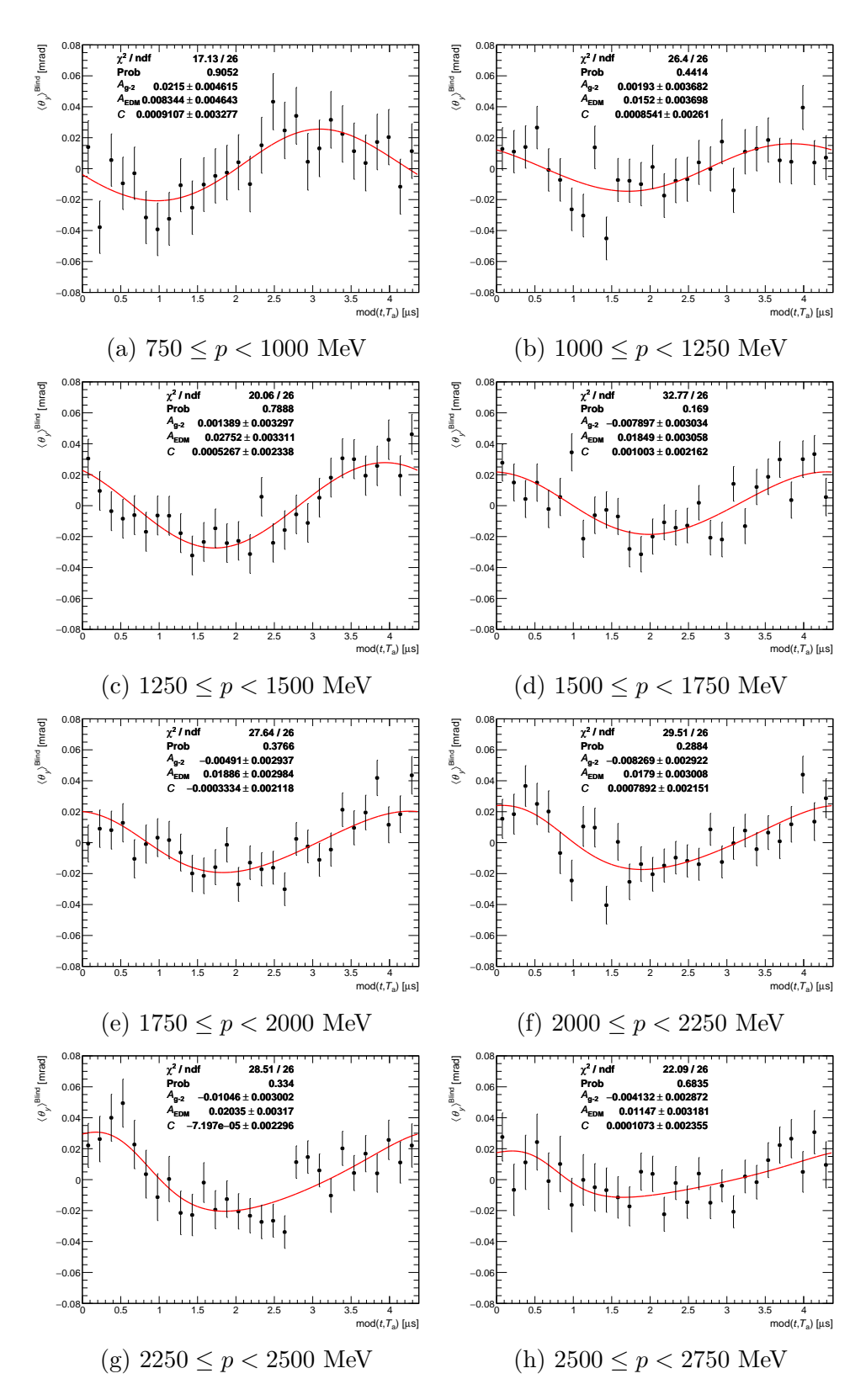


Figure 3.25: Fit to the average vertical angle in momentum bins for Run-3b station 18.

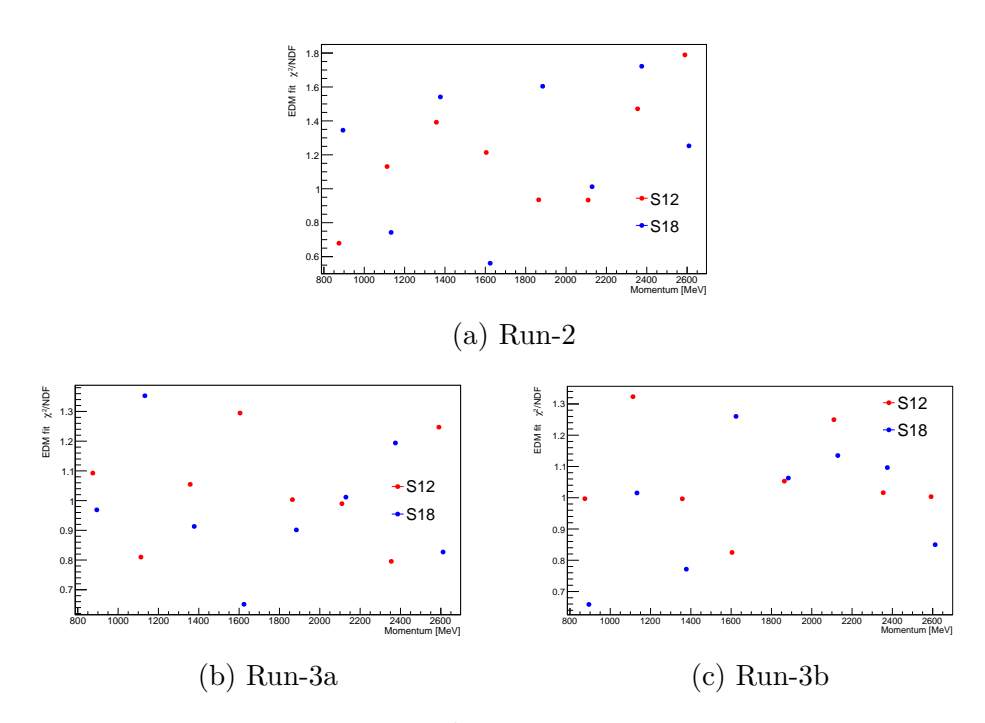


Figure 3.26: Summary of the χ^2/NDF for the average vertical angle fits in each momentum bin for all datasets and both stations.

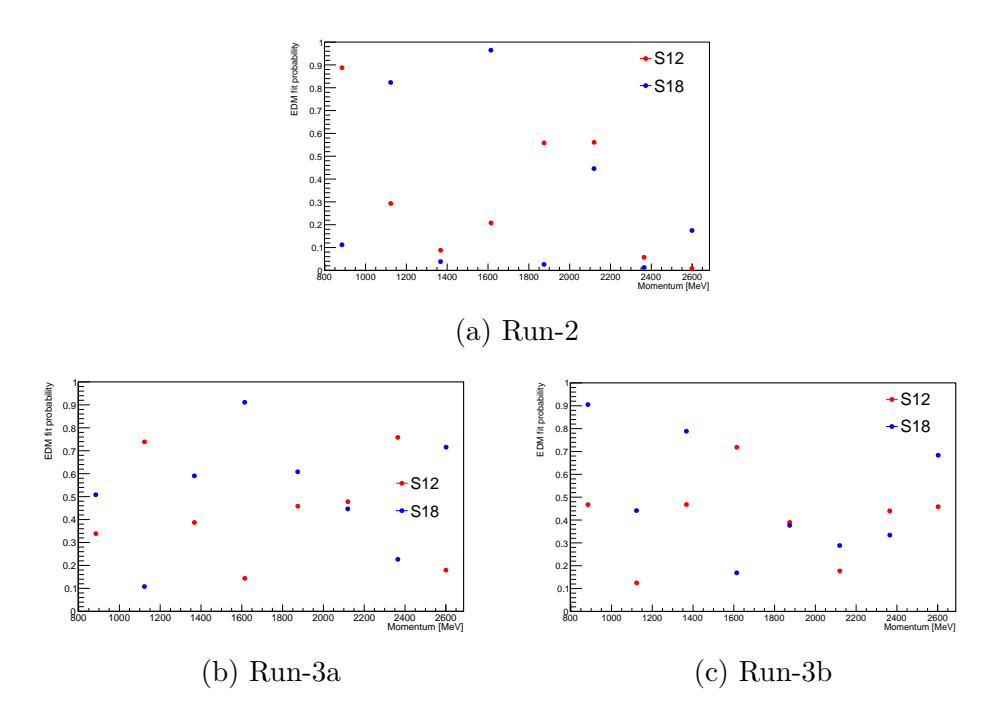


Figure 3.27: Summary of the p values for the average vertical angle fits in each momentum bin for all datasets and both stations.

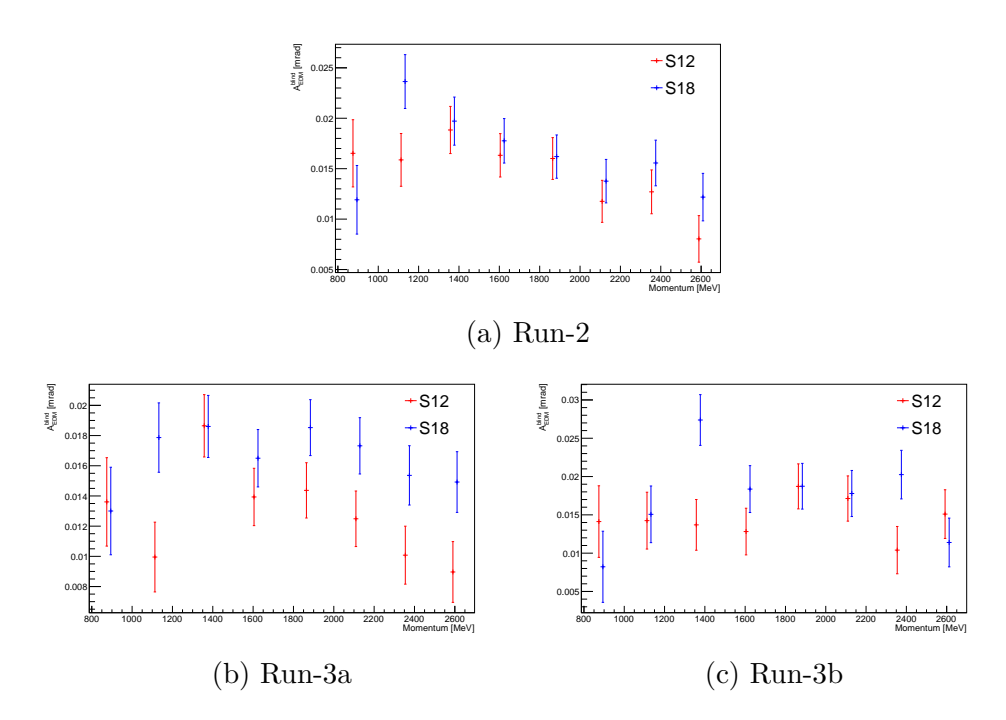


Figure 3.28: Summary of $A_{\rm EDM}$ from the average vertical angle fits before any corrections in each momentum bin for all datasets and both stations.

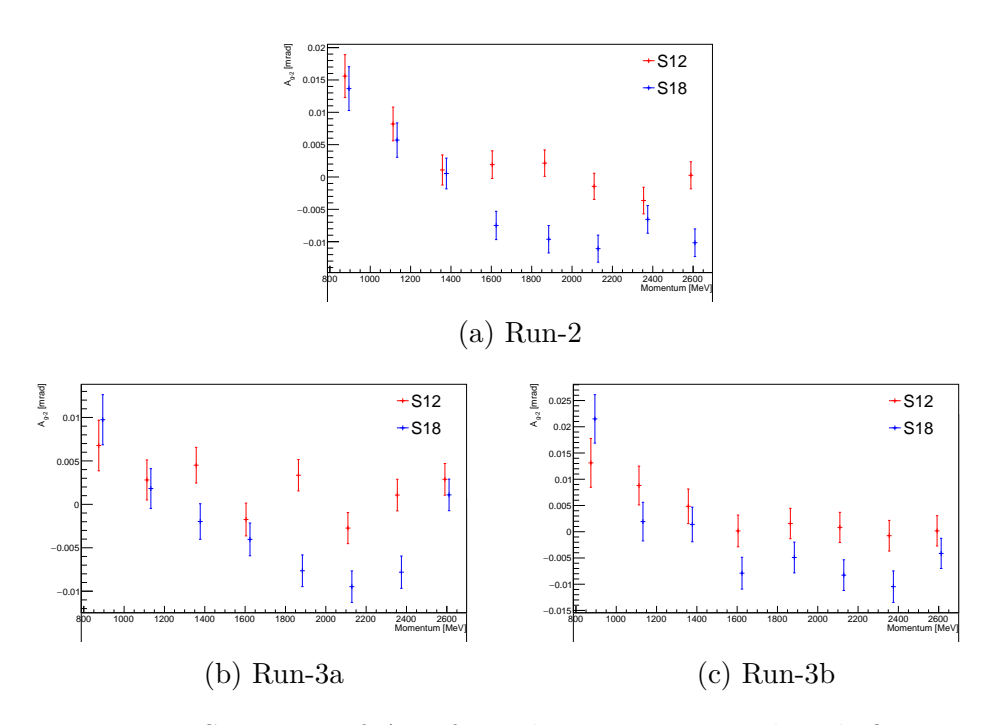


Figure 3.29: Summary of A_{g-2} from the average vertical angle fits in each momentum bin for all datasets and both stations.

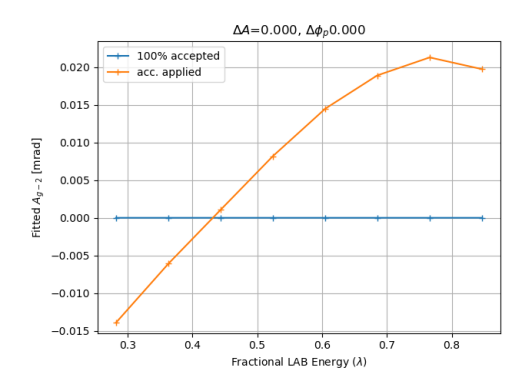


Figure 3.30: The fitted A_{g-2} from a toy MC study before and after applying an acceptance function with a bias of +1 mrad. The acceptance introduces a false amplitude in the fit in phase with g-2.

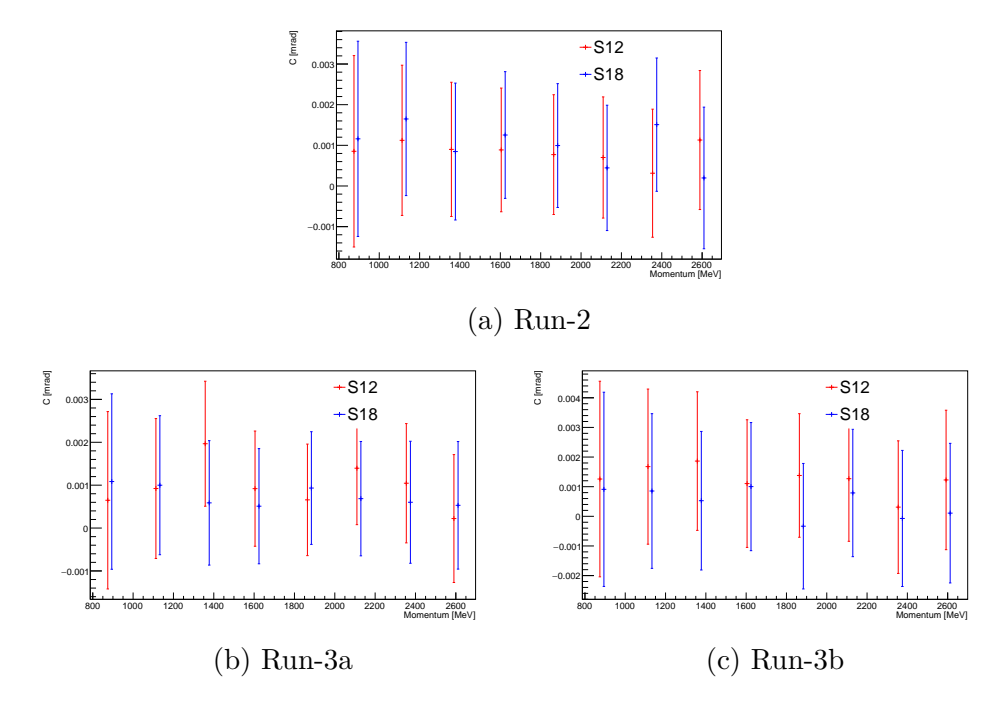


Figure 3.31: Summary of offset C from the average vertical angle fits in each momentum bin for all datasets and both stations.

3.2 Systematic uncertainties

There are several systematic uncertainties to consider throughout this analysis and these must be assessed before the results in each momentum bin are combined so that the results are appropriately weighted. Initially, systematic uncertainties arising from the way the data is corrected and fitted will be described - these contribute minimally to total uncertainties. Secondly, systematics that are assessed principally using MC are detailed, with the acceptance dominating the total systematic uncertainty. Lastly, the effect of the measured radial field is accounted for.

3.2.1 Randomisation of VB oscillations

As described in Section 3.1.3, the vertical betatron oscillations are randomised out before fitting. This is done via the ROOT class TRandom3 that uses a Mersenne Twister pseudorandom number generator with a user-defined seed [78, 79]. 50 seeds are tested and the resulting distribution of measured EDM amplitudes is fitted with a Gaussian. This is only completed for dataset 3N, as it is computationally expensive to run. The results from this fit are summarised in table 3.3 including the error on the standard deviation to confirm enough seeds are used such that the spread is well determined. The uncertainty associated with the choice of seed will inversely scale with the size of the dataset, so the result from 3N is scaled based on $\sqrt{N_{3N}/N_{\rm Run}}$ to obtain an uncertainty for Run-2, 3a and 3b. This is done for each momentum bin and each station. As different seeds are used throughout, this uncertainty is not correlated between momentum bins, stations, or Runs.

Momentum	S	S12		18
bin (MeV)	$\sigma_{A_{\mathrm{EDM}}}$	$\Delta \sigma_{A_{\mathrm{EDM}}}$	$\sigma_{A_{ m EDM}}$	$\Delta \sigma_{A_{\mathrm{EDM}}}$
om (wev)	(μrad)	(μrad)	(µrad)	(μrad)
750–1000	1.09	0.23	1.40	0.31
1000 – 1250	1.16	0.26	1.29	0.24
1250 – 1500	0.87	0.16	0.57	0.07
1500 - 1750	0.83	0.16	0.77	0.12
1750 - 2000	0.94	0.23	0.95	0.14
2000 – 2250	0.67	0.15	0.76	0.14
2250 – 2500	0.94	0.17	0.84	0.14
2500-2750	0.64	0.11	1.01	0.13

Table 3.3: The Gaussian spread and associated uncertainty from a fit to the distribution of measured $A_{\rm EDM}$ for each station and momentum bin from 50 random seeds for vertical betatron randomisation. These numbers are for the 3N dataset.

3.2.2 Beam scraping correction

To assess the impact of any systematic uncertainty from the early-time correction, each of the three drift fit parameters as described in Section 3.1.3 is individually varied up then down by one standard deviation.

The drift correction is then applied with a shift to one parameter and the EDM analysis is repeated. The difference in $A_{\rm EDM}$ between the up and down shift for a given parameter is taken as the uncertainty. To avoid running over all track vertices repeatedly, the correction is applied to a non-modulated plot bin by bin and this is used to reconstruct the modulated plots. The result is three shifts in $A_{\rm EDM}$, one for each of the three parameters, which are combined in quadrature to give a total systematic uncertainty for each momentum bin and station. As the fit is unique to each Run, station, and momentum bin, the uncertainty is uncorrelated between them.

The impact of these shifts are presented in Tables 3.4, 3.5 and 3.6 for each parameter and station for Run-2, 3a, and 3b respectively. As expected, a shift in the constant offset C has minimal impact as the EDM amplitude is only sensitive to an oscillation in the average vertical decay angle. The decay rate of the fitted drift has the largest impact in most of the momentum bins, likely to do with a change in this parameter affecting more tracks later in the fill. The final totals after quadrature combination are in Tables 3.16–3.18.

Momentum		Fit pa	arameter	$\Delta A_{ m EDM}$	(µrad)	
bin (MeV)		S12		S18		
bili (MeV)	A_{drift}	$ au_{ m drift}$	C_{drift}	$A_{ m drift}$	$ au_{ m drift}$	C_{drift}
750-1000	0.07	0.14	~ 0	0.06	0.12	~ 0
1000 – 1250	0.05	0.10	~ 0	0.04	0.09	~ 0
1250 – 1500	0.04	0.08	~ 0	0.04	0.08	~ 0
1500 - 1750	0.03	0.07	~ 0	0.03	0.07	~ 0
1750 – 2000	0.03	0.07	~ 0	0.03	0.07	~ 0
2000 – 2250	0.03	0.06	~ 0	0.03	0.07	~ 0
2250 – 2500	0.02	0.05	~ 0	0.02	0.04	~ 0
2500-2750	0.01	0.03	~ 0	0.02	0.04	~ 0

Table 3.4: Summary of the beam scraping systematics in momentum bins for Run-2 in S12 and S18 where ~ 0 indicates the uncertainty is $< 0.005~\mu rad$.

3.2.3 g - 2 phase

The phase of the anomalous precession, which is used as the reference phase for the EDM fit, is determined by fitting the number oscillation for tracks with p > 1700 MeV. The effect of choosing this exact momentum threshold is assessed by using the fitted phase given momentum cuts 1700 ± 100 MeV. This cut is changed using dataset 3N and the anomalous precession fit is repeated. The variation in the phase for S12 and S18 is shown in Figure 3.32.

The central fitted phase from datasets Run-2, Run-3a, and Run-3b is moved by the same shift as measured in 3N and the resulting difference in $A_{\rm EDM}$ is taken as the systematic uncertainty. The results of this are summarised in Tables 3.7–3.9. This is the same reference phase used in all momentum bins and, as each dataset uses the same shifts, the uncertainty is considered to be correlated in both momentum and dataset.

M		Fit pa	arameter	ΔA_{EDM}	(µrad)	
Momentum bin (MeV)		S12			S18	
bili (Mev)	A_{drift}	$ au_{ m drift}$	C_{drift}	$A_{ m drift}$	$ au_{ m drift}$	C_{drift}
750 - 1000	0.03	0.09	~ 0	0.04	0.10	~ 0
1000 – 1250	0.03	0.07	~ 0	0.03	0.07	~ 0
1250 – 1500	0.02	0.06	~ 0	0.02	0.06	~ 0
1500 - 1750	0.02	0.06	~ 0	0.02	0.05	~ 0
1750 - 2000	0.02	0.05	~ 0	0.02	0.05	~ 0
2000 – 2250	0.02	0.05	~ 0	0.02	0.05	~ 0
2250 – 2500	0.01	0.04	~ 0	0.02	0.05	~ 0
2500-2750	0.01	0.02	~ 0	0.02	0.05	~ 0

Table 3.5: Summary of the beam scraping systematics in momentum bins for Run-3a S12 and S18 where \sim 0 indicates the uncertainty is $<0.005~\mu rad.$

Momentum -		Fit pa	arameter	$\Delta A_{ m EDM}$	(µrad)	
bin (MeV)		S12			S18	
bill (Mev)	$A_{ m drift}$	$ au_{ m drift}$	C_{drift}	A_{drift}	$ au_{ m drift}$	$C_{ m drift}$
750–1000	0.03	0.07	~ 0	0.03	0.08	~ 0
1000 – 1250	0.02	0.07	~ 0	0.02	0.06	~ 0
1250 - 1500	0.02	0.05	~ 0	0.02	0.04	~ 0
1500 - 1750	0.01	0.04	~ 0	0.01	0.04	~ 0
1750 - 2000	0.01	0.04	~ 0	0.02	0.04	~ 0
2000 – 2250	0.01	0.03	~ 0	0.01	0.04	~ 0
2250 - 2500	0.01	0.03	~ 0	0.02	0.04	~ 0
2500-2750	0.00	0.01	~ 0	0.02	0.04	~0

Table 3.6: Summary of the beam scraping systematics in momentum bins for Run-3b S12 and S18 where \sim 0 indicates the uncertainty is $<0.005~\mu rad.$

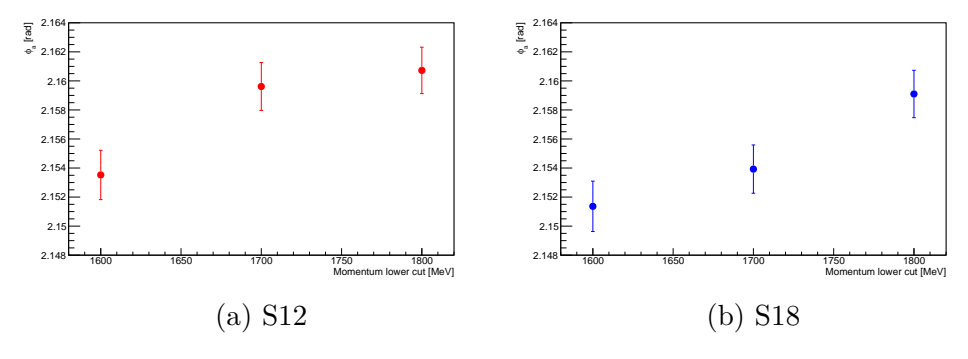


Figure 3.32: The fitted phase from the anomalous precession frequency after varying the lower cut on positron momentum ± 100 MeV from the nominal value of 1700 MeV for dataset 3N (a) S12 and (b) S18.

Momentum	$\Delta A_{ m EDN}$	μ (μrad)
bin (MeV)	S12	S18
750–1000	0.12	0.11
1000 – 1250	0.06	0.04
1250 – 1500	0.01	0.01
1500 - 1750	0.01	0.06
1750 - 2000	0.01	0.07
2000 – 2250	0.01	0.08
2250 – 2500	0.03	0.05
2500-2750	~ 0	0.08

Table 3.7: The difference in measured $A_{\rm EDM}$ after shifting the fitted g-2 phase by the difference from using 1600–1800 MeV for Run-2 S12 and S18, where ~ 0 indicates the uncertainty is < 0.005 µrad.

Momentum	$\Delta A_{ m EDN}$	μ (μrad)
bin (MeV)	S12	S18
750–1000	0.05	0.07
1000 – 1250	0.02	0.02
1250 – 1500	0.04	0.01
1500 – 1750	0.01	0.04
1750 - 2000	0.03	0.06
2000 – 2250	0.02	0.07
2250 – 2500	0.01	0.06
2500 – 2750	0.02	0.01

Table 3.8: The difference in measured $A_{\rm EDM}$ after shifting the fitted g-2 phase by the difference from using 1600–1800 MeV for Run-3a S12 and S18.

Momentum	$\Delta A_{ m EDN}$	₄ (μrad)
bin (MeV)	S12	S18
750–1000	0.09	0.15
1000 – 1250	0.07	0.02
1250 – 1500	0.04	0.02
1500 – 1750	0.01	0.07
1750 - 2000	0.00	0.04
2000 – 2250	0.02	0.07
2250 – 2500	0.01	0.08
2500-2750	~ 0	0.03

Table 3.9: The difference in measured $A_{\rm EDM}$ after shifting the fitted g-2 phase by the difference from using 1600–1800 MeV for Run-3b S12 and S18, where ~ 0 indicates the uncertainty is < 0.005 µrad.

3.2.4 g-2 momentum dependent phase

The momentum-dependent phase ϕ_a^p is extracted from the anomalous precession frequency fits with an associated uncertainty. The systematic effect of this on the EDM measurement is assessed by varying the phase by its uncertainty, refitting the data, and taking the shift in $A_{\rm EDM}$ as the systematic such that

$$\Delta A_{\text{EDM}}^{\phi_a^p} = \left| A_{\text{EDM}} \right|_{\phi_a^p = \phi_a^p - \Delta \phi_a^p} - \left| A_{\text{EDM}} \right|_{\phi_a^p = \phi_a^p + \Delta \phi_a^p}. \tag{3.2.1}$$

The shifts are not applied to the blinding signal and are repeated separately for each dataset, station, and momentum bin. The uncertainties from varying the momentum-dependent anomalous precession phase are displayed in Tables 3.16–3.18 and are unique to each fit, making the uncertainty uncorrelated.

3.2.5 g-2 amplitude

The fitted amplitude of the anomalous precession is used in the EDM fit and also has an associated uncertainty. Similarly to the phase, the amplitude A_N is varied by $\pm 1\sigma$ and the EDM fit repeated in each momentum bin and for each dataset. Again, this is not applied to the blinding signal and the total shift in $A_{\rm EDM}$ is taken as the systematic such that

$$\Delta A_{\text{EDM}}^{A_N} = \left| A_{\text{EDM}} \right|_{A_N = A_N - \Delta A_N} - \left| A_{\text{EDM}} \right|_{A_N = A_N + \Delta A_N}. \tag{3.2.2}$$

The results of varying A_N are displayed in Tables 3.16–3.18. As for the momentum dependent g-2 phase, the fit is unique, so the uncertainty is uncorrelated.

3.2.6 CBO fit parameters

The uncertainty of the CBO parameters in the anomalous precession fit must also be propagated through to an error on $A_{\rm EDM}$. Similarly to above, both the amplitude $A_{\rm CBO}$ and phase $\phi_{\rm CBO}$ are varied by $\pm 1\sigma$ and the EDM fit repeated for every momentum bin, station, and dataset. Without applying this to the blinding signal, the total shift in $A_{\rm EDM}$ is taken as the systematic such that

$$\Delta A_{\text{EDM}}^{A_{\text{CBO}}} = \left| A_{\text{EDM}} \right|_{A_{\text{CBO}} = A_{\text{CBO}} - \Delta A_{\text{CBO}}} - \left| A_{\text{EDM}} \right|_{A_{\text{CBO}} = A_{\text{CBO}} + \Delta A_{\text{CBO}}}, \tag{3.2.3}$$

and

$$\Delta A_{\text{EDM}}^{\phi_{\text{CBO}}} = \left| A_{\text{EDM}} \right|_{\phi_{\text{CBO}} = \phi_{\text{CBO}} - \Delta \phi_{\text{CBO}}} - \left| A_{\text{EDM}} \right|_{\phi_{\text{CBO}} = \phi_{\text{CBO}} + \Delta A_{\text{CBO}}} \right|. \quad (3.2.4)$$

The impact of varying $A_{\rm CBO}$ and $\phi_{\rm CBO}$ are displayed in Tables 3.16–3.18. There is no correlation between datasets for these uncertainties.

3.2.7 $R_{\rm acc}(\lambda)$ uncertainties

There are several systematic uncertainties arising when using MC to determine the acceptance. Firstly, there is a statistical error on the acceptance coming from the combination of the errors on the measured *all*

decays amplitudes before and after applying the acceptance map weighting. As the same MC sample is used, this is correlated between datasets, but the stations and momentum bins are treated independently. Furthermore, weighting the MC to match data and the tracker alignment are quantified as uncertainties on the acceptance and are discussed in this section. The uncertainty from the tracking resolution is also considered here.

For the tracker alignment, MC is produced where both tracker positions have been shifted in vertical position and tilted vertically, relative to the world coordinates. These are the two parameters with the biggest impact on vertical angle and, hence, the EDM. The alignment shifts are based on the uncertainties from laser surveys conducted during Run-1 and Run-2. For each station the position relative to the centre of the quadrupoles are:

$$\begin{split} y^{S12} &= 0.55 \pm 0.60 \text{ mm}, \\ y^{S18} &= 0.65 \pm 0.60 \text{ mm}, \\ \theta_y^{S12} &= 40 \pm 230 \text{ µrad}, \\ \theta_y^{S18} &= -410 \pm 230 \text{ µrad}. \end{split}$$

There are also uncertainties on the internal alignment but the effect of these is considered negligible.

In the MC the trackers are shifted ± 1 mm in vertical position and tilted by $\pm 0.1^{\circ} \approx 1.7$ mrad - an overestimate which can then be scaled down to the appropriate size. Tracks from these samples are used to produce new acceptance maps and the acceptance analysis, as outlined in Section 2.4.2, is repeated with these new maps. Finally, the alignment uncertainty is given as an uncertainty on $R_{\rm acc}$ using the change in acceptance from nominal alignment. The alignment is different for each station, but the uncertainty on the acceptance is correlated between momentum bins and datasets

Besides this, the MC is weighted to better match the data as described in Section 2.4.2 - the result of which leads to a closer, but not exact, match. Any remaining differences are used to set the scale for the MC-data matching uncertainty. This is done by adjusting the acceptance maps' mean and RMS in both y and θ_y and propagating the difference through to the acceptance factor. To allow for interpolation of any given mismatch in mean or RMS of y and θ_y , the change in acceptance under these shifts is fitted with an appropriate function. Then, the uncertainty in the acceptance can be extracted using the differences in data and MC distributions for a given dataset.

Relatedly, it was noted during the MC closure test that the final result was falling $\sim 6\%$ short of the expected tilt, given the inputted EDM. This problem only existed when using acceptance corrections that had been weighted to data. Hence, it was deduced that re-weighting the Flat MC to match data was introducing a systematic discrepancy between measured EDM from the acceptance-weighted all decays sample and the true tracks. For the acceptance map method to work, these results need to agree, as they do before data-weighting. To counteract this effect an extra scaling factor must be introduced so that closure is achieved.

Accordingly, the scaling is calculated by performing a weighted least squares minimisation to bring the $A_{\rm EDM}$ s from data- and acceptance-weighted all decays down to agree with the data-weighted true track $A_{\rm EDM}$ s across momentum bins. A scan around the minimum is completed to determine the scaling and its uncertainty. To best determine the uncertainty, the binning is fine enough to ensure three stable significant figures and the largest of the two limits either side is used, this also means flatness around the minimum is accounted for.

	Run-2	Run-3a	Run-3b
Station 12	0.865 ± 0.008	0.868 ± 0.005	0.890 ± 0.005
Station 18	0.990 ± 0.005	0.990 ± 0.005	0.995 ± 0.005

Table 3.10: Results from weighted least squares minimisation to align the data- and acceptance-weighted *all decays* to the data-weighted *true track* EDM values for each dataset and station.

This procedure is repeated for each Run and station, with the resultant scaling factors shown in Table 3.10. The variation between datasets is to be expected as they have slightly different beam conditions. Similarly, the difference between station 12 and 18 is likely due to each seeing a slightly different part of the beam. Given the method used to extract these uses one MC sample, the uncertainty is completely correlated between results.

In hindsight, the alterations to the beam shape exacerbated this and simultaneously exposed the consequences of imperfect matching between MC and data on the acceptance. Looking forward, this effect can be greatly reduced with better agreement between the MC beam and the real beam but, without perfect congruity, there may always be a small effect to account for.

Lastly, to quantify the impact of the tracking resolution the $reco\ track$ and the $true\ track$ samples are compared. Both of these samples are used to produce an acceptance correction. Then, the quadrature difference of the uncertainty on $A_{\rm EDM}$ from all decays weighted to $reco\ tracks$ versus weighted to $true\ tracks$ is taken as the tracking resolution uncertainty assuming that the $true\ tracks$ weighting carries only a statistical error. Technically, this uncertainty is an additional uncertainty on $A_{\rm EDM}$ in radians but, as it is calculated via the acceptance, it is listed here.

Tables 3.11 and 3.12 summarise the combined uncertainties on $R_{\rm acc}(\lambda)$. For the final combination (see Section 3.4) the alignment dominates the acceptance related uncertainties, the MC-data matching and extra scaling having similar size and are the next biggest contribution, and the statistical uncertainty is the smallest.

Quoted as an uncertainty on $A_{\rm EDM}$, the track reconstruction uncertainty is given in Table 3.13. This uncertainty is not expected to vary with momentum as much as is shown, especially as no obvious trend is seen, so it is likely caused by statistical fluctuations in the MC sample. Given that the statistical uncertainties dominate this is not currently a concern. However, these uncertainties could lead to a misrepresentative weighting in a systematically dominated analysis, so a different or non-momentum-dependent assessment of this uncertainty may be necessary.

Momentum	Total un	certainty or	$R_{\rm acc}(\lambda)$
bin (MeV)	Run-2	Run-3a	Run-3b
750–1000	0.0105	0.0103	0.00998
1000 - 1250	0.0121	0.0120	0.0119
1250 – 1500	0.0110	0.0109	0.0108
1500 - 1750	0.00989	0.00990	0.00998
1750 - 2000	0.0114	0.0113	0.0113
2000 – 2250	0.00979	0.00948	0.00895
2250 – 2500	0.0189	0.0178	0.0167
2500-2750	0.0541	0.0542	0.0545

Table 3.11: The total (unitless) uncertainty on the acceptance for S12 from combining all uncertainties in quadrature.

Momentum	Total ur	certainty or	$R_{\rm acc}(\lambda)$
bin (MeV)	Run-2	Run-3a	Run-3b
750–1000	0.0117	0.0102	0.00971
1000 - 1250	0.0131	0.0119	0.0115
1250 – 1500	0.0123	0.0112	0.0109
1500 - 1750	0.0110	0.00976	0.00961
1750 - 2000	0.0126	0.0114	0.0112
2000 – 2250	0.0112	0.00957	0.00881
2250 – 2500	0.0197	0.0179	0.0169
2500 - 2750	0.0544	0.0542	0.0545

Table 3.12: The total (unitless) uncertainty on the acceptance for S18 from combining all uncertainties in quadrature.

Momentum	$\Delta A_{\rm EDM}$ from	track reconstr	uction (µrad)
bin (MeV)	Run-2	Run-3a	Run-3b
750–1000	0.176	0.169	0.194
1000 - 1250	1.241	1.307	1.347
1250 - 1500	0.095	0.099	0.074
1500 - 1750	0.351	0.413	0.333
1750 - 2000	0.166	0.167	0.168
2000 – 2250	0.617	0.612	0.672
2250 – 2500	0.171	0.175	0.177
2500-2750	0.801	0.816	0.832

Table 3.13: Summary of the track reconstruction uncertainty in each momentum bin and Run. The same MC sample is weighted to better match each Run.

3.2.8 $R_{e^+}(\lambda)$ uncertainty

To account for the reduction in the amplitude of the $\langle \theta_y \rangle$ oscillation in the lab frame due to the decay properties of the muon, the all decays sample is used. The g-2 simulation makes use of GEANT4 software that includes first order radiative corrections unlike the analytic form of the reduction given in Equation 2.2.26. By using the all decays sample, $R_{e^+}(\lambda)$ can be extracted with a more accurate approximation of the radiative corrections included.

In each momentum bin, the EDM analysis is completed to extract the measured tilt. In principle, this measured tilt $\delta_{m, all \ decays}$ is reduced from the true lab frame tilt δ by the reduction factor $R_{e^+}(\lambda)$ such that

$$\delta_{m, all \ decays} = R_{e^+}(\lambda)\delta,$$
 (3.2.5)

where the true tilt from the injected EDM $\delta = \delta_{30\times BNL}$. Figure 3.33 shows the results of this extraction compared to the functional form of $R_{e^+}(\lambda)$ in Equation 2.2.26. The reduction of average vertical decay in the lab frame at the point of maximum tilt is greater when using the all decays sample than the functional form because additional radiative corrections mean fewer positrons are emitted in the direction of spin than in the Born-level approximation [16].

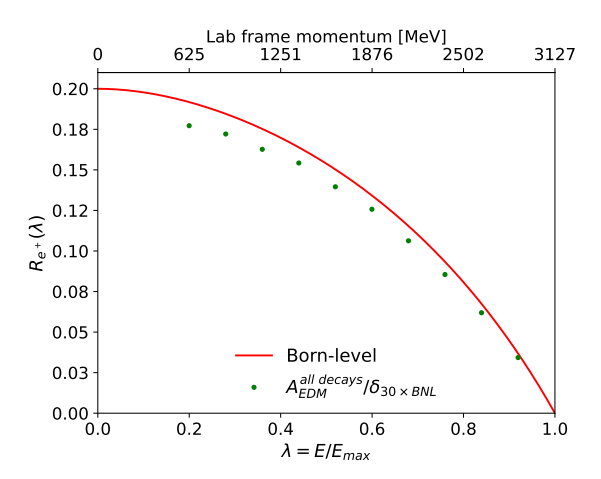


Figure 3.33: The functional form of $R_{e^+}(\lambda)$ at the Born-level (red) compared to the extraction from MC including higher order radiative correction (green).

The associated uncertainty comes from the uncertainty on the fitted amplitude scaled by the tilt: $\Delta R_{e^+}(\lambda) = \Delta A_{\rm EDM}^{all\ decays}/\delta_{30\times BNL}$. The reduction factors and uncertainties are summarised in Table 3.14 and are unique for each momentum bin, but correlated between Runs and stations.

3.2.9 Polarisation

The polarisation as taken from [61] does not have an associated uncertainty. In place of this an error of 1% has been assumed such that

$$R_P = 0.96 \pm 0.01.$$
 (3.2.6)

This is the same for all results and, hence, is completely correlated.

Momentum bin (MeV)	$R_{e^+}(\lambda)$	$\Delta R_{e^+}(\lambda)$
750–1000	0.1818	0.0009
1000 – 1250	0.1718	0.0008
1250 - 1500	0.1629	0.0007
1500 - 1750	0.1474	0.0006
1750 - 2000	0.1328	0.0006
2000 – 2250	0.1122	0.0005
2250 – 2500	0.0902	0.0005
2500-2750	0.0654	0.0005

Table 3.14: The *all decays* amplitudes and their uncertainties scaled to the injected tilt of 1.69 mrad to give the reduction factor $R_{e^+}(\lambda)$ and its uncertainty.

3.2.10 Muon momentum spread

The momentum RMS of the stored muons is 0.15% [27]. This is taken as a conservative uncertainty on γ such that

$$R_{\gamma} = \frac{1}{\gamma} \pm \frac{0.0015}{\gamma^2}.\tag{3.2.7}$$

As with the polarisation, this uncertainty is same for all results so it is completely correlated.

3.2.11 Radial field

As described in Section 2.5 the radial field measurement using the ESQs in Run-4 is used to extrapolate back to give the average radial field in each of the three datasets. This is then added to the measured tilt with an associated uncertainty - a positive radial field is equivalent to a negative EDM.

The extrapolated radial field measurements and corresponding tilts are described in Table 3.15. The impact of the average radial field is the same in both stations and for all momenta, hence it is correlated between these but not between Runs. The error on the rest frame tilt is a subdominant systematic uncertainty.

Dataset	$\langle B_r \rangle$ (ppm)	δ^* (µrad)
Run-2	14.9 ± 4.5	14.9 ± 4.5
Run-3a	11.2 ± 2.2	11.2 ± 2.2
Run-3b	12.0 ± 2.5	12.0 ± 2.5

Table 3.15: Results of extrapolating the average radial field using the Run-4 data measurement. Showing the average radial field and the corresponding lab frame precession plane tilt for each of the three datasets.

3.2.12 Systematic uncertainty summary

A summary of all the systematic uncertainties is given in Tables 3.16–3.18 as an uncertainty on the rest frame tilt with the statistical uncertainty for comparison. The statistical and systematic uncertainties on $A_{\rm EDM}$ are scaled by the four R-factors to take them to a rest frame tilt uncertainty. The uncertainties from the four R-factors and the Flat MC correction are calculated via standard error propagation such that e.g.

$$\Delta \delta^* = \frac{\delta^*}{R_{\rm acc}} \Delta R_{\rm acc}. \tag{3.2.8}$$

This means that all five of these uncertainties as quoted in the table below are dependent on the amplitude and, as such, will be expected to decrease when the data is unblinded. It should also be noted that the statistical uncertainties are by far the dominant errors.

Momentum	> *						S12	* gygtp	matic	(lirad)					
Momentum	$\Delta \delta_*$	VR	Coroning.	}	$d\mathcal{H}$	Λ	$\Delta \delta^*$	* syste	systematic	(μrad)	Flat MC wrt	D .	R_{z}	D	R
750-1000	1711	302	78	$\frac{\varphi_a}{59}$	$\begin{array}{c c} & & & \\ & & \\ & & \\ & & \end{array}$	~ 0	4 4	φCBO	90	17 _{acc}	74	$\frac{n_{e^+}}{42}$	88	4	~ 0
1000 - 1250	1229	292	51	27	~ 0	<u> </u>	ಏ	<u> </u>	583	100	65	34	78	4	~ 0
1250 - 1500	995	199	38	2	○0	\vdash	2	\vdash	40	162	70	34	83	4	∼0
1500-1750	1022	210	35	6	○0	2	ဃ	~ 0	167	96	68	33	81	4	~ 0
1750 - 2000	1023	248	35	4	0	0	4		82	98	69	35	82	4	∼0
2000-2250	1141	198	38	4	~ 0	<u> </u>	2	⊢	338	81	56	31	67	4	~ 0
2250 - 2500	1376	317	36	20	1	4		1	108	177	70	46	84	4	~ 0
2500-2750	1782	273	29	4	4	6	2	2 0	619	329	54	46	65	4	~ 0
							S18								
Momentum	$\Delta \delta^*$						$\Delta \delta^*$		systematic	(µrad)					
bin (MeV)	stat.	VB	Scraping	ϕ_a	ϕ_a^p	A_N	$A_{\rm CBO}$	$\phi_{ ext{CBO}}$	reco.	$R_{ m acc}$	Flat MC wt.	R_{e^+}	R_P	R_{γ}	B_r
750-1000	1516	349	60	50	2	<u> </u>	\vdash	သ	78	223	29	26	55	4	~ 0
1000 - 1250	1090	290	42	17	1	0	~ 0	4	507	229	52	44	100	4	~ 0
1250 - 1500	946	124	33	2	~ 0	0	0	2	38	125	42	33	81	4	~ 0
1500 - 1750	940	179	32	24	~ 0	0	~ 0	2	150	193	41	32	79	4	~ 0
1750 - 2000	947	230	32	32	\vdash	<u> </u>	0	2	73	167	39	31	74	4	~ 0
2000-2250	1048	202	38	39	1	0	~ 0	_	300	134	36	32	70	4	~ 0
2250 - 2500	1287	261	28	30	~ 0	೮٦	ဃ	1	97	326	48	50	92	4	~ 0
2500-2750	1648	395	33	55	ಬ	7	~ 0	~ 0	561	165	46	64	89	4	~ 0

indicates the uncertainty is < 0.5 µrad. Table 3.16: Summary of the systematics on the rest frame tilt in momentum bins for Run-2 S12 and S18 where ~ 0

34 72 2

	B_r	0 ~	0 ~	0 ~	0 ~	0 ~	0 ~	0 ~	0 ~
	R_{γ}	2	2	2	2	2	2	2	2
	R_P	59	75	92	72	84	98	88	107
	R_{e^+}	28	32	31	30	35	40	49	22
	Flat MC wt.	30	38	38	36	42	43	45	54
(prad)	$R_{ m acc}$	230	167	115	174	184	161	298	204
systematic (reco.	74	525	39	173	73	293	400	564
	$\phi_{ ext{CBO}}$	2	2	2	Η	П	Η	П	4
$\Delta \delta^*$	$A_{\rm CBO}$	-		Н		П	2	П	2
	A_N	0 ~	0 ~	0 ~	0 ~	0 ~	က	П	4
	ϕ_a^p	0 2	0 ~	0 ~	0 ~	0 ~	П	\vdash	0 ~
	ϕ_a	59	∞	2	16	24	33	33	7
	Scraping	44	31	26	25	23	28	30	34
	VB	288	244	105	151	194	170	221	332
$\Delta \delta^*$	stat.	1261	922	803	262	805	891	1098	1390
Momentum	bin (MeV)	750-1000	1000 - 1250	1250 - 1500	1500 - 1750	1750-2000	2000-2250	2250 - 2500	2500-2750

Table 3.17: Summary of the systematics on the rest frame tilt in momentum bins for Run-3a S12 and S18 where ~ 0 indicates the uncertainty is < 0.5 µrad.

1750-2000 2000-2250

Flat MC wt.

 $\begin{array}{c|c}
 \hline
 65 \\
 \hline
 65 \\
 \hline
 29 \\
 \hline
 15 \\
 \hline
 32 \\
 \hline
 43 \\
 \hline
 44 \\
 44 \\
 \hline
 44 \\
 \hline
 44 \\
 44 \\
 44 \\
 44 \\
 44 \\
 44 \\
 44 \\
 44 \\
 44 \\
 44 \\
 44 \\
 44 \\
 44 \\
 44 \\
 44 \\
 44 \\
 44 \\
 44 \\
 44 \\
 44 \\
 44 \\
 44 \\
 44 \\
 44 \\
 44 \\
 44 \\
 44 \\
 44 \\
 44 \\
 44 \\
 44 \\
 44 \\
 44 \\
 44 \\
 44 \\
 44 \\
 44 \\
 44 \\
 44 \\
 44 \\
 44 \\
 44 \\
 44 \\
 44 \\
 44 \\
 44 \\
 44 \\
 44 \\
 44 \\
 44 \\
 44 \\
 44 \\
 44 \\
 44 \\
 44 \\
 44 \\
 44 \\
 44 \\
 44 \\
 44 \\
 44 \\
 44 \\
 44 \\
 44 \\
 44 \\
 44 \\
 44 \\
 44 \\
 44 \\
 44 \\
 44 \\
 44 \\
 44 \\
 44 \\
 44 \\
 44 \\
 44 \\
 44 \\
 44 \\
 44 \\
 44 \\
 44 \\
 44 \\
 44 \\
 44 \\
 44 \\
 44 \\
 44 \\
 44 \\
 44 \\
 44 \\
 44 \\
 44 \\
 44 \\
 44 \\
 44 \\
 44 \\
 44 \\
 44 \\
 44 \\
 44 \\
 44 \\
 44 \\
 4$

Momentum bin (MeV)

750-1000

stat.

							7								
Λ omentum	$\Delta \delta^*$						Δ	$\Delta \delta^*$ systematic	matic ((prad)					
bin (MeV)	stat.	VB	Scraping	ϕ_a	ϕ_a^p	A_N	A_{CBO}	$\phi_{ ext{CBO}}$	reco.	$R_{ m acc}$	Flat MC wt.	R_{e^+}	R_P	R_{γ}	B_r
750-1000	2260	394	38	45	2	2	ш	2	94	131	36	34	71	2	
1000 - 1250	1638	385	31	29	2	2	∼0	2	595	79	33	28	65	2	
1250-1500	1327	262	23	15	0	<u> </u>	2	2	30	108	29	23	57	2	~ 0
1500-1750	1366	277	17	57	\vdash	<u> </u>	4	~ 0	149	74	30	25	60	2	~ O
1750-2000	1369	327	19	2	∼0	\vdash	ယ		78	108	46	38	91	2	
2000 - 2250	1530	262	18	∞	~ 0	○0		ಬ	348	97	46	43	92	2	
2250 - 2500	1853	421	20	ဃ	2	2	7	ಬ	106	104	33 36	36	65	2	$2 \sim 0$
2500 - 2750	2357	358	10	2	~ 0	4	9	1	617	598	59	84	117	2	~ 0
							S18								

indicates the uncertainty is < 0.5 µrad. Table 3.18: Summary of the systematics on the rest frame tilt in momentum bins for Run-3b S12 and S18 where ~ 0

3.3 Cross-checks

As part of the EDM search, there are several approaches to the analysis that are completed to serve as a cross-check for the main result. The outcomes of these are summarised here, including a non-momentum-binned approach, fit start-time scans, and a check for any vertical angle oscillation at a known frequency - the CBO.

3.3.1 Analysis without momentum binning

The analysis described in Section 3.1.4 is also completed for track vertices from the full momentum range 750–2750 MeV. This serves as a cross-check that the result is consistent with the muon EDM result from combining the eight bins, albeit with less sensitivity.

To do this, the anomalous precession fit is repeated for 750–2750 MeV tracks to extract the amplitude, phase, and CBO parameters to be used in the denominator. The reference anomalous precession frequency phase is the same as extracted in a momentum binned analysis. In addition, the acceptance is calculated separately and $R_{e^+}(\lambda)$ is found using the same method - taking the fitted *all decays* amplitude for the momentum range and scaling it to the true inputted tilt.

The non-momentum-binned anomalous precession fits for each station can be seen in Figures 3.34–3.35 and the EDM fits in Figure 3.36–3.37. A summary of the final measured tilts in the lab frame via this method can be found in Table 3.19 including only statistical uncertainties. Combining these via a weighted average gives a muon EDM of $(8.05\pm0.24)\times10^{-19}~e\cdot\text{cm}$ compared with $(7.96\pm0.18)\times10^{-19}~e\cdot\text{cm}$ from the statistical combination using eight momentum bins (see Section 3.4). These results are determined to agree and it should be noted that neither result includes any systematic uncertainties.

Dataset	$d_{\mu} \ (\times 10^{-4})$	$^{-19} e \cdot \text{cm}$
Dataset	S12 1 bin	S18 1 bin
Run-2	8.73 ± 0.60	8.59 ± 0.57
Run-3a	7.25 ± 0.52	8.08 ± 0.48
Run-3b	7.36 ± 0.80	8.24 ± 0.75

Table 3.19: A comparison of the rest frame tilts as measured using one momentum bin 750-2750 MeV for each dataset and station.

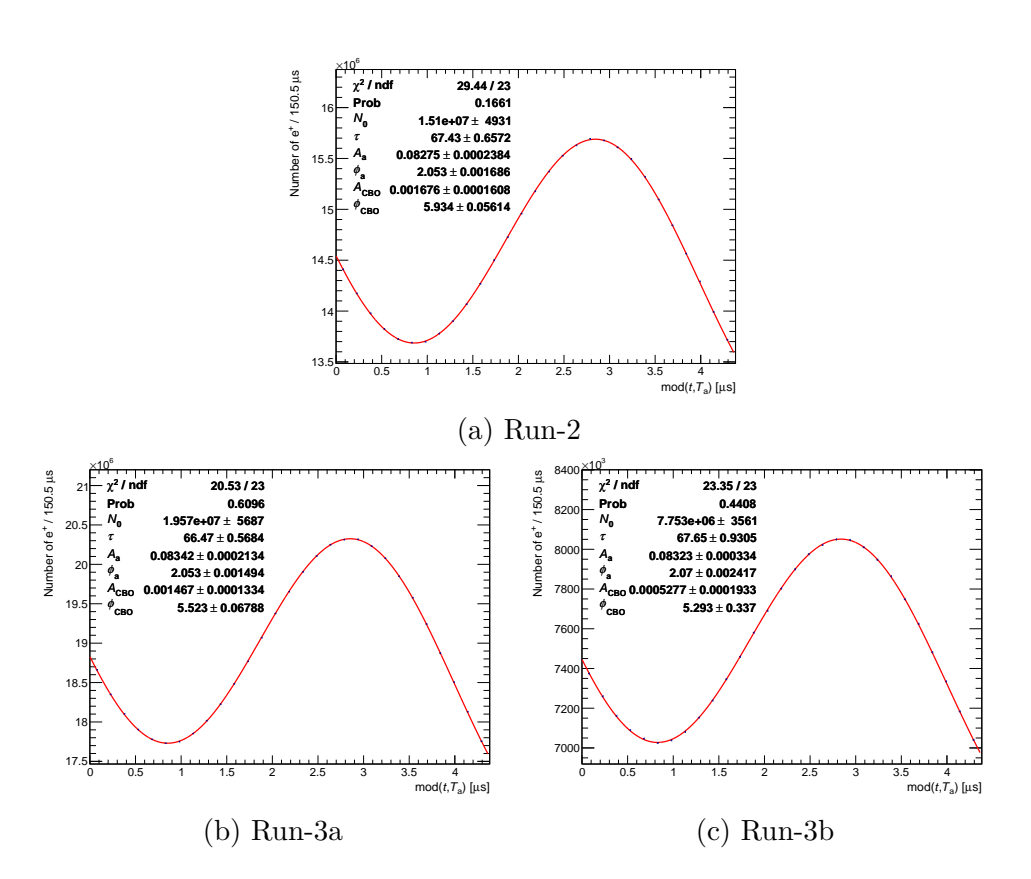


Figure 3.34: Fit to the anomalous precession frequency for track vertices $750 \le p < 2750$ MeV from S12 for all datasets.

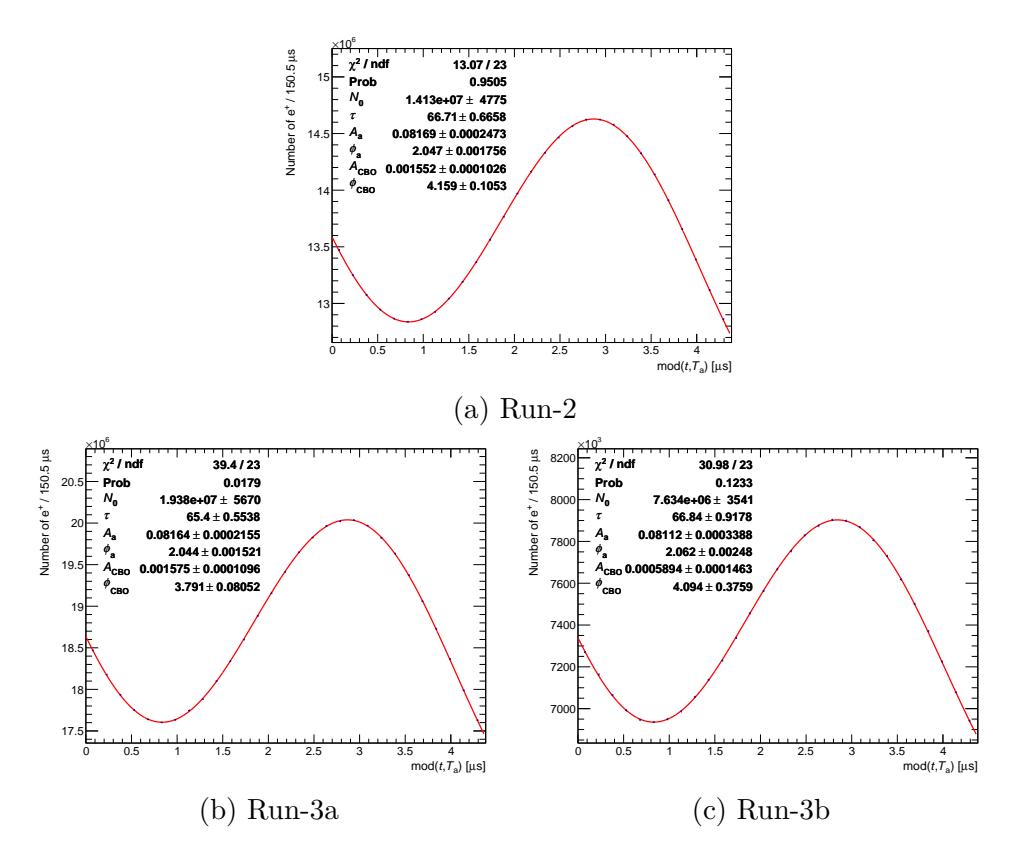


Figure 3.35: Fit to the anomalous precession frequency for track vertices $750 \le p < 2750$ MeV from S18 for all datasets.

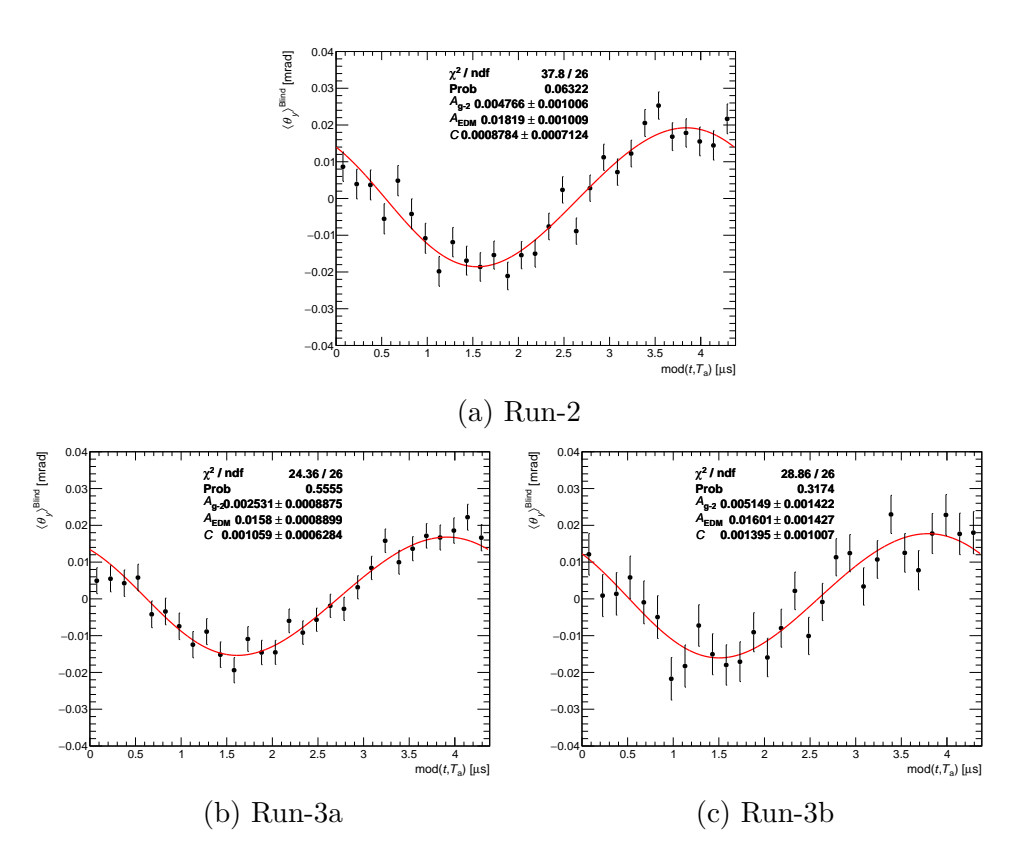


Figure 3.36: Fit to the average vertical angle for track vertices $750 \le p < 2750$ MeV from S12 for all datasets.

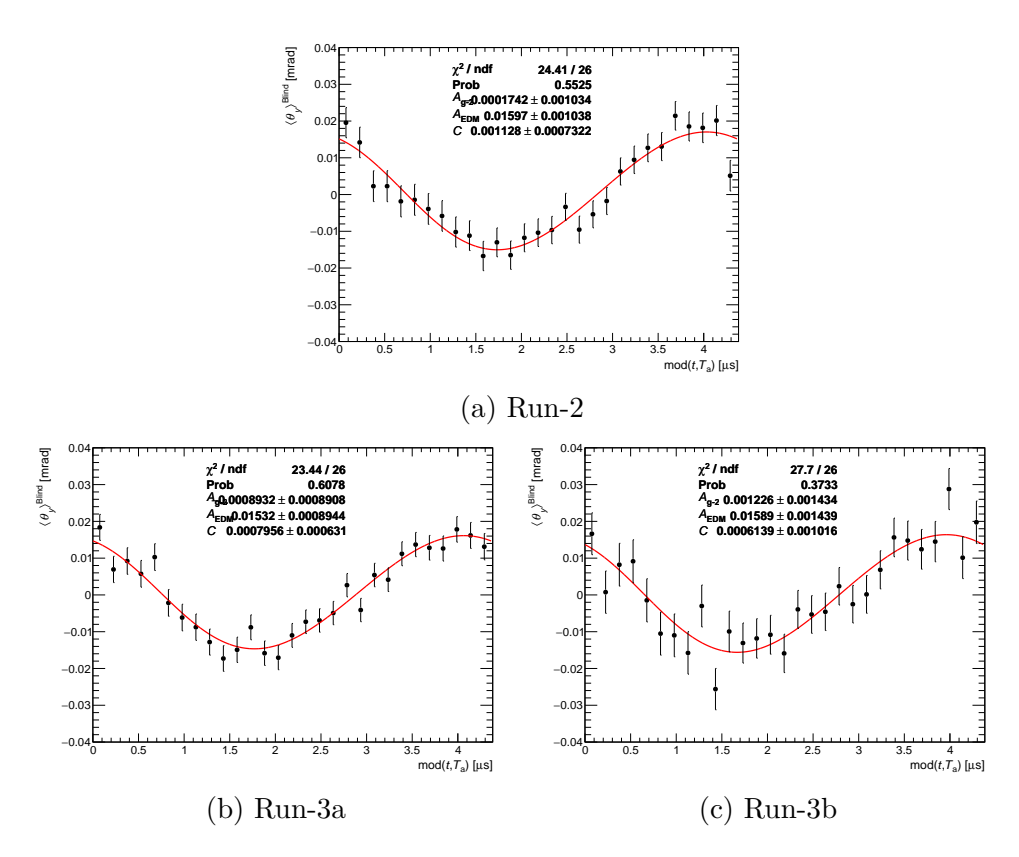


Figure 3.37: Fit to the average vertical angle for track vertices 750 $\leq p < 2750$ MeV from S18 for all datasets.

3.3.2 Fit start-time scans

The fit start-time is determined by balancing the uncertainties from statistical gains against decreasing tracking efficiency early in the fill. To check for any impact on the measured amplitude based on start-time, a fit start-time scan is performed. Firstly, non-modulated number plots and vertical decay angle plots are used to make corresponding modulated plots for a given start time. This is done for each Run, station, and momentum bin. The blinded analysis is then completed by fitting both the anomalous precession and the average vertical decay angle for a particular start-time. Start-times range from the nominal $6T_a$ and increase in integer values of T_a to $41T_a$.

Results from the fit start-time scans are shown for all Runs, stations, and momentum bins in Appendix B. The red bands show the allowed 1σ variation σ_{Δ} between a parameter measured from two datasets where one dataset set is a subset of the other. The allowed variation is given by

$$\sigma_{\Delta} = \sqrt{\sigma_2^2 - \sigma_1^2},\tag{3.3.1}$$

as was developed for the BNL ω_a analysis [30]. Fits from the larger dataset, i.e. earlier start-time, are associated with uncertainty σ_1 and the subset dataset, i.e. later start-time, are associated with σ_2 . All Runs see the majority of the $A_{\rm EDM}$ errors (statistical only) falling within the allowed variation across stations and momentum bins. Some datasets diverge more than others, but this is not unexpected given 48 separate scans. The two other floating parameters in the EDM fit, A_{g-2} and C, are also shown to check for any significant drifts.

Additionally, the fit start-time scans are repeated on unmodulated plots. An example for one Run and station is illustrated in Figure 3.38 where an oscillation is visible. This likely arises from slow terms that are not accounted for in a 9-parameter ω_a fit. However, the size of the oscillation is considered to be negligible compared with statistical and other systematic uncertainties. Additionally, the start-time chosen does not sit at a maximum or minimum of the oscillation.

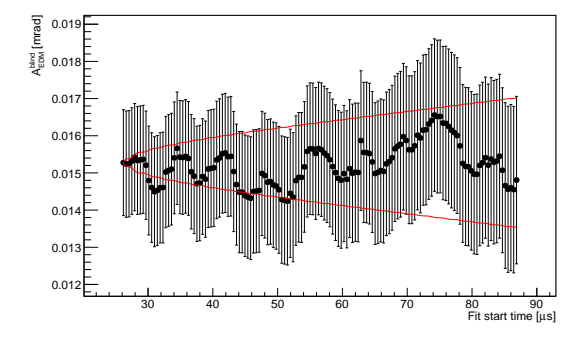


Figure 3.38: Fit start-time scans for $A_{\rm EDM}$ Run-3b S12 using the full momentum range $750 \le p < 2750$ MeV and unmodulated plots. This scan uses a nine-parameter fit fixing ω_a and $\omega_{\rm CBO}$.

3.3.3 Check for oscillation at the CBO frequency

A further cross-check involves applying the same principles of the analysis but fixing the oscillation frequency to something other than ω_a , with the assumption that there should be no observable oscillation in $\langle \theta_y \rangle$ at this frequency. However, if there is an observation, the impact on the EDM result must then be assessed.

The CBO frequency is used to set the x-axis limits for the modulo plots and fixed in the fits as ω_a is normally. Then, the anomalous precession frequency fits follow closely the EDM analysis by using an 8-parameter fit with fixed ω_a and predetermined ω_{CBO} . The CBO phase extracted from these fits is then used to set the reference phase in the 'EDM' fit such that

$$\langle \theta_y \rangle (t) = \frac{A_1 \cos(\omega_{\text{CBO}} t + \phi_{\text{CBO}}) + A_2 \sin(\omega_{\text{CBO}} t + \phi_{\text{CBO}})}{(1 + A_N \cos(\omega_a t + \phi_a^p)) (1 + A_{\text{CBO}} \cos(\omega_{\text{CBO}} t + \phi_{\text{CBO}}))} + C,$$
(3.3.2)

with in-phase and out-of-phase amplitudes A_1 and A_2 .

Example fits can be seen in Figure 3.39, with the amplitudes for each station shown in Figure 3.40. Across all stations and Runs the results show non-zero amplitudes for the $\langle \theta_y \rangle$ oscillation, which is predicted to arise due to acceptance effects varying at the CBO frequency. In Figure 3.40a the second momentum bin shows a larger discrepancy between the stations than the other bins. As momentum acts as a proxy for azimuthal position, this observation may arise due to effects of closed orbit distortion coupling with the CBO and acceptance. This reasoning is motivated as the discrepancy is reduced but also visible in Run-3a, but not observed in Run-3b, which is known to have a smaller CBO amplitude [27]. Moreover, the impact on the EDM analysis from any size oscillation at f_{CBO} must be determined.

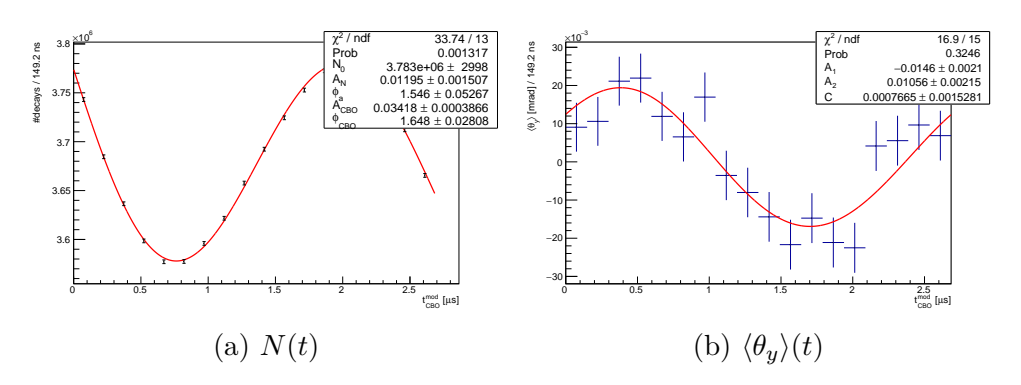


Figure 3.39: Example results for CBO cross-check fits for Run-2 S12 1500 MeV showing (a) number oscillation fit and (b) vertical angle fit

Specifically, having seen an oscillation in $\langle \theta_y \rangle$ at $f_{\rm CBO}$, a study is completed to establish if this could cause an EDM-like amplitude to be measured in the main analysis. Taking representative values for the CBO fit parameters, the oscillation can be sampled from to produce a pseudo EDM analysis. From this, the induced EDM amplitudes are determined to be on the order of 0.1 µrad, which is around two orders

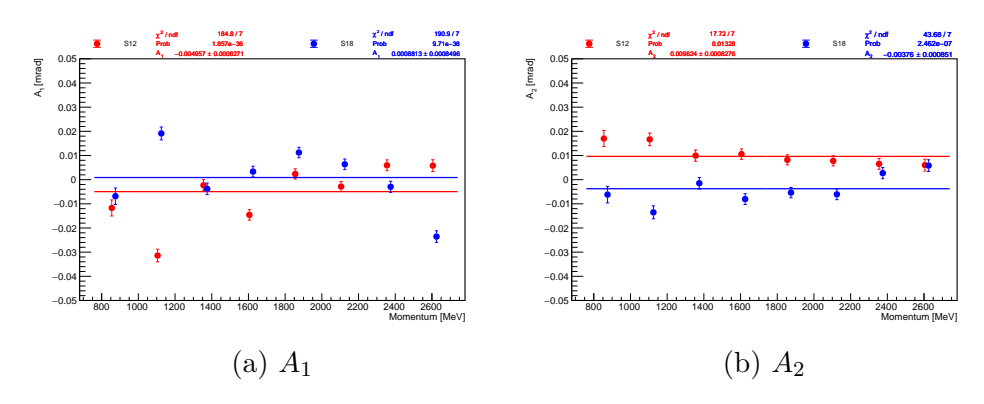


Figure 3.40: Example CBO cross-check vertical angle oscillation amplitudes for Run-2 showing (a) in-phase and (b) out-of-phase amplitudes for both stations.

of magnitude smaller than the statistical uncertainties and therefore no extra systematic uncertainty is assigned.

3.4 Combining results

Once the blinded EDM amplitude is extracted for each momentum bin, station, and Run, the four reduction factors are applied: $R_{\rm acc}(\lambda)$ and $R_{e^+}(\lambda)$ account for any momentum-dependent reductions, and R_P and R_γ take the measured amplitude to the rest frame tilt. For each dataset, the tilt due to the radial field is added, allowing the measured rest frame tilt due to an EDM to be converted to a muon EDM (d_μ) via equation 2.2.10.

Including all 8 momentum bins, 2 stations, and 3 datasets, there are 48 measurements of d_{μ} that are combined using a standard method called the Best Linear Unbiased Estimate (BLUE) [80]. This method accounts for statistical uncertainties, systematic uncertainties, and any correlations between them using a complete error matrix. The systematic uncertainties can be correlated across any combination of dataset, station, or momentum bin; these are summarised in table 3.20. Correlations are also visualised in Figure 3.41a and, with the inclusion of statistical uncertainties in Figure 3.41b, the statistical uncertainty domination is clear.

The final systematic uncertainty is determined from the quadrature difference between the uncertainty on the combination with statistical errors only compared to the combination including systematic errors. Results of the full combination are shown in Figure 3.42, where the central value is found using all uncertainties.

As a further cross-check, the combination is repeated in each Run (shown in Figure 3.43) and for each station (shown in Figure 3.44). The results are summarised in Table 3.21. Combination probabilities for these breakdowns vary between 0.87 and 0.08, which is deemed reasonable. The largest disagreement is between S12 and S18; assuming zero correlation, this disagreement is 1.4σ , which is considered acceptable.

Furthermore, the stability of the combination is checked by dropping one result and repeating the fit to assess its pull. Overall, the fit appears

	Q 1		1	
Source	Scales		rrelation	
Dource	with A_{EDM}	Momentum	Station	Dataset
VB rand.				
Beam scraping				
ϕ_a		Y		Y
ϕ^p_a				
A_N				
A_{CBO}				
$\phi_{ ext{CBO}}$				
$R_{ m acc}$	Y			Y
Alignment	Y	Y		Y
Data-MC match	Y	Y	Y	Y
Flat MC wt.	Y	Y	Y	Y
Track reco.			Y	
R_{e^+}	Y		Y	Y
R_P	Y	Y	Y	Y
R_{γ}	Y	Y	Y	Y
Radial field		Y	Y	

Table 3.20: Summary of systematic uncertainties from each source. Some sources are absolute uncertainties on $A_{\rm EDM}$, and some are uncertainties on the R-factors and, as such, will scale with the size of the measured amplitude as seen in equation 3.2.8. Whether the uncertainties scale is indicated in the table, alongside the correlations between momentum bins, stations, and datasets.

stable; around 2–3 bins are expected to have a pull above 2σ (5% of 48 bins), and 3 are seen. The projected pull distribution is consistent with a mean of 0 and width 1.

Lastly, the impact of each systematic source is assessed by dropping it from the combination. The contribution from the dropped source is estimated by taking the quadrature difference in the total uncertainty with and without including it in the fit. Figure 3.46 shows a comparison of the uncertainties. The dominant systematic uncertainties on the blinded analysis are from ΔR_P , the alignment, and track reconstruction. However, all individual systematic uncertainties are at least a factor of 2 smaller than the statistical uncertainty.

Assuming the unblinded result measures $A_{\text{EDM}} = 0$ such that R-factor

Dataget	Combination	Uncerta	inty (×10	$e^{-19} \cdot \text{cm}$	Duob
Dataset	$\times 10^{-19} e \cdot \text{cm}$	Total	Stat.	Syst.	Prob.
All	7.96	0.24	0.18	0.16	0.44
Run-2	8.28	0.37	0.31	0.19	0.87
Run-3a	7.82	0.33	0.27	0.18	0.41
Run-3b	8.23	0.46	0.42	0.19	0.09
S12	7.69	0.31	0.27	0.16	0.82
S18	8.32	0.33	0.25	0.21	0.19

Table 3.21: Summary the combinations and their uncertainties.

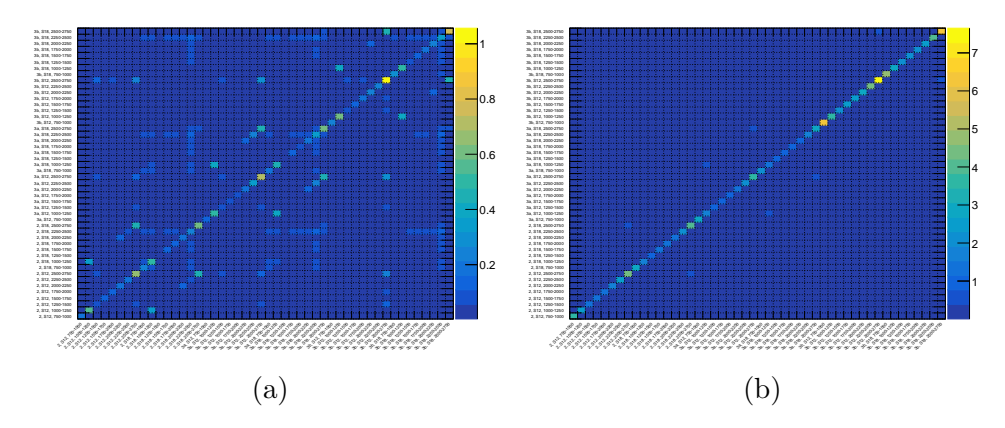


Figure 3.41: The total covariance matrices for blinded data including (a) systematic uncertainties and (b) statistical and systematic uncertainties.

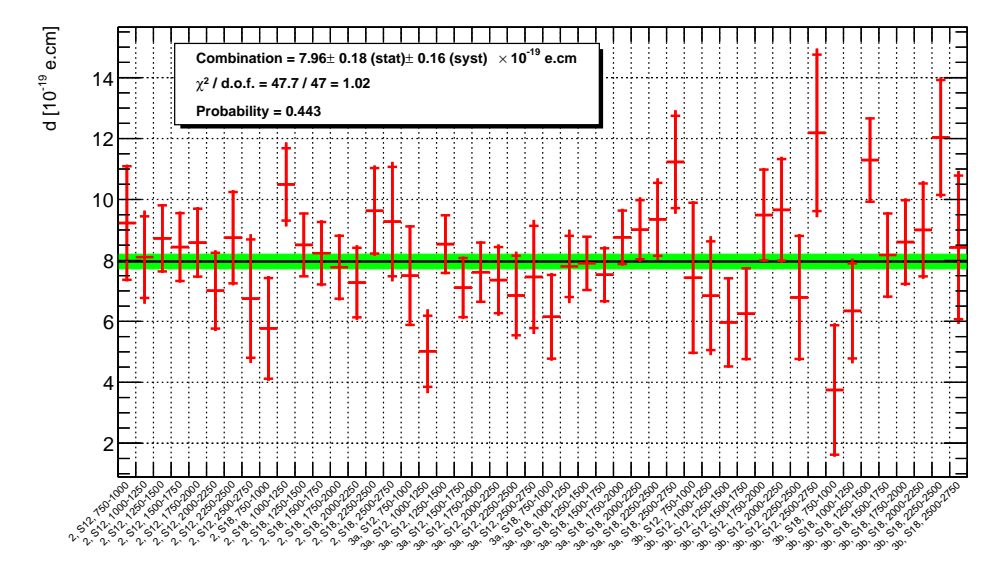


Figure 3.42: The combination of individual results in each momentum bin, station, and Run. For each result, the inner error bar represents the statistical uncertainty and the outer the combined statistical and systematic uncertainty.

uncertainties go to zero as motivated in Appendix C, the best estimate of the blinded result and its uncertainty is

$$d_{\mu} = 8.10 \pm 0.18 (\mathrm{stat.}) \pm 0.07 (\mathrm{syst.}) \times 10^{-19} \ e \cdot \mathrm{cm}.$$

Which can be compared to the result including R-factor uncertainties given the size of the blinded $A_{\rm EDM}$ that gives

$$d_{\mu} = 7.96 \pm 0.18 \text{(stat)} \pm 0.16 \text{(syst)} \times 10^{-19} \ e \cdot \text{cm},$$

where the systematic uncertainty contribution is larger and the central value is also shifted. The blinded result is the value from the fit with the unknown EDM injected, it is therefore expected to measure just the blinding signal, as the predicted muon EDM is very close to zero. When setting the limit, a measurement of zero is assumed to give a best-case scenario and only the uncertainties are relevant.

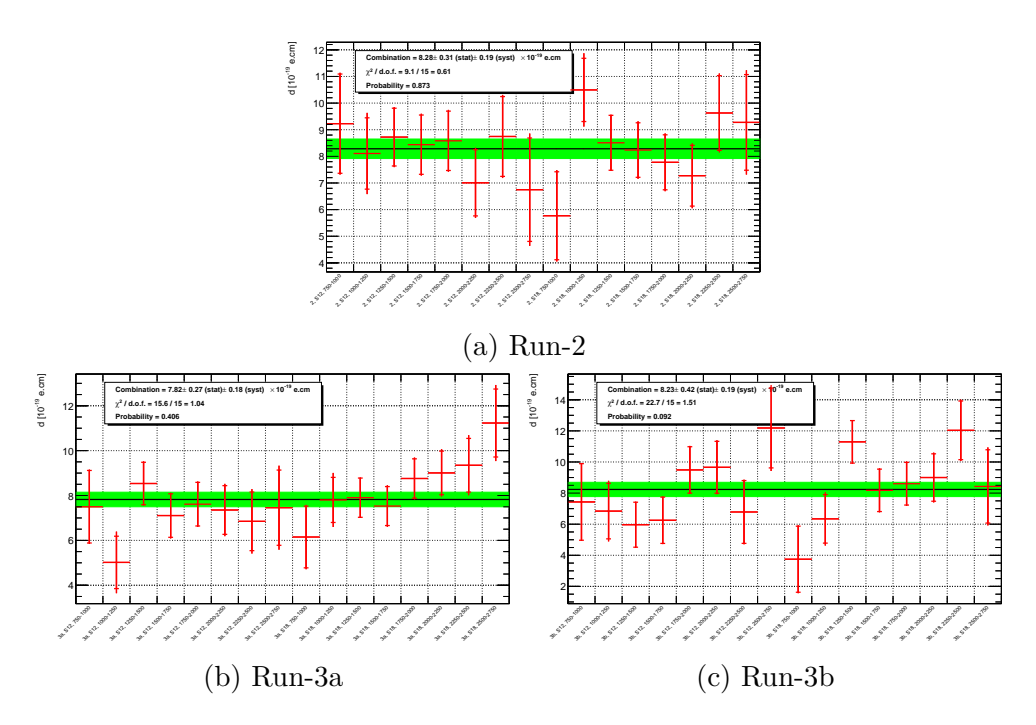


Figure 3.43: Combination using results from each Run.

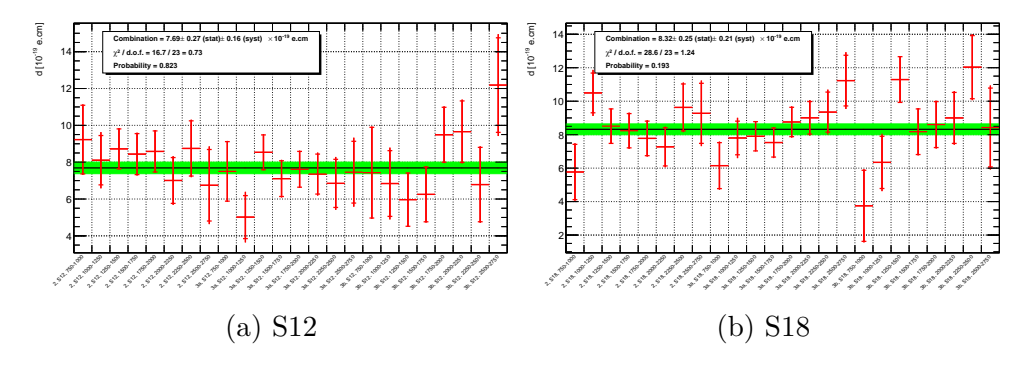


Figure 3.44: Combination using results from each station.

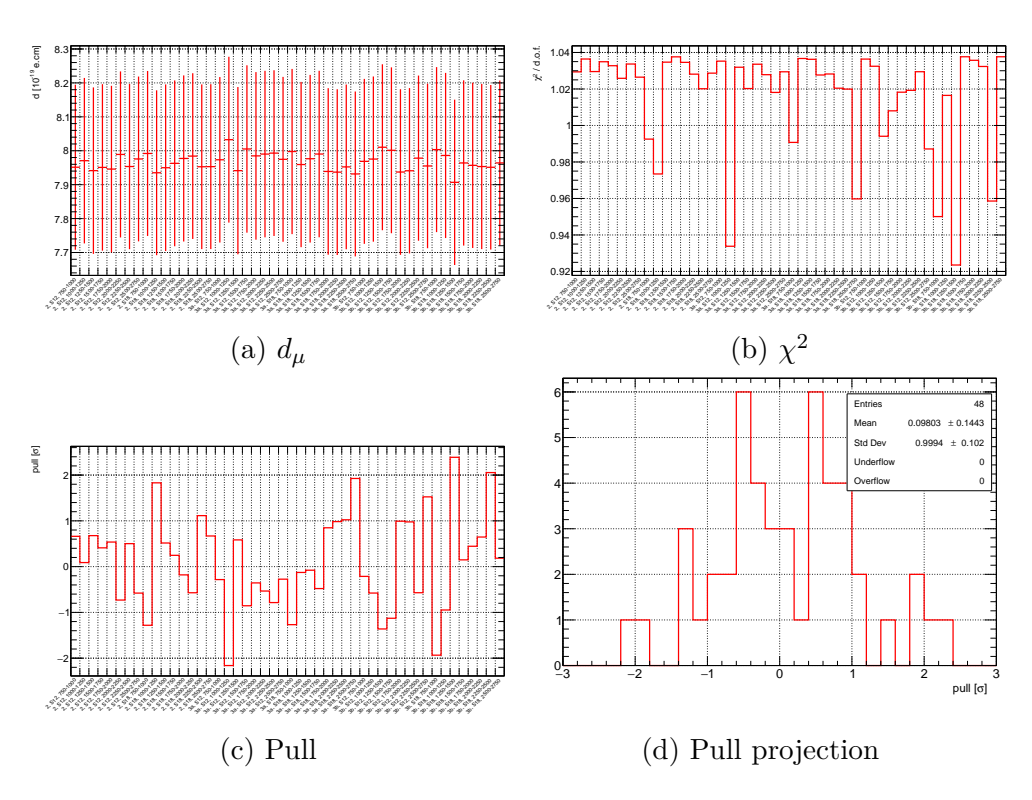


Figure 3.45: Combination checks after dropping individual results showing (a) the combined EDM value, (b) the χ^2 of the combination and (c) the pull. The x-axis is the result dropped from the fit and the final plot (d) shows the projection of the pull distribution.

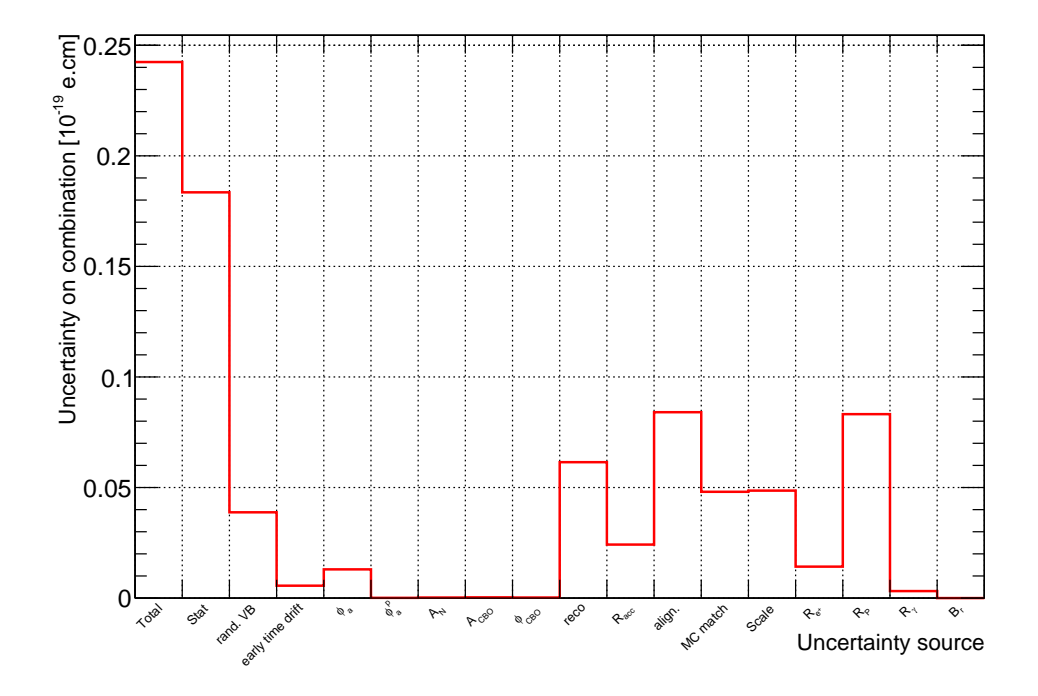


Figure 3.46: The contributions to the uncertainty on the combination from each systematic source. The total statistical uncertainties are included for comparison.

3.5 Limit setting

The final measured value has to be converted to a limit on the muon EDM via a statistical procedure. It is common practice in EDM searches to place a limit on the absolute value and, as this measurement is sensitive to the sign of the EDM, the absolute measured value $|d_{\mu}|$ will be used. Thus, the limit is set using the Feldman-Cousins (FC) method with a folded Gaussian because it produces a smooth variation between a one-sided and two-sided limit near the $|d_{\mu}|=0$ boundary. Also, it guarantees correct coverage of the probability space compared to, e.g., a one-sided Gaussian folded at zero as used at BNL [41]. FC has been used in electron EDM searches such as in [81].

FC limits must be determined numerically. For a true value of $|d_{\mu}|$, measured values X_0 are ordered by descending $R = P(X_0|d_{\mu})/P(X_0|d_{\text{best}})$. In this case, $P(X_0|d)$ is given by a folded Gaussian, and $d_{\text{best}} = X_0$ giving:

$$R = \frac{e^{-\frac{(|X_0| - |d_\mu|)^2}{2\sigma^2}} + e^{-\frac{(|X_0| + |d_\mu|)^2}{2\sigma^2}}}{1 + e^{-\frac{(2|X_0|)^2}{2\sigma^2}}}$$
(3.5.1)

Then, taking successive X_0 values, probabilities are summed from maximum to minimum R until the desired sensitivity S is reached. Therefore,

$$\int_{R_{max}}^{R} \frac{1}{\sigma\sqrt{2\pi}} \left[e^{-\frac{(|X_0|_R - |d_\mu|)^2}{2\sigma^2}} + e^{-\frac{(|X_0|_R + |d_\mu|)^2}{2\sigma^2}} \right] dR = S.$$
 (3.5.2)

The highest and lowest values of X_0 used in this sum represent the interval for this true value of d_{μ} . This is repeated for different values of d_{μ} to produce a sensitivity contour in $|d_{\mu}|$ vs $|X_0|$. For a given value of $|X_0|$, the compatible values of $|d_{\mu}|$ are determined from this contour.

Limits at both the 90% and 95% confidence level (CL) will be quoted to be consistent with current EDM limits and to provide direct comparison to the BNL muon EDM limit. The contours for 90% and 95% CLs are shown in Figure 3.47, including a comparison to two other methods.

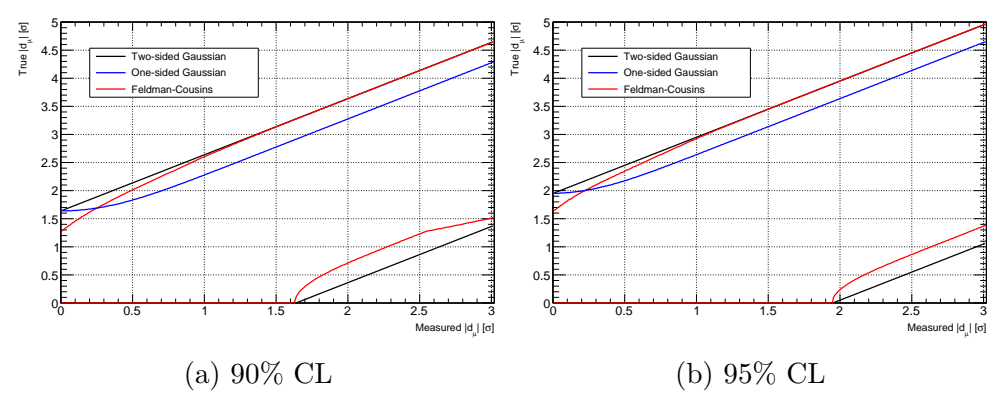


Figure 3.47: Contours showing the limits on true EDM $|d_{\mu}|$ for a given measured EDM |d| (both normalised to σ) at the (a) 90% and (b) 95% CL. Three methods are shown: FC, a one-sided Gaussian, and a two-sided Gaussian where d_{μ} can be negative.

3.6 Estimate of best sensitivity

Evidently, the strictest limit would come from a measurement of $A_{\rm EDM}=0$ mrad. To estimate the sensitivity in this case, the combined uncertainty is taken from Section 3.4 with the R-factor systematics excluded, giving a total uncertainty on d_{μ} of $0.20\times 10^{-19}~e\cdot {\rm cm}$ from the statistical and systematic uncertainties combined in quadrature.

Using the folded FC method as described in Section 3.5, a measurement of $d_{\mu} = 0 \pm 0.20 \times 10^{-19} e \cdot \text{cm}$ would lead to a limit of approximately

$$|d_{\mu}| < 0.33 \times 10^{-19} \ e \cdot \text{cm} \text{ at } 95\% \text{ CL}$$

This is a factor of ~ 5.5 improvement on the BNL limit. It should be noted that measuring $A_{\rm EDM} \equiv 0$ represents the best possible limit. At $A_{\rm EDM} \neq 0$ the limit would be less strict as shown in Figure 3.47 where the measured value of d_{μ} is on the x-axis and the limit increases as $d_{\mu} > 0$. The R-factor systematics would then be non-zero, increasing the limit further as the total uncertainty is also increased. Furthermore, the unblinding procedure will require reprocessing the fits on the unblinded data. After this, the associated uncertainties may vary slightly due to fluctuations. From MC studies, the expected variation in the measured value after blinding is on the order of 1%.

3.7 Discussion

Given an exact measurement of $d_{\mu} = 0$, the unblinded result from this analysis is expected to improve on the current muon EDM limit by ~ 5.5 times. This result is statistically limited and is on track to reach the final goal of an order of magnitude improvement after the analysis of the full dataset. Currently, the analysis is in the final stages of collaboration review and should proceed to the unblinding process soon.

Regarding the future outlook of this measurement, there are still three data taking periods from FNAL (Run-4, 5, and 6) that have yet to be analysed which contain approximately 4.8 times the statistics of Run-2/3. This alone could produce a result competitive with the indirect limit from [43] and improve on the direct limit from BNL by an order of magnitude. In addition, there is a potential improvement to the analysis method that implements a weighting of the vertical decay angles based on their probability. A similar weighting is applied in the ω_a 'A method' analysis [27] to maximise the sensitivity.

The tracking improvements set out in Section 2.3.3 have also been applied to all later datasets. As the change in QCs was slightly limited here by the MC-data agreement, a better-tuned MC could potentially allow for a small gain in tracks from additional QC adjustment. A further loosening of the QCs was well motivated based on initial investigations using data alone.

Similarly, the additional correction to the acceptance (required due to the weighting to match data as outlined in Section 3.2.7) will be greatly reduced with improvements in the MC and data agreement. Ideally, the extra scaling and the associated uncertainty could become obsolete. 3.7. Discussion 3. Analysis

With greater statistical power this will become a more significant issue if not addressed, so better beam tuning in MC will be necessary. Generally, creating further MC samples including accurate beam dynamics and varying sizes of injected EDM would be advantageous for additional cross-checks of acceptance.

Furthermore, the calculation of $R_{e^+}(\lambda)$ would benefit from MC packages that include higher order QED correction such as those in [82]. A new sample with higher statistics would improve the uncertainty and have the benefit of being an independent determination of this reduction from rest frame tilt.

A relatively simple improvement is to reconsider the treatment of the VB randomisation uncertainty. Taking the lead from the ω_a analysis, the data could be processed with a number of fixed seeds in order to find the average result. In this way, the number of seeds tested determines the error on the mean, which, although more computationally expensive, will become important as statistics increase and this uncertainty begins to dominate. The uncertainty from the randomisation is not one that vanishes as $A_{\rm EDM} \to 0$. Beyond this, the statistical gains in individual EDM fits may allow for the VB oscillation to be appropriately incorporated into the fit. This was shown to be possible in [77] but, at the time, the gains were negligible compared to the necessary work required to successfully execute the simultaneous fit.

In conclusion, the method to measure the muon EDM was established at BNL and, after further scrutiny and improvements at Fermilab, the Muon g-2 experiment will enable a world leading limit on this fundamental property. The EDM limit from the Run-2/3 analysis will improve on the current muon EDM limit by up to 5.5 times. With statistical uncertainties dominating, the analysis of the full dataset and incorporation of the suggested improvements above will facilitate a final improvement on the limit by an order of magnitude. Precision measurements continue to search for hints of new physics and guide the development of BSM theories.

Bibliography

- [1] A. D. Sakharov, "Violation of CP Invariance, C asymmetry, and baryon asymmetry of the universe", Pisma Zh. Eksp. Teor. Fiz. 5, 32–35 (1967).
- [2] A. D. Sakharov, "Violation of CP invariance, C asymmetry, and baryon asymmetry of the universe", Sov. Phys. Usp. **34**, 392 (1991).
- [3] C. S. Wu, E. Ambler, R. W. Hayward, D. D. Hoppes, and R. P. Hudson, "Experimental test of parity conservation in beta decay", Phys. Rev. **105**, 1413–1415 (1957).
- [4] J. H. Christenson, J. W. Cronin, V. L. Fitch, and R. Turlay, "Evidence for the 2π decay of the K_2^0 meson", Phys. Rev. Lett. 13, 138–140 (1964).
- [5] K. Abe et al. (Belle Collaboration), "Observation of large CP violation in the neutral B meson system", Phys. Rev. Lett. 87, 091802 (2001).
- [6] B. Aubert et al. (BABAR Collaboration), "Observation of CP violation in the B^0 meson system", Phys. Rev. Lett. 87, 091801 (2001).
- [7] K. Abe et al. (Belle Collaboration), "Observation of large CP violation in the neutral B meson system", Phys. Rev. Lett. 87, 091802 (2001).
- [8] R. Aaij et al., "Observation of CP Violation in Charm Decays", Phys. Rev. Lett. 122, 211803 (2019).
- [9] S. Navas et al. (Particle Data Group Collaboration), "Review of particle physics", Phys. Rev. D 110, 030001 (2024).
- [10] A. Hook, "TASI Lectures on the Strong CP Problem and Axions", PoS **TASI2018**, 004 (2019).
- [11] P. J. Mohr, E. Tiesinga, D. B. Newell, and B. N. Taylor, Codata Internationally Recommended 2022 Values of the Fundamental Physical Constants, Aug. 2024.
- [12] J. C. Street and E. C. Stevenson, "New evidence for the existence of a particle of mass intermediate between the proton and electron", Phys. Rev. **52**, 1003–1004 (1937).
- [13] B. Falkenburg and W. Rhode, From ultra rays to astroparticles: a historical introduction to astroparticle physics, SpringerLink: Bücher (Springer Netherlands, 2012).
- [14] P. Kunze, "Untersuchung der ultrastrahlung in der wilsonkammer", Zeitschrift für Physik 83, 1–18 (1933).

[15] B. Rossi and D. B. Hall, "Variation of the rate of decay of mesotrons with momentum", Phys. Rev. **59**, 223–228 (1941).

- [16] L. Michel, "Interaction between four half spin particles and the decay of the μ meson", Proc. Phys. Soc. A **63**, edited by T. Damour, I. Todorov, and B. Zhilinskii, 514–531 (1950).
- [17] A. Hillairet et al. (TWIST Collaboration), "Precision muon decay measurements and improved constraints on the weak interaction", Phys. Rev. D 85, 092013 (2012).
- [18] C. A. Gagliardi, R. E. Tribble, and N. J. Williams, "Global analysis of muon decay measurements", Phys. Rev. D 72, 073002 (2005).
- [19] K. Afanaciev et al. (MEG II), "A search for $\mu^+ \to e^+ \gamma$ with the first dataset of the MEG II experiment", Eur. Phys. J. C 84, [Erratum: Eur.Phys.J.C 84, 1042 (2024)], 216 (2024).
- [20] G. Hesketh, S. Hughes, A.-K. Perrevoort, and N. Rompotis, "The Mu3e Experiment", in Proceedings of the US Community Study on the Future of Particle Physics (Snowmass 2021) (2022).
- [21] R. H. Bernstein (Mu2e), "The Mu2e Experiment", Frontiers in Physics 7, 1 (2019).
- [22] R. Abramishvili et al., "Comet phase-i technical design report", Progress of Theoretical and Experimental Physics **2020**, 10.1093/ptep/ptz125 (2020).
- [23] P. A. M. Dirac, "The quantum theory of the electron. part II", Proc. R. Soc. Lond. A 118, 351–361 (1928).
- [24] P. Kusch and H. M. Foley, "The magnetic moment of the electron", Phys. Rev. **74**, 250–263 (1948).
- [25] J. Schwinger, "On quantum-electrodynamics and the magnetic moment of the electron", Phys. Rev. **73**, 416–417 (1948).
- [26] X. Fan, T. G. Myers, B. A. D. Sukra, and G. Gabrielse, "Measurement of the electron magnetic moment", Phys. Rev. Lett. 130, 071801 (2023).
- [27] D. P. Aguillard et al. (Muon g-2 Collaboration), "Detailed report on the measurement of the positive muon anomalous magnetic moment to 0.20 ppm", Phys. Rev. D **110**, 032009 (2024).
- [28] F. J. M. Farley and E. Picasso, "The Muon (g-2) Experiments at CERN", Ann. Rev. Nucl. Part. Sci. **29**, 243–282 (1979).
- [29] F. Combley, F. J. M. Farley, and E. Picasso, "The CERN Muon (g-2) Experiments", Phys. Rept. **68**, 93 (1981).
- [30] G. W. Bennett et al. (Muon g-2 Collaboration), "Final report of the E821 muon anomalous magnetic moment measurement at BNL", Phys. Rev. D **73**, 072003 (2006).
- [31] B. Abi et al. (Muon g-2 Collaboration), "Measurement of the positive muon anomalous magnetic moment to 0.46 ppm", Phys. Rev. Lett. **126**, 141801 (2021).
- [32] T. Aoyama et al., "The anomalous magnetic moment of the muon in the Standard Model", Physics Reports 887, 1–166 (2020).

[33] D. Aguillard et al., "Measurement of the positive muon anomalous magnetic moment to 0.20 ppm", Phys. Rev. Lett. **131**, 161802 (2023).

- [34] F. V. Ignatov et al. (CMD-3 Collaboration), "Measurement of the $e^+e^- \to \pi^+\pi^-$ cross section from threshold to 1.2 GeV with the CMD-3 detector", Phys. Rev. D **109**, 112002 (2024).
- [35] A. Boccaletti et al., "High precision calculation of the hadronic vacuum polarisation contribution to the muon anomaly", (2024).
- [36] J. L. Feng, K. T. Matchev, and Y. Shadmi, "Theoretical expectations for the muons electric dipole moment", Nuclear Physics B 613, 366–381 (2001).
- [37] D. Ghosh and R. Sato, "Lepton electric dipole moment and strong CP violation", Physics Letters B 777, 335–339 (2018).
- [38] Y. Yamaguchi and N. Yamanaka, "Large long-distance contributions to the electric dipole moments of charged leptons in the Standard Model", Phys. Rev. Lett. **125**, 241802 (2020).
- [39] M. Pospelov and A. Ritz, "CKM benchmarks for electron electric dipole moment experiments", Phys. Rev. D 89, 056006 (2014).
- [40] J. Bailey et al., "New limits on the electric dipole moment of positive and negative muons", Journal of Physics G: Nuclear Physics 4, 345 (1978).
- [41] G. W. Bennett et al. (Muon g-2 Collaboration), "Improved limit on the muon electric dipole moment", Phys. Rev. D **80**, 052008 (2009).
- [42] T. S. Roussy et al., "An improved bound on the electrons electric dipole moment", Science **381**, 46–50 (2023).
- [43] Y. Ema, T. Gao, and M. Pospelov, "Improved indirect limits on muon electric dipole moment", Phys. Rev. Lett. **128**, 131803 (2022).
- [44] R. Aaij et al., "Test of lepton universality in beauty-quark decays", Nature Physics 18, 277–282 (2022).
- [45] R. Aaij et al. (LHCb Collaboration), "Measurement of the $\Lambda_b^0 \to \Lambda(1520)\mu^+\mu^-$ differential branching fraction", Phys. Rev. Lett. **131**, 151801 (2023).
- [46] R. Aaij et al. (LHCb Collaboration), "Test of lepton universality in $b \to s \ell^+ \ell^-$ decays", Phys. Rev. Lett. **131**, 051803 (2023).
- [47] G. Isidori and D. M. Straub, "Minimal flavour violation and beyond", The European Physical Journal C 72, 2103 (2012).
- [48] V. Cirigliano, B. Grinstein, G. Isidori, and M. B. Wise, "Minimal flavor violation in the lepton sector", Nuclear Physics B **728**, 121–134 (2005).
- [49] P. Fileviez Pérez and A. D. Plascencia, "Theory of Dirac dark matter: Higgs boson decays and EDMs", Phys. Rev. D 105, 095021 (2022).

[50] K. S. Khaw, Y. Nakai, R. Sato, Y. Shigekami, and Z. Zhang, "A large muon EDM from dark matter", Journal of High Energy Physics 2023, 234 (2023).

- [51] S. Kraml, "CP violation in SUSY", in 15th International Conference on Supersymmetry and the Unification of Fundamental Interactions (SUSY07) (Oct. 2007), pp. 132–139.
- [52] R. Barbieri, P. Lodone, and D. M. Straub, "CP violation in supersymmetry with Effective Minimal Flavour Violation", Journal of High Energy Physics **2011**, 049 (2011).
- [53] A. J. Roy and M. Bander, "Magnetic and electric dipole constraints on extra dimensions and magnetic fluxes", Nuclear Physics B 811, 353–362 (2009).
- [54] W. Dekens, J. de Vries, M. Jung, and K. K. Vos, "The phenomenology of electric dipole moments in models of scalar leptoquarks", Journal of High Energy Physics **2019**, 069 (2019).
- [55] J. Bailey et al. (CERN-Mainz-Daresbury), "Final report on the CERN muon storage ring including the anomalous magnetic moment and the electric dipole moment of the muon, and a direct test of relativistic time dilation", Nucl. Phys. B **150**, 1–75 (1979).
- [56] L. H. Thomas, "The motion of a spinning electron", Nature 117, 514 (1926).
- [57] L. Thomas, "The kinematics of an electron with an axis", The London, Edinburgh, and Dublin Philosophical Magazine and Journal of Science 3, 1–22 (1927).
- [58] V. Bargmann, L. Michel, and V. L. Telegdi, "Precession of the polarization of particles moving in a homogeneous electromagnetic field", Phys. Rev. Lett. **2**, 435–436 (1959).
- [59] T. Fukuyama and A. J. Silenko, "Derivation of generalised Thomas–Bargmann–Michel–Telegdi equation for a particle with electric dipole moment", International Journal of Modern Physics A 28, 1350147 (2013).
- [60] J. Grange et al., Muon (g-2) technical design report, 2018.
- [61] D. Stratakis et al., "Accelerator performance analysis of the fermilab muon campus", Phys. Rev. Accel. Beams **20**, 111003 (2017).
- [62] E. Commins and P. Bucksbaum, Weak interactions of leptons and quarks (Cambridge University Press, 1983).
- [63] S. Grant, "Towards a search for the electric dipole moment of the muon at the Fermilab Muon g-2 experiment", PhD thesis (University College London, 2022).
- [64] R. E. Behrends, R. J. Finkelstein, and A. Sirlin, "Radiative corrections to decay processes", Phys. Rev. **101**, 866–873 (1956).
- [65] T. Kinoshita and A. Sirlin, "Muon decay with parity nonconserving interactions and radiative corrections in the two-component theory", Phys. Rev. **107**, 593–599 (1957).

[66] A. Arbuzov, "First-order radiative corrections to polarized muon decay spectrum", Physics Letters B **524**, 99–106 (2002).

- [67] C. Patrignani, Particle Data Group, et al., "Review of Particle Physics", Chinese Physics C 40, 100001, 100001 (2016).
- [68] J. Kaspar et al., "Design and performance of SiPM-based readout of PbF₂ crystals for high-rate, precision timing applications", JINST 12, P01009 (2017).
- [69] K. S. Khaw et al. (Muon g-2), "Performance of the Muon g-2 calorimeter and readout systems measured with test beam data", Nucl. Instrum. Meth. A **945**, 162558 (2019).
- [70] MidasWiki, (2023) https://daq00.triumf.ca/MidasWiki/ index.php/Main_Page (visited on 03/17/2025).
- [71] P. Girotti, "Small experiment, Big Data: the data production of the Muon g-2 Experiment", in Proceedings of 41st international conference on high energy physics, Vol. 414 (2022), p. 228.
- [72] B. King et al., "The straw tracking detector for the fermilab muon g-2 experiment", Journal of Instrumentation 17, P02035 (2022).
- [73] G. Sweetmore, "Measurement of the muon spin precession frequency using the straw tracking detectors at the Fermilab Muon g-2 experiment", PhD thesis (University of Manchester, 2023).
- [74] J. Allison et al., "Recent developments in Geant4", Nuclear Instruments and Methods in Physics Research Section A: Accelerators, Spectrometers, Detectors and Associated Equipment 835, 186–225 (2016).
- [75] G. Lukicov, "Alignment of the straw tracking detectors for the Fermilab Muon g-2 experiment and systematic studies for a muon electric dipole moment measurement", PhD thesis (University College London, 2020).
- [76] S. Charity, "Beam profile measurements using the straw tracking detectors at the Fermilab Muon g-2 experiment, and a study of their sensitivity to a muon electric dipole moment", PhD thesis (University of Liverpool, 2018).
- [77] D. Vasilkova, "Searching for a muon electric dipole moment with the straw trackers at the Fermilab Muon g-2 experiment", PhD thesis (University College London, 2023).
- [78] R. Brun and F. Rademakers, "ROOT An Object Oriented Data Analysis Framework", Nucl. Inst. & Meth. in Phys. Res. A **389**, edited by M. Werlen and D. Perret-Gallix, See also "ROOT" [software], Release v6.12/04, 81–86 (1997).
- [79] M. Matsumoto and T. Nishimura, "Mersenne twister: a 623-dimensionally equidistributed uniform pseudo-random number generator", ACM Trans. Model. Comput. Simul. 8, 3–30 (1998).
- [80] L. Lyons, D. Gibaut, and P. Clifford, "How to combine correlated estimates of a single physical quantity", Nucl. Instrum. Meth. A **270**, 110 (1988).

[81] J. Baron et al., "Methods, analysis, and the treatment of systematic errors for the electron electric dipole moment search in thorium monoxide", New Journal of Physics 19, 073029 (2017).

[82] P. Banerjee, T. Engel, A. Signer, and Y. Ulrich, "QED at NNLO with McMule", SciPost Physics 9, 027 (2020).

Appendices

Appendix A

Example results from beam scraping fit and correction

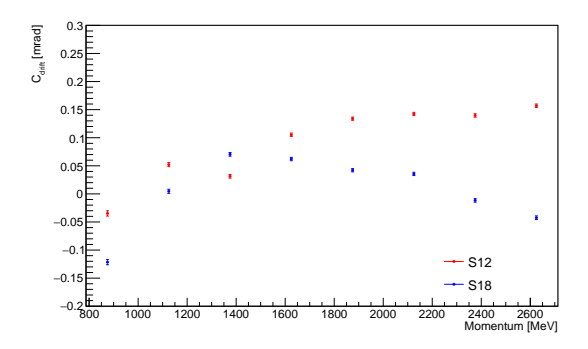


Figure A.1: C_{drift} for the exponential fit to the beam scraping effect on 3N for both stations.

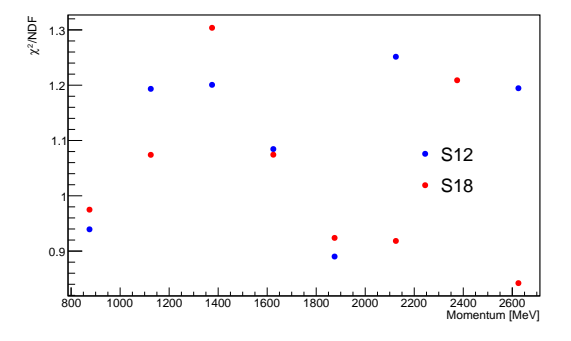


Figure A.2: χ^2/NDF for the exponential fit to the beam scraping effect on 3N for both stations.

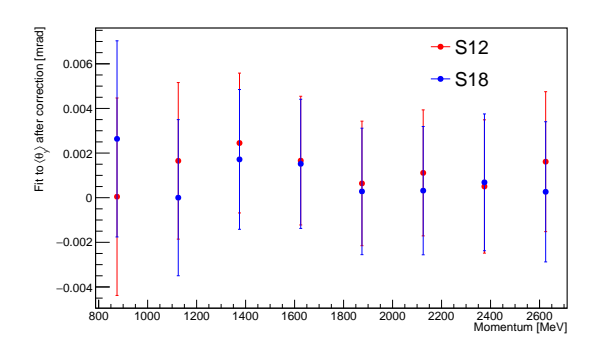


Figure A.3: Constant from the straight line fit after the beam scraping correction to 3N for both stations. A discussion of a potential reason for the systematic shift from zero is given in Section 3.1.4.

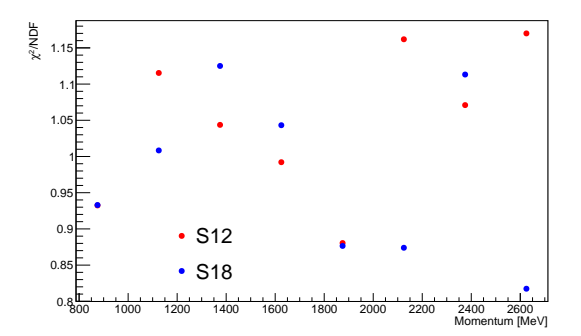


Figure A.4: χ^2/NDF for the straight line fit after the beam scraping correction to 3N for both stations.

Appendix B

All fit start-time scan plots

The fit start-time scan plots for each dataset, station, and momentum bin for the average vertical angle fit floating parameters $A_{\rm EDM}$, A_{g-2} and C.

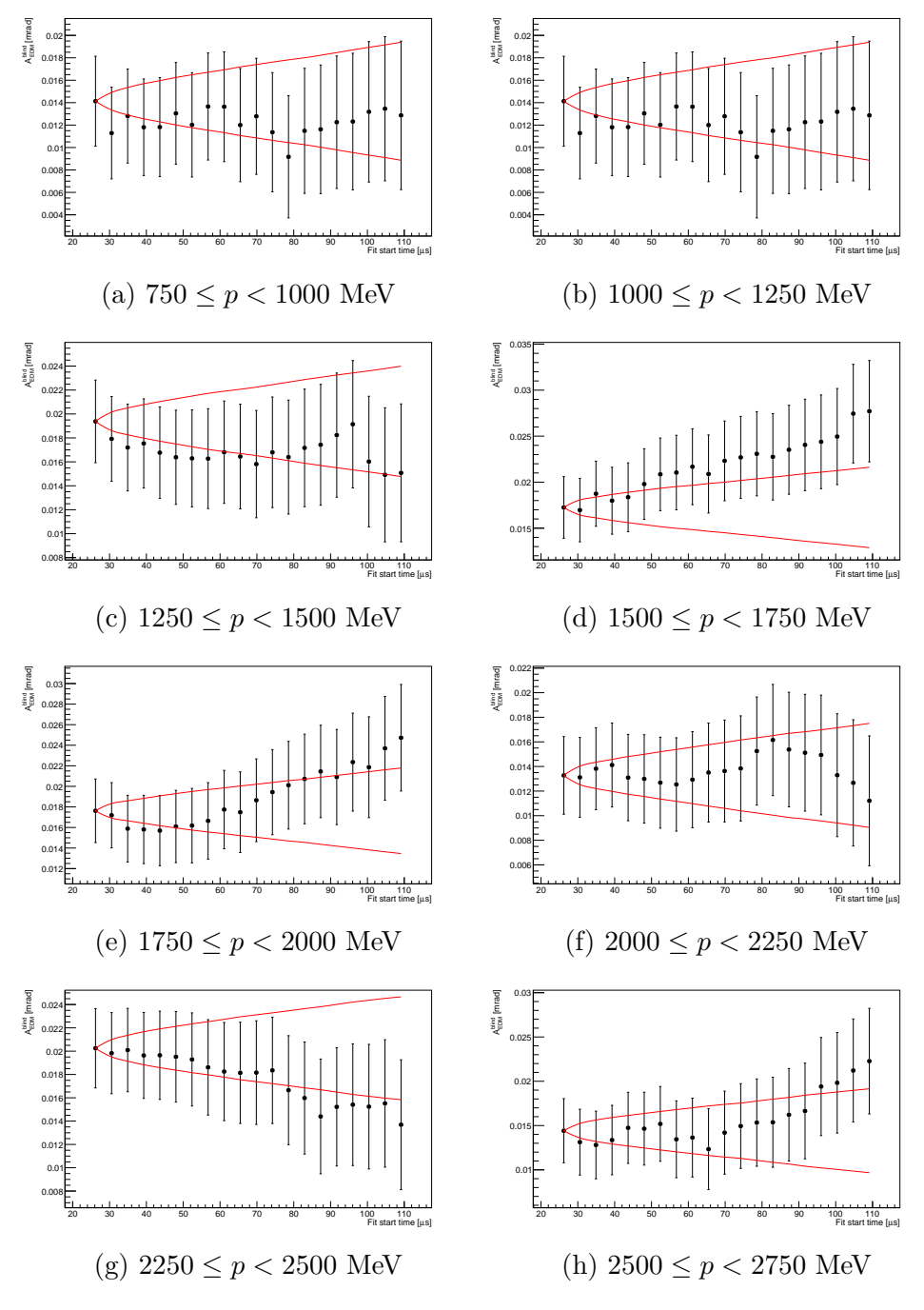


Figure B.1: Fit start time scans for Run-2 S12 fit parameter $A_{\rm EDM}$, the red line indicates the 1σ allowed variation.

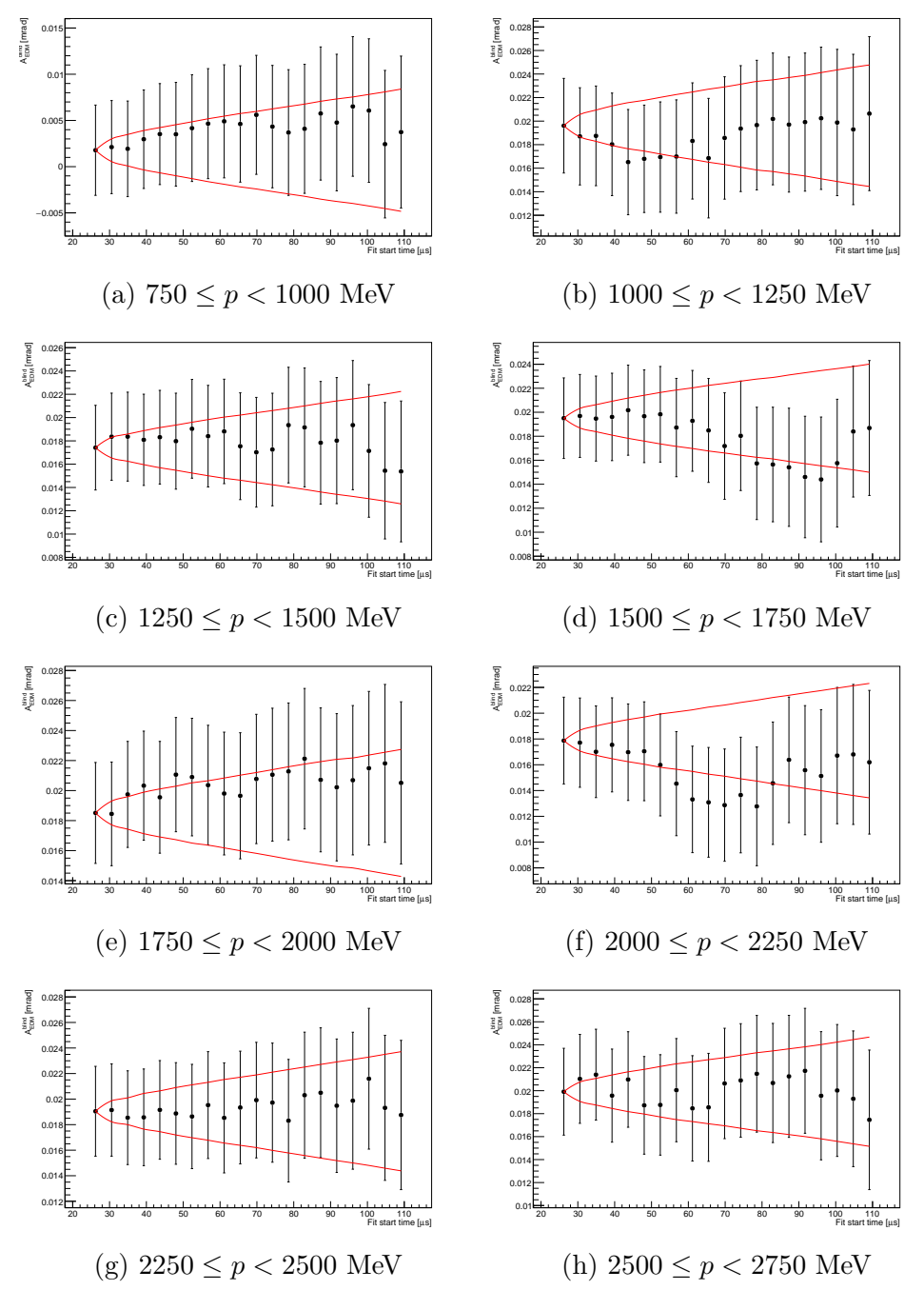


Figure B.2: Fit start time scans for Run-2 S18 fit parameter $A_{\rm EDM}$, the red line indicates the 1σ allowed variation.

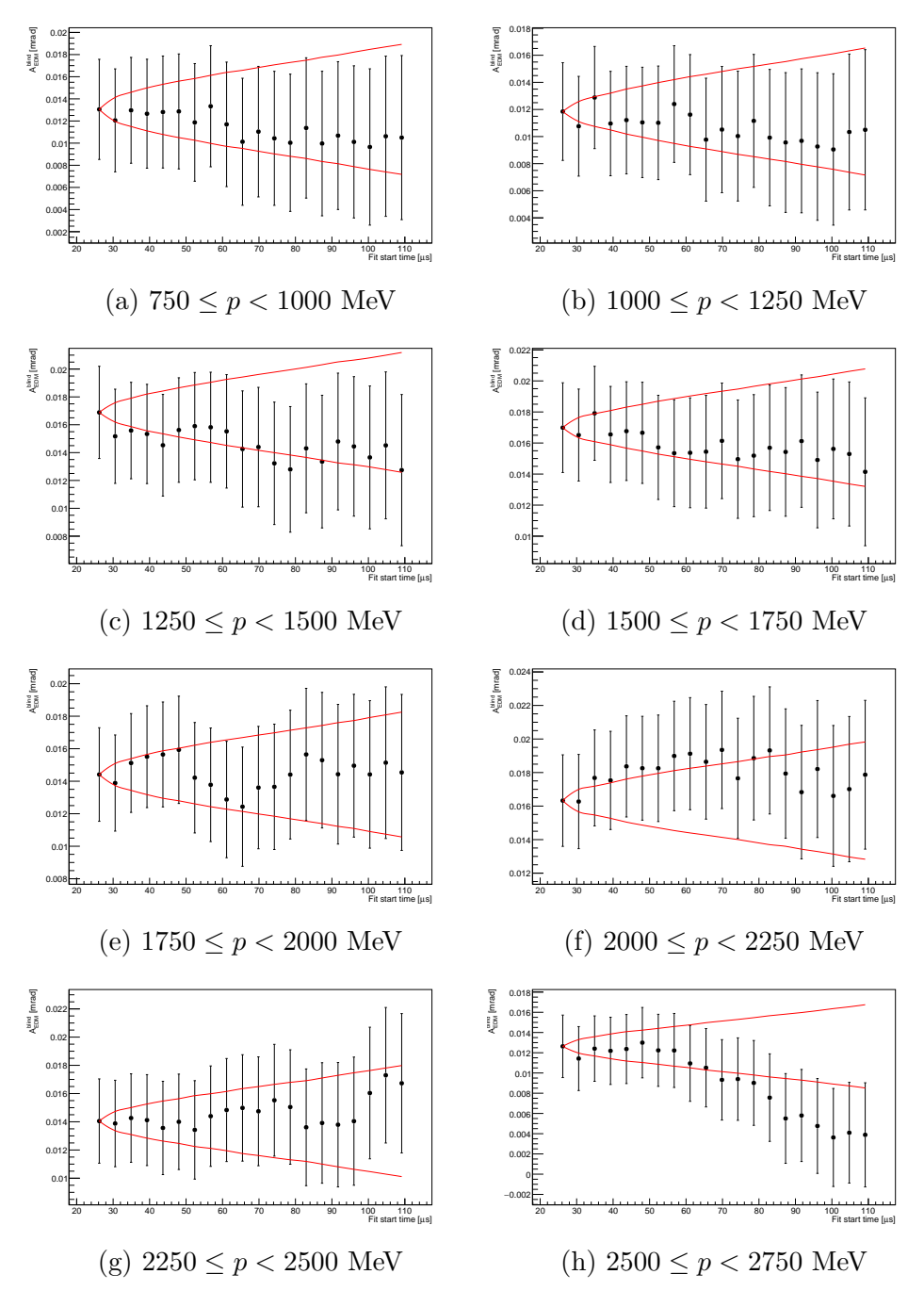


Figure B.3: Fit start time scans for Run-3a S12 fit parameter $A_{\rm EDM}$, the red line indicates the 1σ allowed variation.

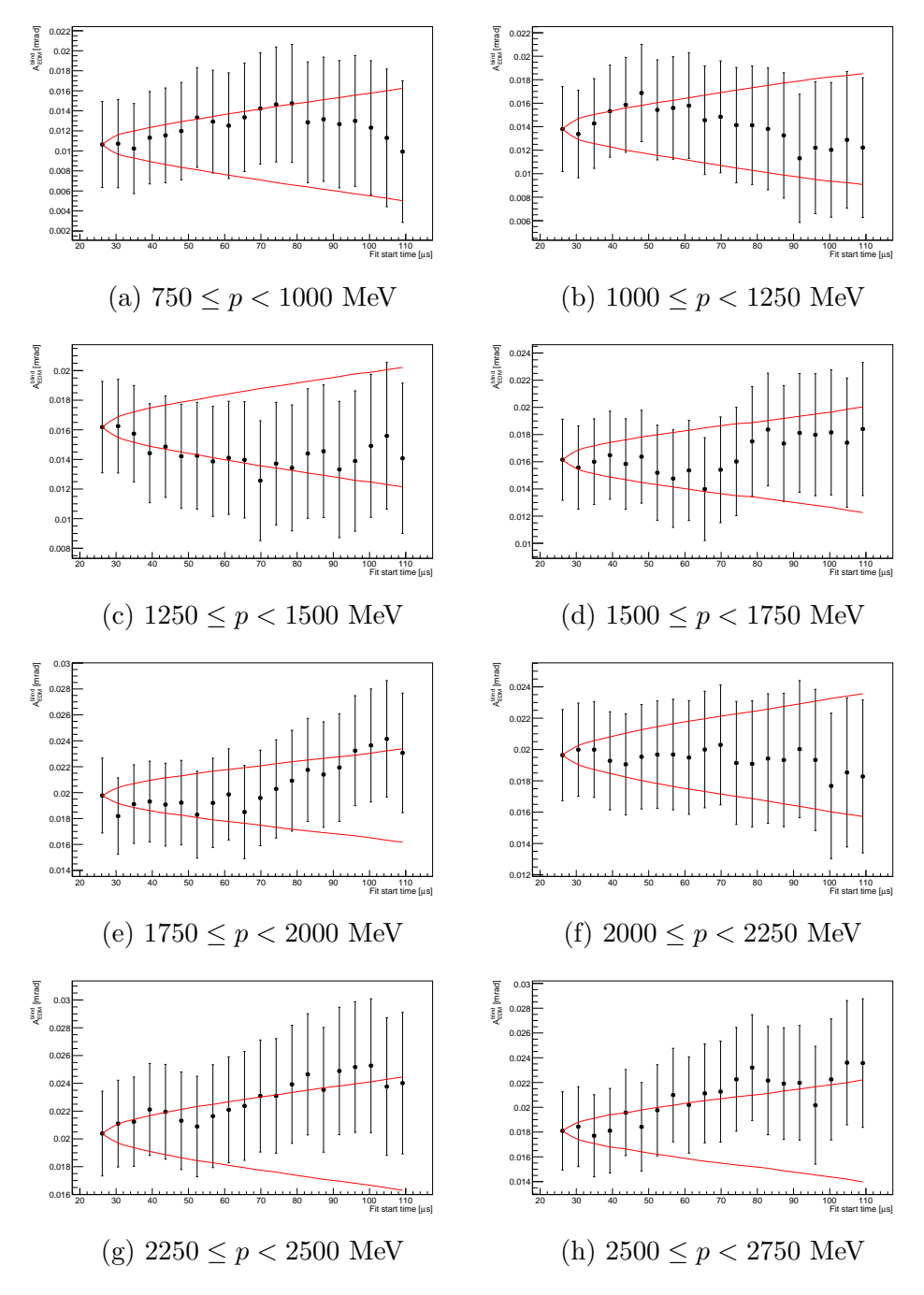


Figure B.4: Fit start time scans for Run-3a S18 fit parameter $A_{\rm EDM}$, the red line indicates the 1σ allowed variation.

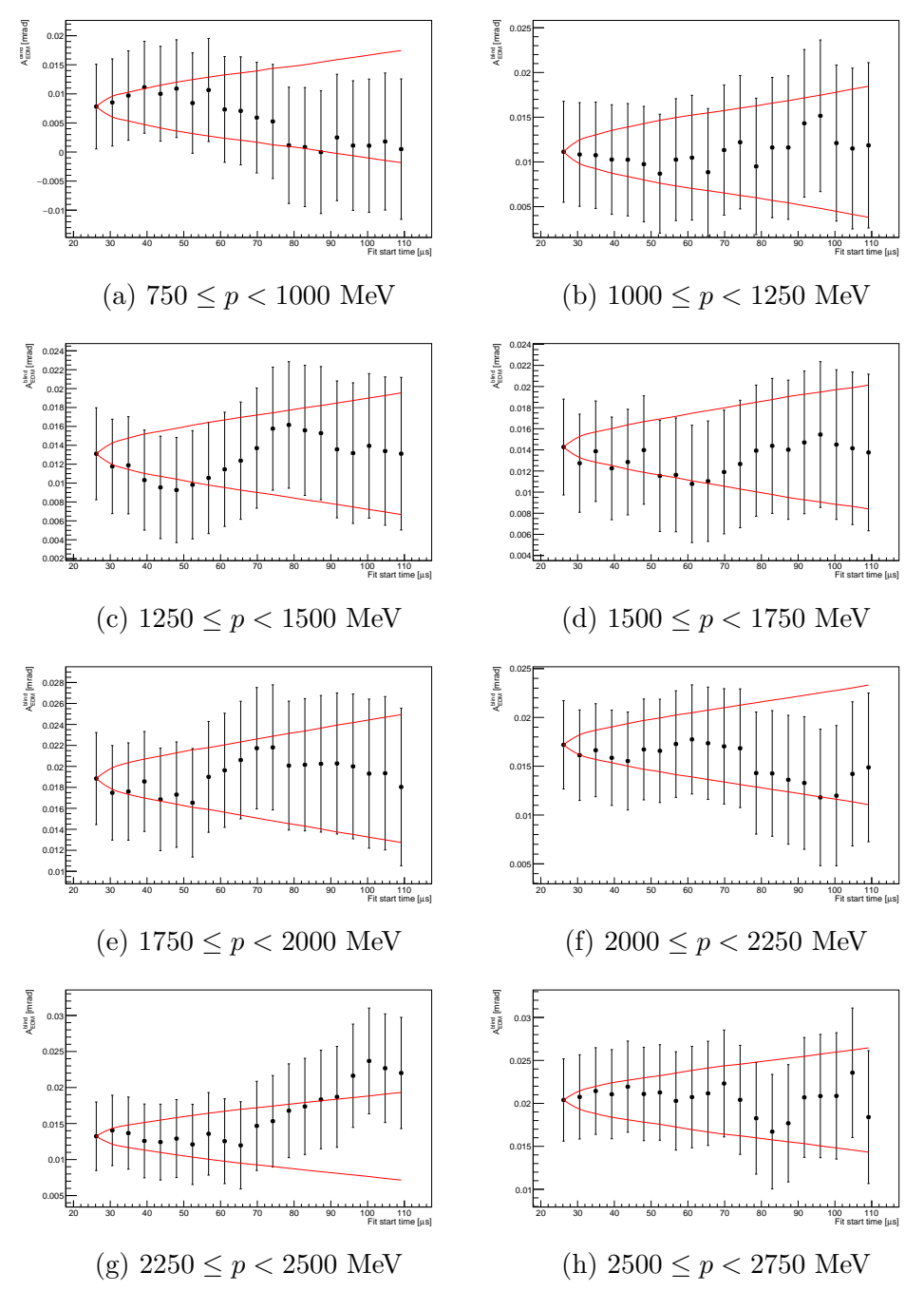


Figure B.5: Fit start time scans for Run-3b S12 fit parameter $A_{\rm EDM}$, the red line indicates the 1σ allowed variation.

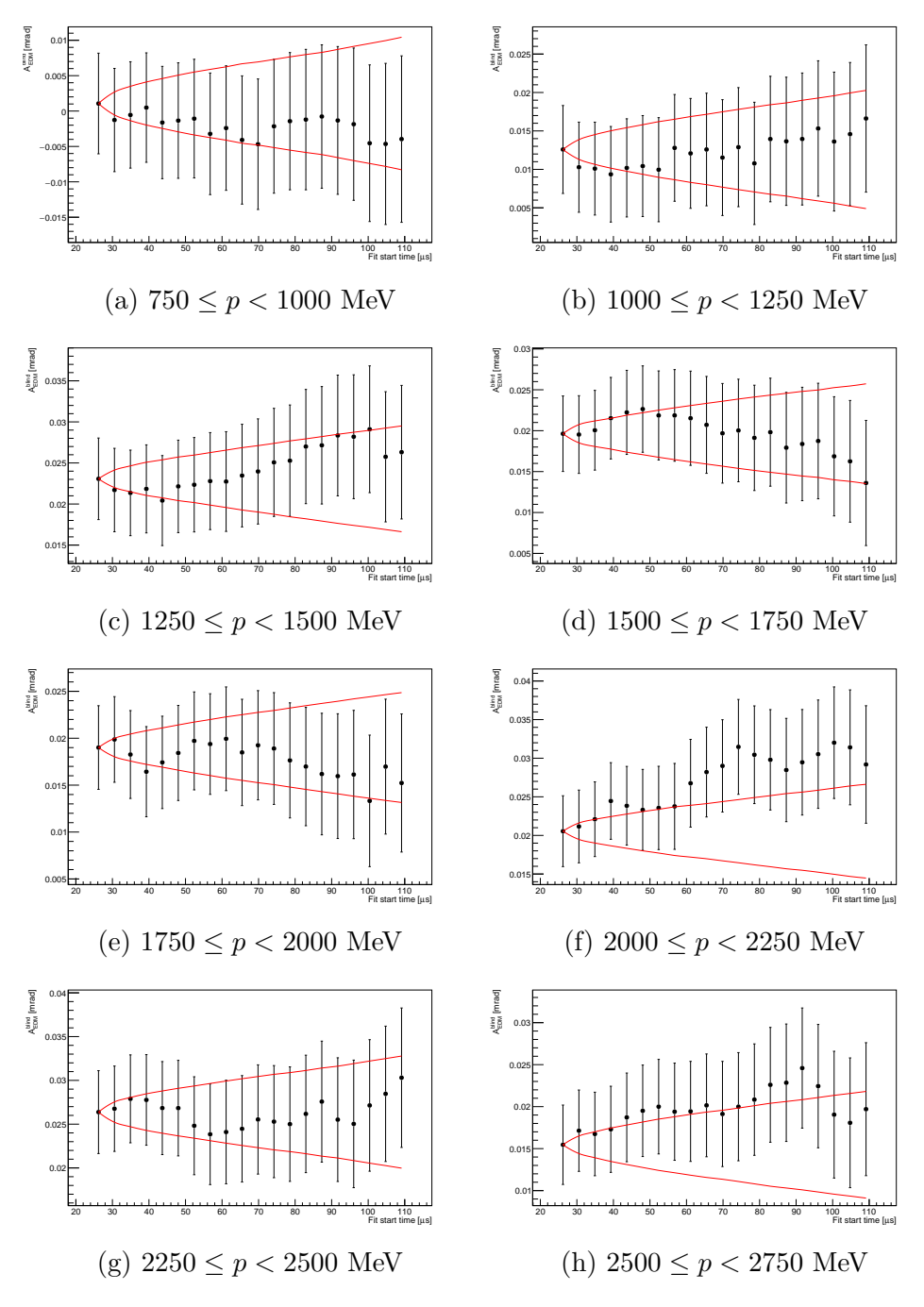


Figure B.6: Fit start time scans for Run-3b S18 fit parameter $A_{\rm EDM}$, the red line indicates the 1σ allowed variation.

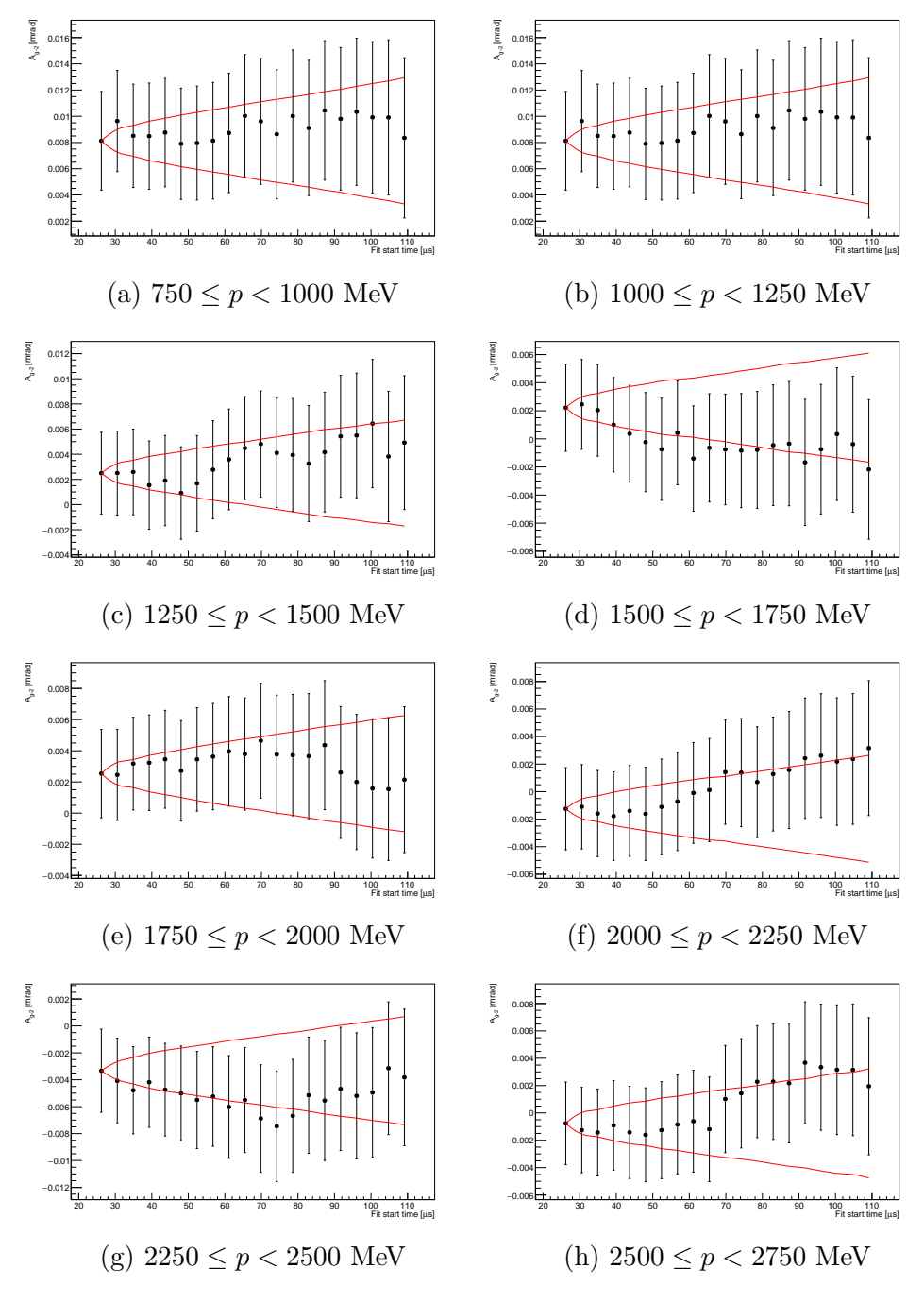


Figure B.7: Fit start time scans for Run-2 S12 fit parameter A_{g-2} , the red line indicates the 1σ allowed variation.

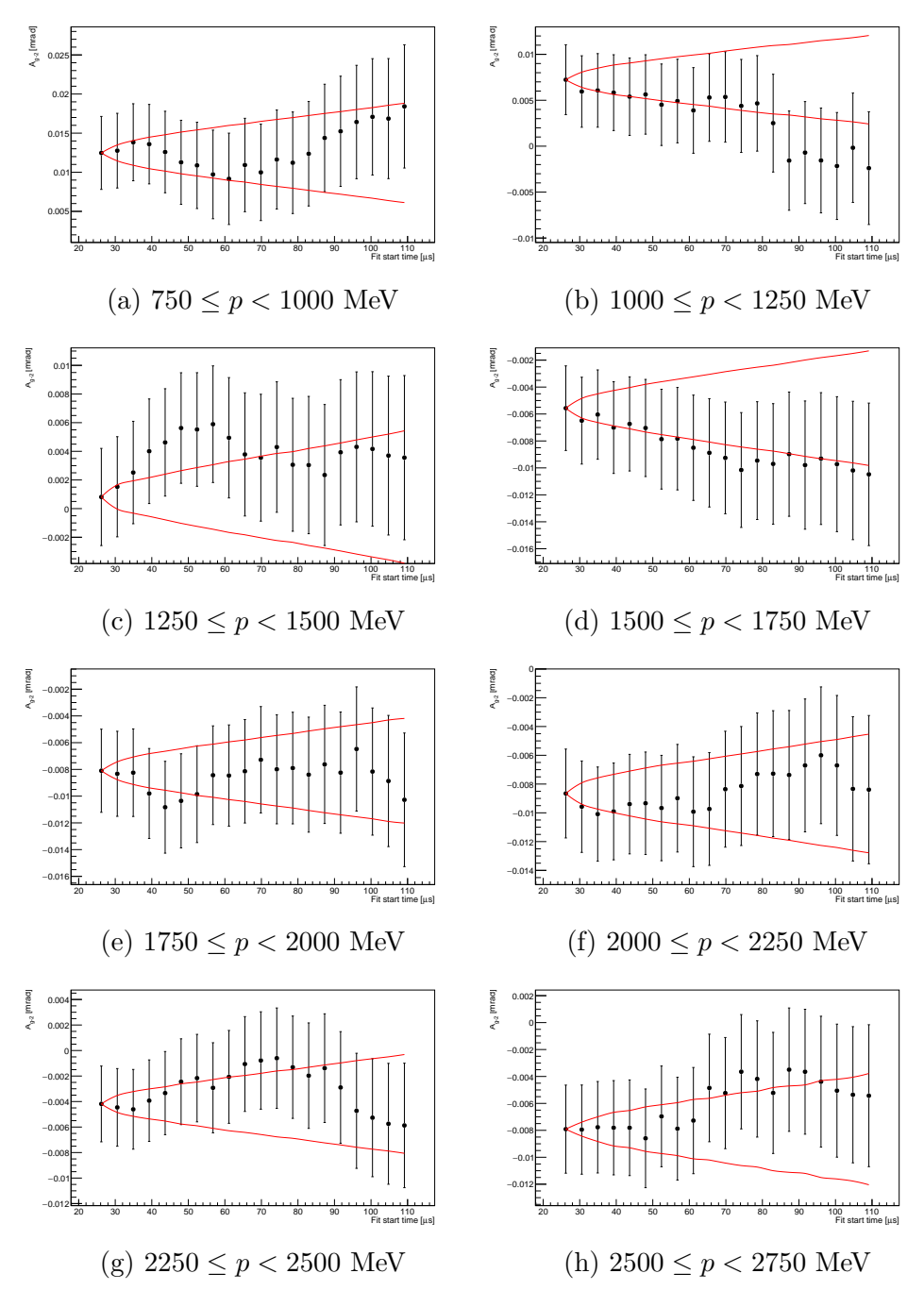


Figure B.8: Fit start time scans for Run-2 S18 fit parameter A_{g-2} , the red line indicates the 1σ allowed variation.

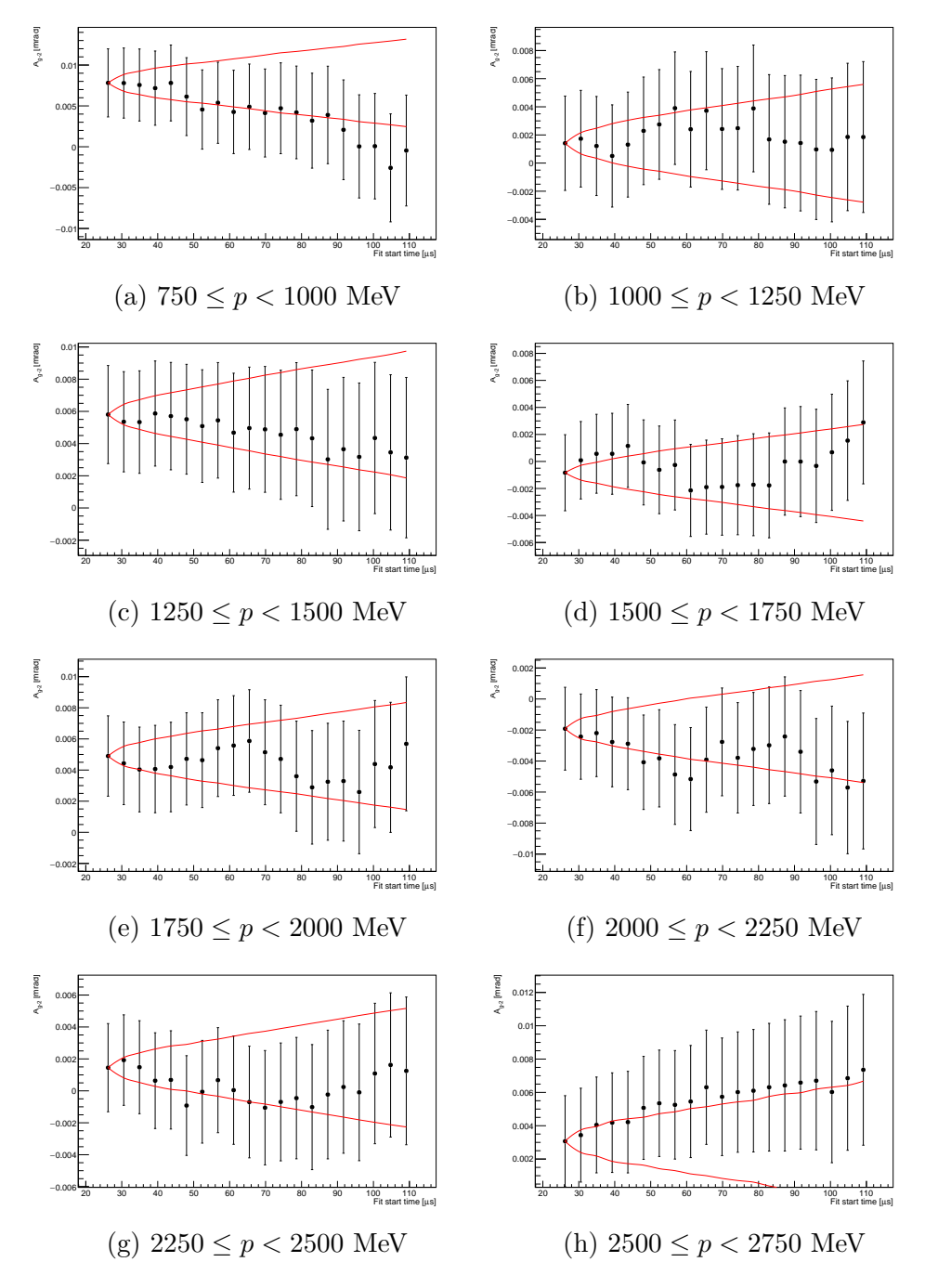


Figure B.9: Fit start time scans for Run-3a S12 fit parameter A_{g-2} , the red line indicates the 1σ allowed variation.

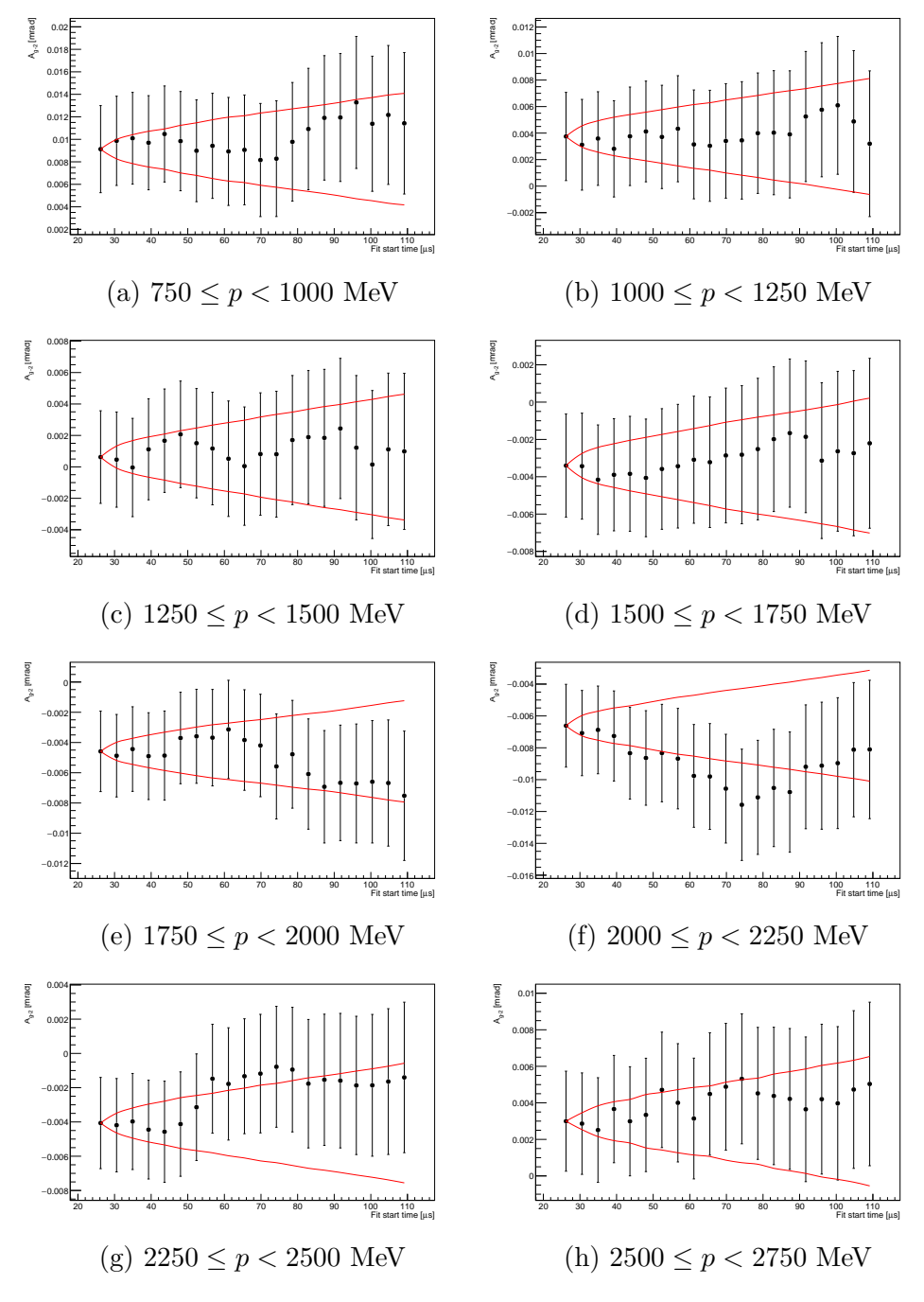


Figure B.10: Fit start time scans for Run-3a S18 fit parameter A_{g-2} , the red line indicates the 1σ allowed variation.

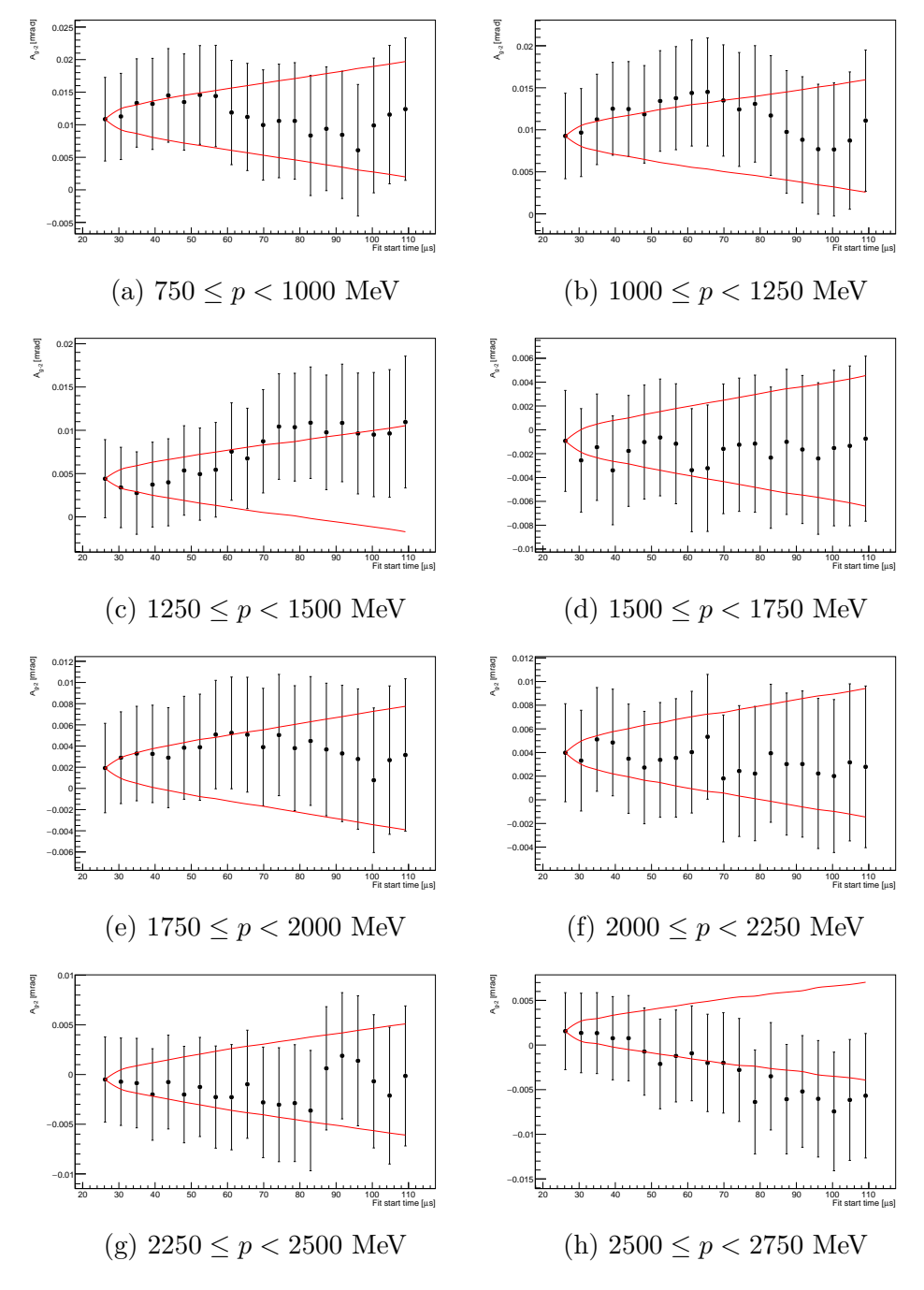


Figure B.11: Fit start time scans for Run-3b S12 fit parameter A_{g-2} , the red line indicates the 1σ allowed variation.

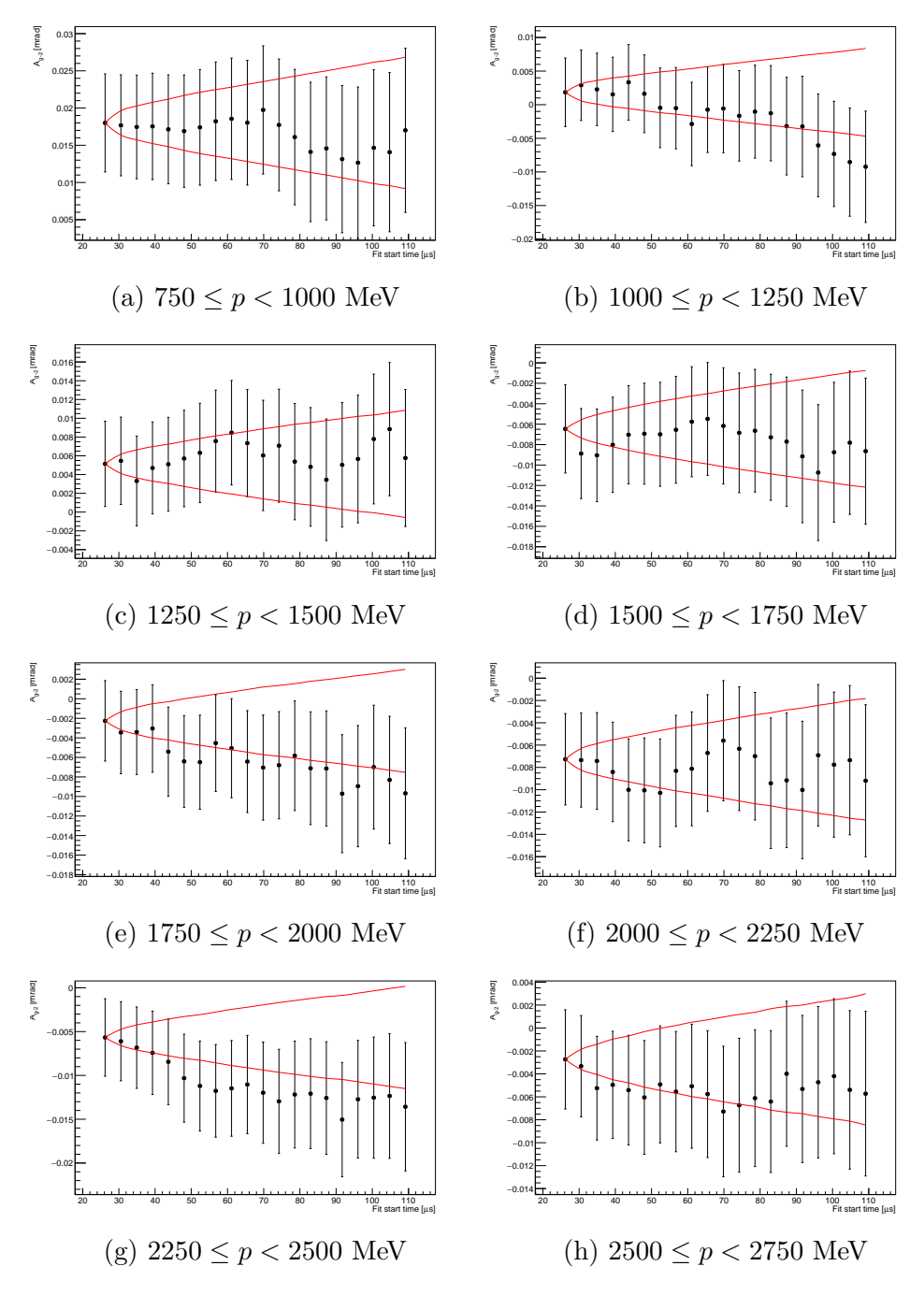


Figure B.12: Fit start time scans for Run-3b S18 fit parameter A_{g-2} , the red line indicates the 1σ allowed variation.

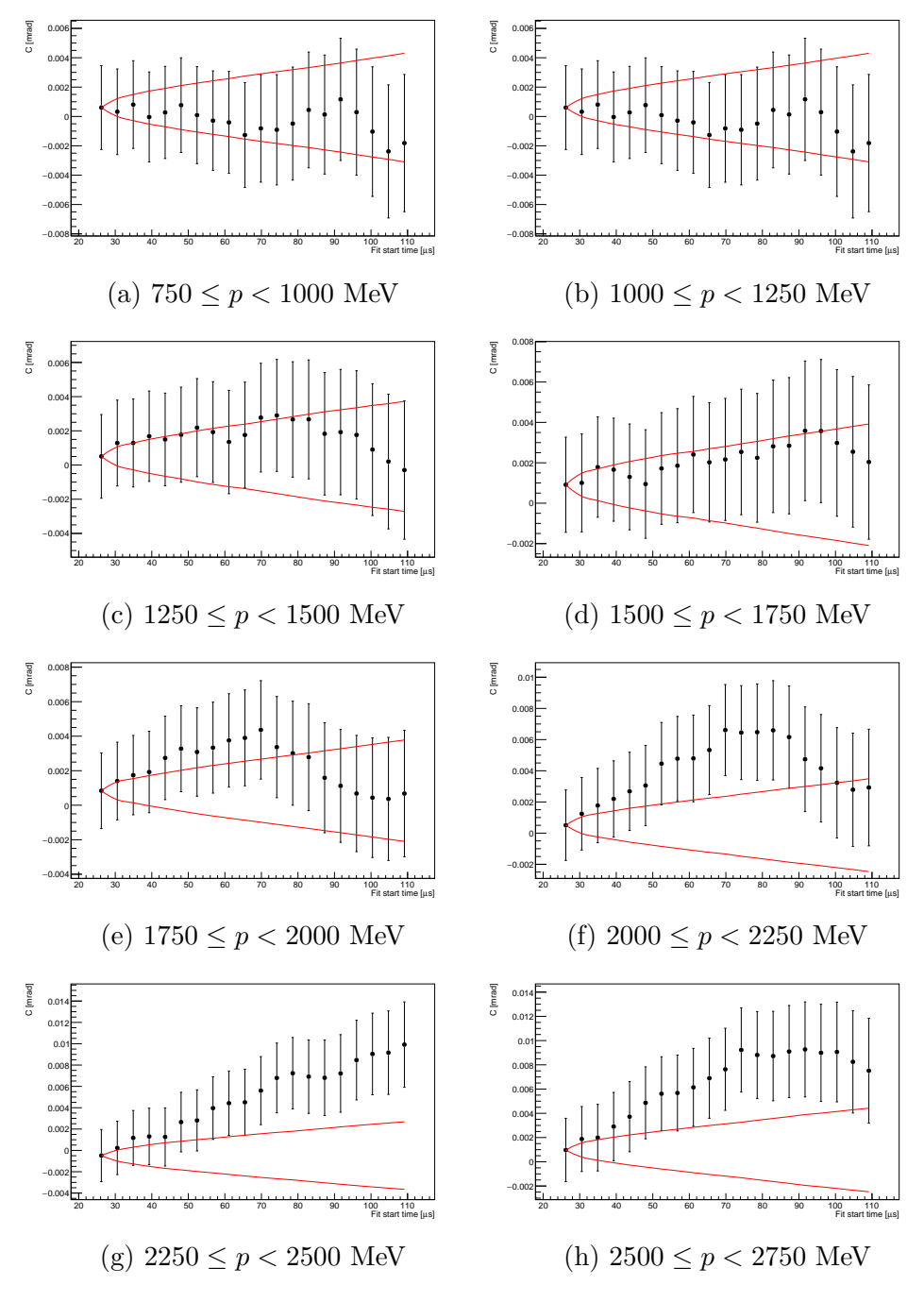


Figure B.13: Fit start time scans for Run-2 S12 fit parameter C, the red line indicates the 1σ allowed variation.

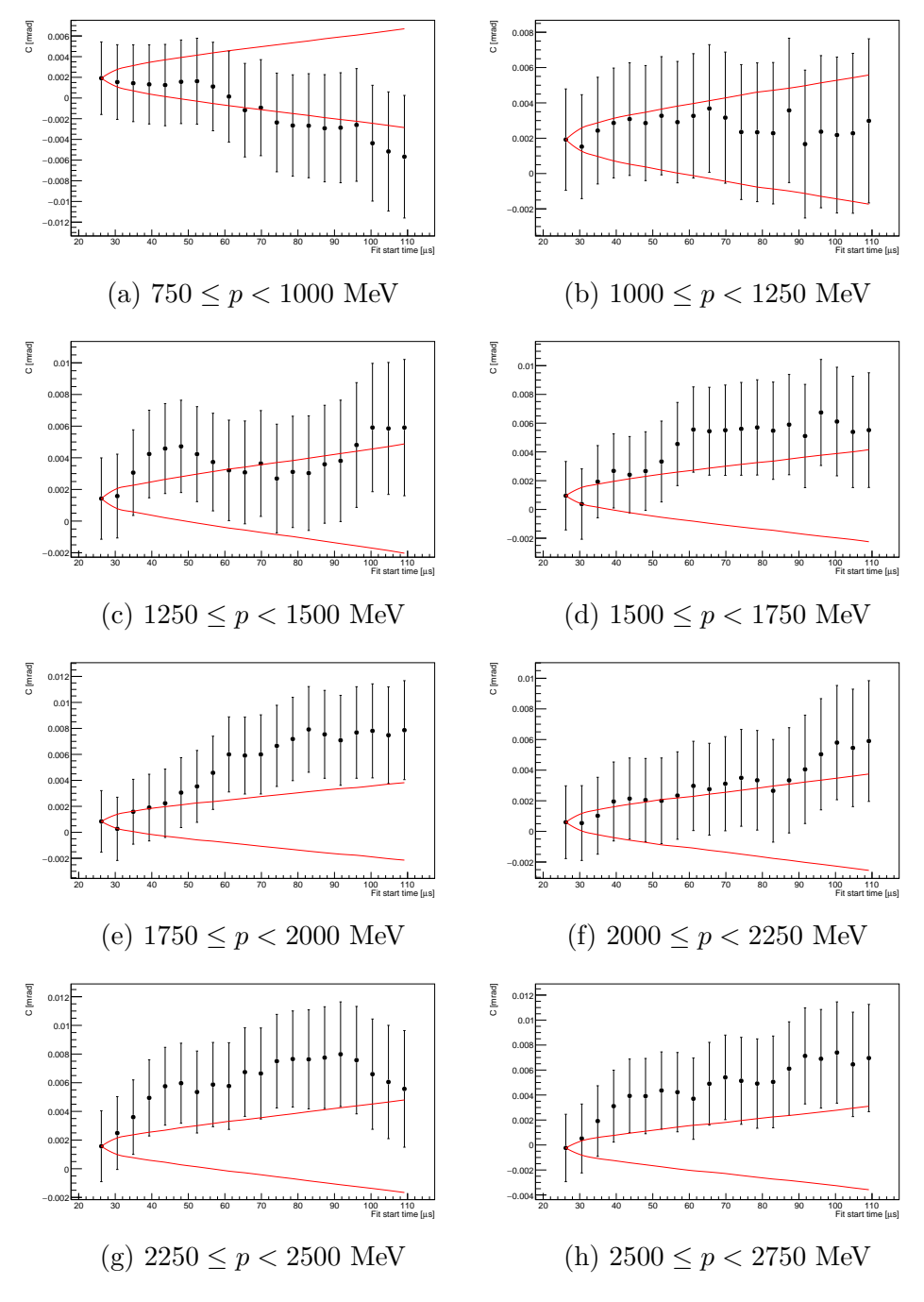


Figure B.14: Fit start time scans for Run-2 S18 fit parameter C, the red line indicates the 1σ allowed variation.

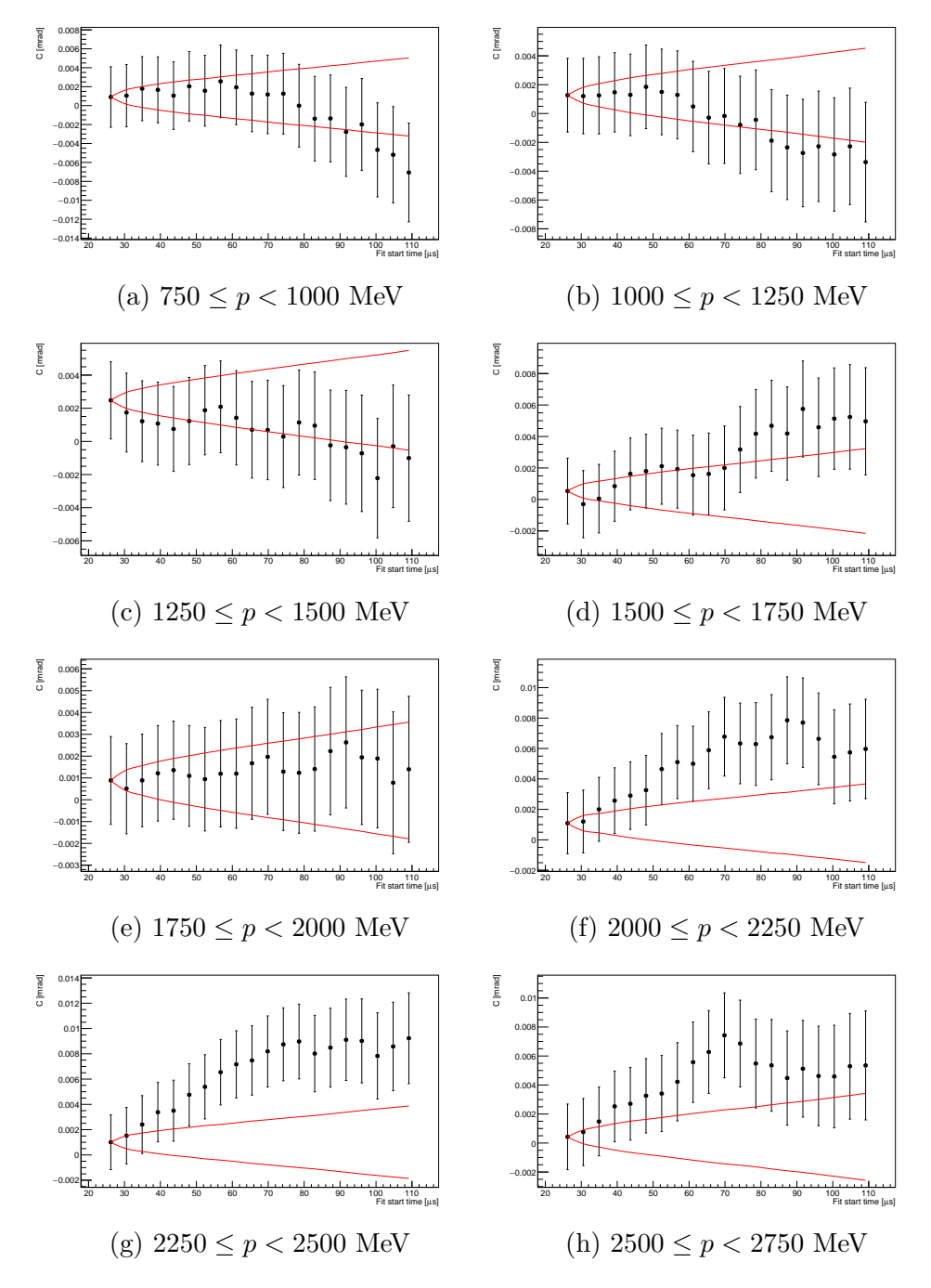


Figure B.15: Fit start time scans for Run-3a S12 fit parameter C, the red line indicates the 1σ allowed variation.

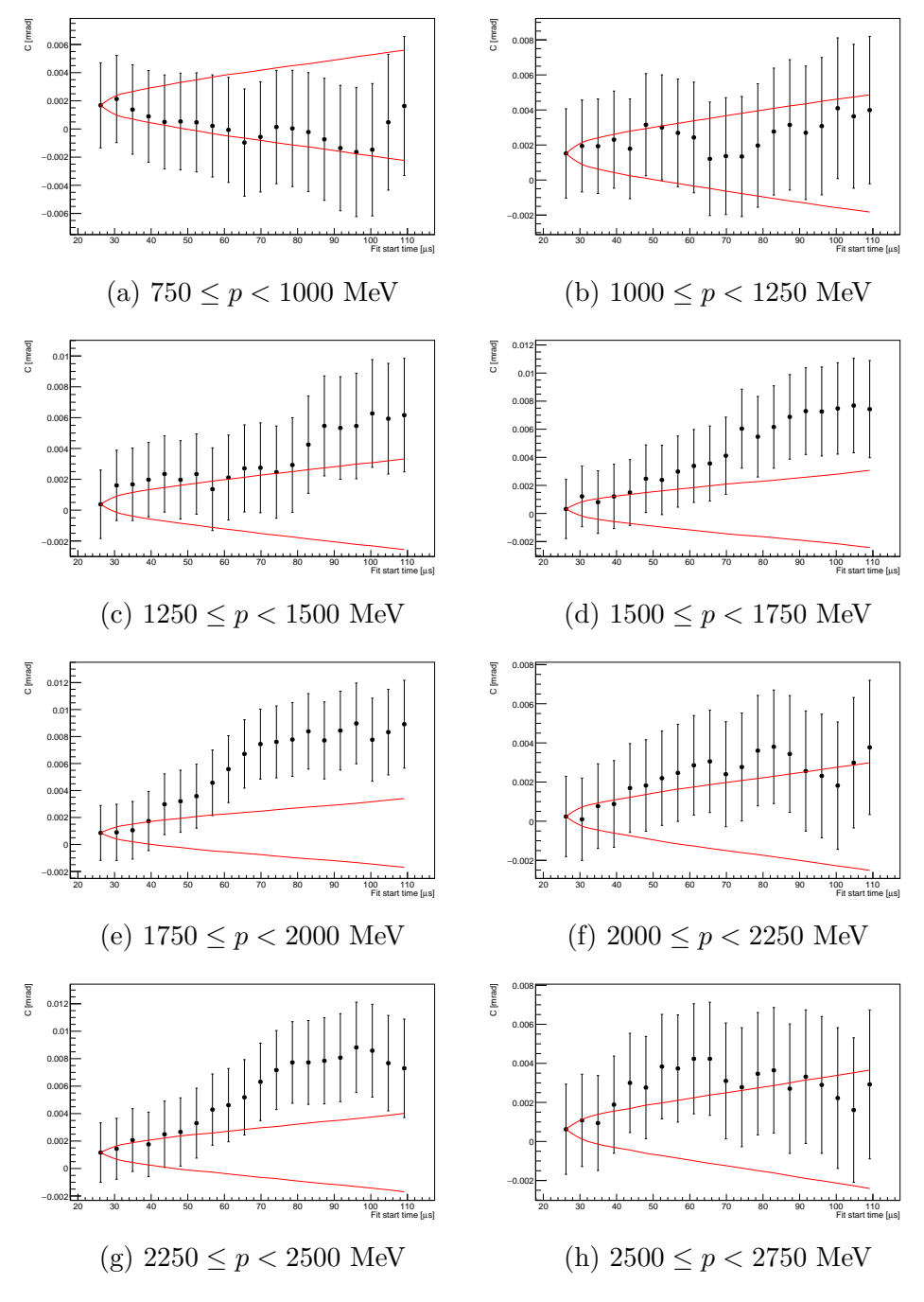


Figure B.16: Fit start time scans for Run-3a S18 fit parameter C, the red line indicates the 1σ allowed variation.

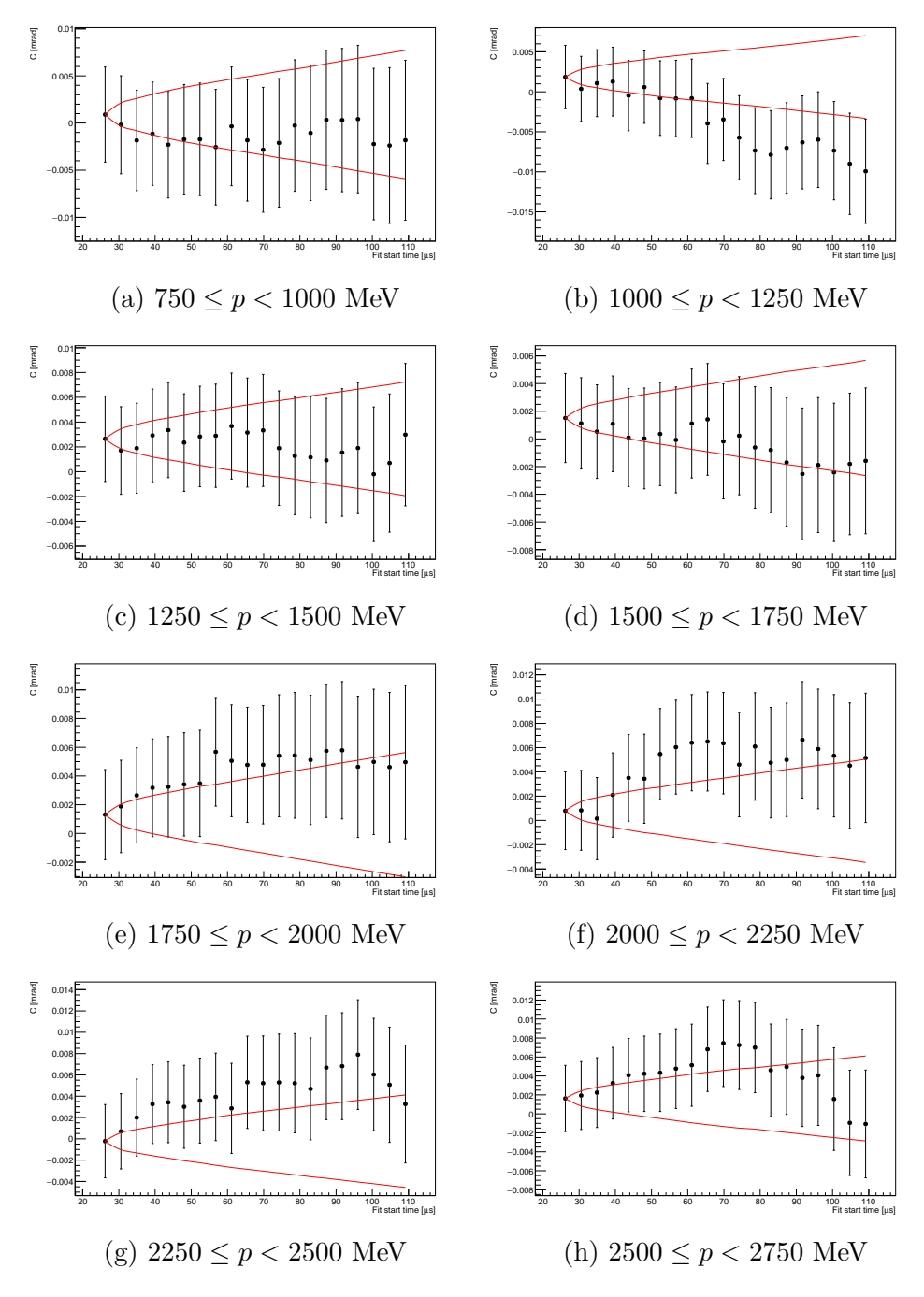


Figure B.17: Fit start time scans for Run-3b S12 fit parameter C, the red line indicates the 1σ allowed variation.

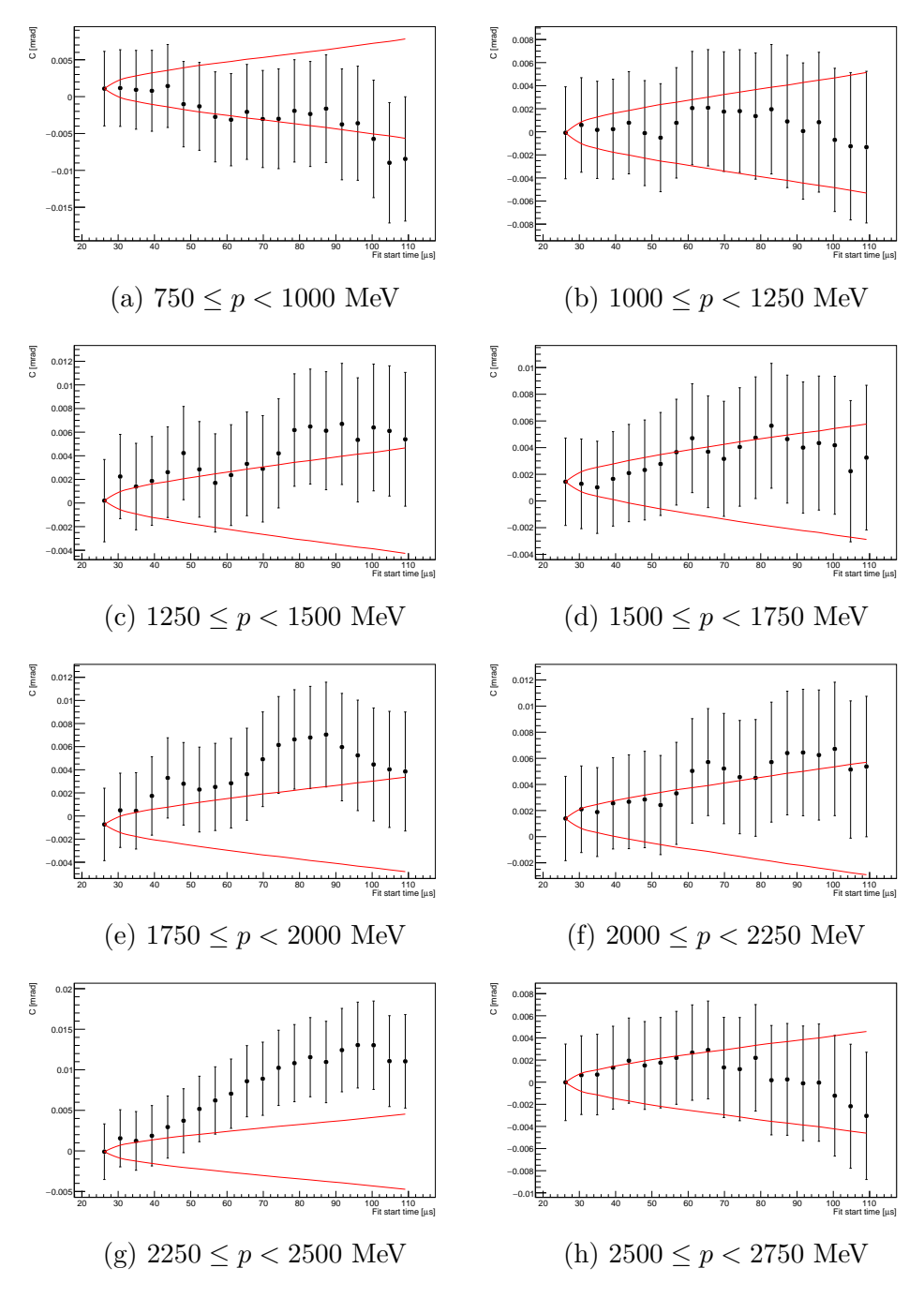


Figure B.18: Fit start time scans for Run-3b S18 fit parameter C, the red line indicates the 1σ allowed variation.

Appendix C

Uncertainties on the R-factors

From Equation 3.2.8, which determines the contribution on the tilt uncertainty from each reduction factor, it is evident that measuring $A_{\rm EDM}=0$ will result in this uncertainty also reducing to 0. As this is not an unexpected result, it is pertinent to consider if this treatment is an underestimation of the total uncertainty

Errors on the R-factors are combined by standard error propagation such that

$$\Delta \delta^* = \delta^* \sqrt{\left(\frac{\Delta A_{\text{EDM}}}{A_{\text{EDM}}}\right)^2 + \sum_i \left(\frac{\Delta R_i}{R_i}\right)^2}.$$
 (C.0.1)

However, this equation is not taking account of the cross-term that could enter if the result was actually $A_{\rm EDM} = A_{\rm EDM} + \Delta A_{\rm EDM}$. Using just $R_{\rm acc}$ as an example (such that and $\delta^* = A_{\rm EDM}/R_{\rm acc}$) the uncertainty would be

$$\Delta \delta^* = \delta^* \sqrt{\left(\frac{\Delta A_{\text{EDM}}}{A_{\text{EDM}}}\right)^2 + \left(\frac{\Delta R_{\text{acc}}}{R_{\text{acc}}}\right)^2 + \left(\frac{\Delta A_{\text{EDM}} \Delta R_{\text{acc}}}{R_{\text{acc}}}\right)^2}, \quad (C.0.2)$$

where the additional term is dependent on $\Delta A_{\rm EDM}$. Then, rewriting the Equation C.0.2 as

$$\Delta \delta^* = \sqrt{\left(\frac{\Delta A_{\rm EDM}}{R_{\rm acc}}\right)^2 + \left(\frac{A_{\rm EDM}}{R_{\rm acc}}\frac{\Delta R_{\rm acc}}{R_{\rm acc}}\right)^2 + \left(\frac{\Delta A_{\rm EDM}\Delta R_{\rm acc}}{R_{\rm acc}^2}\right)^2}, \quad (C.0.3)$$

and rearranging to

$$\Delta \delta^* = \sqrt{\left(\frac{\Delta A_{\rm EDM}}{R_{\rm acc}}\right)^2 \left(1 + \left(\frac{\Delta R_{\rm acc}}{R_{\rm acc}}\right)^2\right) + \left(\frac{A_{\rm EDM}}{R_{\rm acc}}\frac{\Delta R_{\rm acc}}{R_{\rm acc}^2}\right)^2}, \quad (C.0.4)$$

such that the addition from the cross term can be taken as $\Delta R_{\rm acc}/R_{\rm acc}$ combined in quadrature.

Now, the acceptance correction is typically $R_{\rm acc}=0.6$, with an uncertainty $\sim \Delta R_{\rm acc}=0.05$ giving $\Delta R_{\rm acc}/R_{\rm acc}=0.08$. This first term is then increased from $\Delta A_{\rm EDM}R_{\rm acc}$ to $1.003\times\Delta A_{\rm EDM}R_{\rm acc}$, which is deemed negligible. In the case of $A_{\rm EDM}=0$, there is no change to this argument and, as the acceptance has the largest uncertainty, this is extended to all the R-factors.

Consequently, assuming the unblinded result measures $A_{\rm EDM}=0$ such that R-factor uncertainties go to zero, the best estimate of the blinded result is

$$d_{\mu} = 8.10 \pm 0.18 \text{(stat.)} \pm 0.07 \text{(syst.)} \times 10^{-19} e \cdot \text{cm.}$$

Which can be compared to the result including R-factor uncertainties given the size of the blinded $A_{\rm EDM}$ that gives

$$d_{\mu} = 7.96 \pm 0.18(\text{stat}) \pm 0.16(\text{syst}) \times 10^{-19} e \cdot \text{cm},$$

where the systematic uncertainty contribution is larger and the central value is also shifted.